

**Multi-scale Characterization of the Petrophysical Properties of
Tight Sedimentary Rocks: Examples from an Ordovician
Limestone, Canada and Silurian and Ediacaran Shales, China**

Von der Fakultät für Georessourcen und Materialtechnik der
Rheinisch -Westfälischen Technischen Hochschule Aachen

zur Erlangung des akademischen Grades eines

Doktors der Naturwissenschaften

genehmigte Dissertation

vorgelegt von

M.Sc. Zhazha Hu

aus Hubei/China

Berichter: Univ. Prof. Dr. Ralf Littke

Univ. Prof. Dr. Rudy Swennen

Tag der mündlichen Prüfung: 30.11.2020

Diese Dissertation ist auf den Internetseiten der Universitätsbibliothek online verfügbar.

500000

Fakultät für Georessourcen und Materialtechnik

S. Frenzel-Gumlich

Intzestr. 1

52056 Aachen

Fax: 0241-80-92370

E-Mail: promotionen@fb5.rwth-aachen.de

Eidesstattliche Erklärung

1.)

Hiermit versichere ich eidesstattlich, dass ich die Dissertation selbstständig verfasst und alle in Anspruch genommenen Hilfen in der Dissertation angegeben habe.

Zhazha Hu

Unterschrift

Aachen, 15.08.2021

Ort, Datum

2.) Sofern die Dissertation in einer Einrichtung außerhalb der RWTH entstanden ist:

Hiermit erkläre ich, dass mit Veröffentlichung der Dissertation keine bestehenden Betriebsgeheimnisse verletzt werden.

Zhazha Hu

Unterschrift

Aachen, 15.08.2021

Ort, Datum

ABSTRACT

Understanding fluid transport processes in low-permeable sedimentary rocks is required for a wide range of geotechnical applications, especially for assessing their sealing behavior during nuclear waste storage and their transport properties as an unconventional reservoir. Fluid transport is largely controlled by the pore structure. Apart from pore structure characterization, sorption measurements are of equal importance in assessment of shale gas reservoirs.

The first part of this study (chapter 2 and 3) employed a series of petrophysical and imaging techniques to characterize the fluid transport properties and pore structure of Middle Ordovician Cobourg limestone, a potential host rock for nuclear waste repositories in Canada. For this purpose, porosity and permeability were measured with helium on four dry cylindrical plugs in pseudo-triaxial cells under defined isostatic stress conditions (5-20 MPa). The experimental results indicate that stress sensitivity coefficients of permeability are about one order of magnitude higher than those of porosity, which is the result of preferential closure or volume reduction of interconnecting restrictions (pore throats) of the pore network with increasing stress. The major discontinuities observed in the most permeable sample are identified by scanning electron microscope (SEM) as open stylolites enhancing the permeability between two to three orders of magnitude as compared to samples where stylolites were absent.

Pore morphologies and pore structures of the intact Cobourg limestone were analyzed by focused ion beam - and broad ion beam - scanning electron microscope (FIB- and BIB - SEM). Mineralogy analysis indicates that it is characterized as a tight rock dominated by calcite grains of variable sizes (μm - cm) surrounded by idiomorphic or subhedral minerals (quartz, dolomite and pyrite) and meshy clay minerals. The clay mineral and calcite phases contribute over 90% of the total pore area. The clay pores are relatively small and occur close to each other, elongated in shape and are interpreted as interparticle pores. On the contrary, the pores associated with calcite have a large pore size range and are distant from each other, equidimensional or elongated in shape and can mostly be considered as intraparticle pores. Different pore size distributions were identified for the two phases in BIB-SEM maps, which can be characterized by power law relationships between pore area and normalized pore frequency with

different exponents (1.93-2.18 for calcite and 2.50-2.59 for clay). Based on the relationship, extrapolated porosities are compared to porosities obtained by helium pycnometry (HP).

In Chapter 4 the pore structure and sorption capacity of Ediacaran Doushantuo and Liuchapo shales were characterized and compared with those of commercially producing Silurian Longmaxi shales in Upper Yangtze platform. The results show that computed maximum gas storage capacities at present day reservoir conditions are lower for the Ediacaran shales (0.054 - 0.251 mmol/g) when compared to the Silurian shales (0.237 - 0.330 mmol/g), while the maximum amounts of sorbed methane of Ediacaran and Silurian shales were in the same range, between 0.02 - 0.19 mmol/g and 0.08 - 0.21 mmol/g, respectively. Porosities were smaller for Ediacaran shales (1.4 - 4.6%) than for Silurian shales (6.2 - 7.4%). Low-pressure N₂- and CO₂ adsorption measurements also indicated larger micropore volume fractions and smaller mesopore volumes for the Ediacaran shales. This is likely related to burial and to a silica-associated preservation of pores. TOC content exhibits significant control on sorption capacity and CO₂ micropore volume for both shales. The difference in sorption contribution of clay minerals can be attributed to different clay types and evolutionary differences of illite.

The findings presented in the thesis have important implications for pore structure characterization, Gas-In-Place estimations, fluid flow modelling and sealing efficiency assessments.

ZUSAMMENFASSUNG

Für eine Vielzahl von geotechnischen Anwendungen ist ein sehr gutes Verständnis von Transportprozessen für Flüssigkeiten und Gase in niedrig-permeablen Sedimentgesteinen erforderlich. Dies gilt insbesondere für die Beurteilung ihres Abdichtungsverhaltens bei der Lagerung von Atommüll und für ihre Eigenschaften als unkonventionelles Reservoir für Erdgas und Erdöl. Der Flüssigkeitstransport wird weitgehend durch die Porenstruktur gesteuert. Neben der Charakterisierung der Porenstruktur sind aber auch Sorptionsmessungen für die Beurteilung der Transporteigenschaften niedrig-permeabler Sedimentgesteine von großer Bedeutung.

Im ersten Teil dieser Studie (Kapitel 2 und 3) wurden eine Reihe von petrophysikalischen und bildgebenden Verfahren eingesetzt, um die Transporteigenschaften und die Porenstruktur von Kalkstein aus dem mittleren Ordovizium von Cobourg, einem potenziellen Wirtsgestein für Endlagerstätten für nukleare Abfälle in Kanada, zu charakterisieren. Zu diesem Zweck wurden die Porosität und Permeabilität mit Helium an vier trockenen zylindrischen Gesteinskörpern in pseudo-triaxialen Zellen unter definierten isostatischen Spannungsbedingungen (5 - 20 MPa) gemessen. Die experimentellen Ergebnisse deuten darauf hin, dass die Spannungsempfindlichkeitskoeffizienten der Permeabilität um etwa eine Größenordnung höher sind als die der Porosität, was das Ergebnis einer bevorzugten Schließung oder Volumenreduzierung von Porenhälsen des Porennetzwerks mit zunehmender Spannung ist. Die wichtigsten Diskontinuitäten, die in der durchlässigsten Probe auftreten, wurden im Rasterelektronenmikroskop (SEM) als offene Stylolithe identifiziert, die Durchlässigkeit um zwei bis drei Größenordnungen im Vergleich zu Proben ohne Stylolithe erhöhen.

Die Porenmorphologien und Porenstrukturen des intakten Cobourg-Kalksteins wurden außerdem nach Politur mit einem fokussierten Ionenstrahl beziehungsweise einem breiten Ionenstrahl am Rasterelektronenmikroskop (FIB- und BIB-SEM) analysiert. Mineralogische Analysen weisen darauf hin, dass es sich um ein dichtes Gestein handelt, das von Calcitkörnern unterschiedlicher Größe (μm - cm) dominiert wird, die von verschiedenen spröden Mineralen (Quarz, Dolomit und Pyrit) und miteinander verzahnten Tonmineralen umgeben sind. Die Tonmineral- und Kalzitphasen machen über 90% der Fläche aus, in der Poren vorhanden sind. Die Tonporen sind relativ klein

und nahe beieinander, länglich in der Form und werden als interpartikuläre Poren interpretiert. Die Poren, die mit Kalzit assoziiert sind, decken im Gegensatz dazu einen großen Porengrößenbereich ab und sind weiter voneinander entfernt, von äquidimensionaler oder länglicher Form und können meist als intrapartikuläre Poren betrachtet werden. In BIB-SEM-Karten wurden für die beiden Phasen unterschiedliche Porengrößenverteilungen identifiziert, die durch Potenzgesetzbeziehungen zwischen Porenfläche und normierter Porenhäufigkeit mit unterschiedlichen Exponenten (1.93-2.18 für Calcit und 2.50-2.59 für Ton) charakterisiert werden können. Die aus der Rasterelektronenmikroskopie abgeleiteten und zu niedrigen Porengrößen extrapolierten Porositäten wurden mit den durch Heliumpyknometrie (HP) erhaltenen Porositäten verglichen.

In Kapitel 4 wurden die Porenstruktur und die Sorptionskapazität der ediacarischen Doushantuo- und Liuchapo-Schiefer, China, charakterisiert und mit denen der kommerziell produzierten silurischen Longmaxi-Schiefer der oberen Jangtse Plattform verglichen. Die Ergebnisse zeigen, dass die berechneten maximalen Gasspeicherkapazitäten unter den heutigen Reservoirbedingungen für die ediacarischen -Schiefer (0.054 – 0.251 mmol/g) im Vergleich zu den silurischen Schieferen (0.237 – 0.330 mmol/g) niedriger sind. Die maximalen Mengen an sorbiertem Methan der Ediacara- und Silur-Schiefer lagen im ähnlichen Bereich zwischen 0.02 – 0.19 mmol/g bzw. 0.08 - 0.21 mmol/g. Die Porositäten der Ediacara-Schiefer (1.4 – 4.6%) sind geringer als die der Silur-Schiefer (6.2 – 7.4%). Niederdruck-N₂- und CO₂-Adsorptionsmessungen zeigten auch größere Mikroporenvolumenanteile und kleinere Mesoporenvolumina für die Ediacara-Schiefer. Dies hängt wahrscheinlich mit der Versenkung und mit einer über Kieselsäurediagenese ausgelösten Porenerhaltung zusammen. Der TOC-Gehalt ist entscheidend für die Sorptionskapazität und das CO₂-Mikroporenvolumen beider Schiefer. Der Unterschied im Sorptionsbeitrag von Tonmineralen kann auf verschiedene Tonminerale und diagenetische Unterschiede von Illit zurückgeführt werden.

Die in der Dissertation vorgestellten Ergebnisse haben wichtige Implikationen für die Charakterisierung der Porenstruktur niedrig-permeabler Gesteine, die Modellierung der Flüssigkeitsströmung in solchen Gesteinen, die Bewertung der Abdichtungseffizienz und möglicherweise Abschätzungen von gespeicherten Gasmengen.

ACKNOWLEDGEMENTS

The four years' journey of my Ph.D. study at RWTH Aachen University is about to end while I still feel the luckiness and happiness when I received the confirmation letter from Prof. Ralf Littke. In this big family of LEK, I would like to express my sincere gratitude to Prof. Littke in the first place. His patient instruction and mental encouragement always lead me to the right directions in the scientific paths towards success.

I would like to appreciate my direct advisor Dr. Alexandra Amann for her full support in my experimental work and her inspiration in our discussion of scientific ideas. Her rigorous attitude towards science impresses me and will influence my whole professional life. Apart from academic study, I was invited to her house for several times and got a deep understanding of the German life, which will be a happy memory for me. I am also thankful to another advisor Dr. Jop Klaver, who is an easy-going man and so professional in imaging analysis. The high-quality BIB-SEM images provided by him contributed significantly to pore morphology characterization of the Cobourg limestone. He led me through basic image processing and opened a new world to me. His suggestions and encouragement were really helpful when I came across difficult issues.

Furthermore, I want to express my thanks to Dr. Bernhard Krooss, Dr. Reinhard Fink, Dr. Garri Gaus and Prof. Rudy Swennen for their constructive and valuable comments on this work. I am also grateful to Timo Seemann from the Institute of Clay and Interface Mineralogy for interpreting XRD and low-pressure N₂ and CO₂ adsorption measurements. Dr. Jan Dewanckele from TESCAN company is specially appreciated for our cooperation in FIB-SEM and micro-CT experiments. I would like to thank Patrick Thelen for his support in our petrophysics lab and I am really impressed by his technical skills. Donka Macherey was always available and patient for providing reliable and superior polished sections and I am grateful for her work. Michelle Evertz is thanked for her help in administrative work, which saved me a lot of time. Special thanks go to the China Scholarship Council for its financial support for my study in Germany.

I feel really lucky to be surrounded by so many good fellow Ph.D. students and together

they created a cozy environment for me. My classmate and colleague for 7 years, Qian Zhang, is thanked for daily communication in academic research. I would like to appreciate Steffen Nolte, who helped me a lot in German-related issues. Felix Froidl is always keen to gossip and jokes. Thanks for your “effort” in bringing a lot of joy to our institute. I would like to give my sincere appreciation to Dr. Laura Zieger, Jinqi Qiao, Tianyu Zheng, Sebastian Amberg, Linda Burnaz, Anna Kutovaya, Alireza Baniasad, Joschka Röth, Dr. Sebastian Grohmann.

Finally, I would like to thank my family for their constant support throughout my Ph.D. study. Four years’ studying abroad hindered me from accompanying my parents, which frequently made me feel uneasy. My sole sister always supported me financially and psychologically. You contributed a lot to this thesis in an invisible way and I would like to dedicate it to you all!

Contents

1 INTRODUCTION.....	1
<i>1.1 Energy policy in China.....</i>	<i>1</i>
1.1.1 Nuclear power.....	2
1.1.2 Shale gas.....	3
<i>1.2 Radioactive waste disposal.....</i>	<i>3</i>
1.2.1 Sources of radioactive waste.....	4
1.2.2 Classification of radioactive waste.....	4
1.2.3 Radioactive waste disposal.....	5
<i>1.3 Gas storage in shale gas reservoirs.....</i>	<i>6</i>
1.3.1 Pore classification.....	7
1.3.2 Gas storage mechanisms.....	8
<i>1.4 Comparison of core analysis techniques.....</i>	<i>10</i>
1.4.1 Porosity measurements.....	10
1.4.2 Permeability measurements.....	11
<i>1.5 Main objectives and thesis overview.....</i>	<i>12</i>
2 STRESS SENSITIVITY OF POROSITY AND PERMEABILITY OF COBOURG LIMESTONE.....	15
<i>2.1 Introduction.....</i>	<i>16</i>
<i>2.2 Theory.....</i>	<i>18</i>
2.2.1 Stress dependence of permeability and porosity.....	18
2.2.2 Gas permeability.....	18
<i>2.3 Samples and methods.....</i>	<i>20</i>
2.3.1 Geological setting.....	20
2.3.2 Sample material.....	21
2.3.3 X-ray diffraction analysis (XRD).....	22
2.3.4 Micro-CT.....	22
2.3.5 BIB-SEM.....	23
2.3.6 Porosity measurements.....	23
2.3.7 Gas permeability measurements at controlled stress.....	25
<i>2.4 Results.....</i>	<i>27</i>
2.4.1 XRD analysis.....	27
2.4.2 Microstructure characteristics.....	27
2.4.3 Porosity measurements.....	31
2.4.4 Permeability measurements with helium.....	32
<i>2.5 Discussion.....</i>	<i>34</i>
2.5.1 Comparison of two porosity measurement methods.....	34
2.5.2 Stress sensitivity of porosity and permeability.....	35
2.5.3 Pore structure evolution with effective stress.....	41
<i>2.6 Conclusions.....</i>	<i>43</i>

3. MULTI-SCALE CHARACTERIZATION OF PETROPHYSICAL PROPERTIES OF THE COBOURG LIMESTONE- A POTENTIAL NUCLEAR WASTE HOST ROCK IN CANADA	45
3.1 <i>Introduction</i>	46
3.2 <i>Samples</i>	49
3.3 <i>Imaging experiments and simulation</i>	50
3.3.1 X-ray micro-CT	50
3.3.2 BIB-SEM	50
3.3.3 FIB-SEM	52
3.3.4 Image analysis	52
3.3.5 Permeability simulation.....	55
3.4 <i>Results</i>	56
3.4.1 BIB-SEM image analysis	56
3.4.2 FIB-SEM image analysis.....	64
3.4.3 X-ray micro-CT image analysis	66
3.4.4 Permeability simulation.....	67
3.5 <i>Discussion</i>	68
3.5.1 Methodological comparison of porosity.....	68
3.5.2 Pore morphology and pore size distribution.....	70
3.5.3 Dominant flow pathways.....	72
3.6 <i>Conclusions</i>	75
4. PORE STRUCTURE AND SORPTION CAPACITY INVESTIGATIONS OF EDIACARAN AND LOWER SILURIAN GAS SHALES FROM THE UPPER YANGTZE PLATFORM, CHINA.....	77
4.1 <i>Introduction</i>	78
4.2 <i>Geological setting</i>	80
4.3 <i>Samples and experiments</i>	82
4.3.1 Samples.....	82
4.3.2 Microscopy	83
4.3.3 Elemental analysis	84
4.3.4 X-ray diffraction analysis (XRD).....	84
4.3.5 Water immersion porosimetry (WIP).....	85
4.3.6 High-pressure methane sorption measurements	85
4.3.7 Low-pressure nitrogen and carbon dioxide adsorption measurements	87
4.4 <i>Results</i>	88
4.4.1 Mineral composition.....	88
4.4.2 TOC, TS and thermal maturity	89
4.4.3 Pressure equilibration and uptake kinetics	89
4.4.4 High-pressure methane sorption.....	90
4.4.5 Low-pressure nitrogen adsorption	92
4.4.6 Porosity and pore size distribution	94

4.5 Discussion	95
4.5.1 Effect of organic matter and clay minerals on methane sorption capacity..	95
4.5.2 Effect of thermal maturity on methane sorption capacity	98
4.5.3 Pore structure	100
4.5.4 Gas-in-place.....	101
4.6 Conclusions	104
5. General discussion and outlook	107
5.1 General discussion	107
5.1.1 Pore accessibility	107
5.1.2 Gas-In-Place estimation.....	108
5.2 Outlook.....	110
5.2.1 Competitive sorption on core shales under effective stress.....	110
5.2.2 Fracture sealing and reopening.....	110
5.2.3 Fluid flow testing incorporated with CT scanning	111
6. References.....	113
7. Appendix.....	127

LIST OF TABLES

Table 2.1 XRD result of the Cobourg limestone.....	27
Table 2.2 Porosity values of samples under the unconfined condition.....	31
Table 2.3 Klinkenberg-corrected permeability coefficients (m^2) of Cobourg limestone samples as a function of confining pressure in the second loading-unloading cycle.....	32
Table 2.4 Summary of stress sensitivity coefficients of permeability of sedimentary rocks.....	37
Table 2.5 Summary of stress sensitivity coefficients of porosity of sedimentary rocks.....	38
Table 2.6 Porosity sensitivity exponents of different pore models (modified after Zhang et al. 2016).....	38
Table 2.7 The mean effective pore sizes of four samples at different confining pressures.	43
Table 3.1 Mineralogical composition obtained from BIB- and FIB-SEM, micro-CT and XRD analyses of Cobourg limestone.....	58
Table 3.2 Porosities of different mineral phases in BIB-SEM maps and FIB-SEM volume and bulk porosities measured by HP.....	61
Table 3.3 Power law exponents (D) and constants (log C) for pores in calcite phase, clay mineral phase and total phases.....	64
Table 3.4 The simulated permeability coefficients of sample D at corresponding isotropic permeability, pressure difference and temperature by using the FlowDict module of GeoDict. Isotropic permeability is assigned to silicate or carbonate phase when silicate or carbonate phase is taken as the only permeable phase.....	68
Table 4.1 Characterization of Ediacaran and Silurian shale samples based on elemental composition (TOC, TS), solid bitumen reflectance (BR_r), equivalent vitrinite reflectance (VR_r) and mineral composition.....	83
Table 4.2 Excess sorption capacities at 10 MPa (n_{ex}^{10MPa}), Langmuir volumes (n_{∞})	

normalized to sample weight or sample weight and TOC content as well as Langmuir pressure (P_L) for Ediacaran (E1-E6) and Silurian (S1-S6) shales at dry and moist (97% relative humidity) conditions.....92

Table 4.3 Porosity and pore structure analysis results from N_2 and CO_2 adsorption measurements on Ediacaran (E1-E6) and Silurian (S1-S6) shale samples.....94

LIST OF FIGURES

Fig 1.1 (a) The energy consumption mix of China from 2009 to 2018 (data from NBS, 2019); (b) A detailed energy consumption mix of China in 2018 (data from CEPI, 2019)	1
Fig 1.2 The mix of electricity generation capacity in China from 2011 to 2018 (data from CEPI, 2019)	2
Fig 1.3 Comparison of the shale gas production between China and the US (data from EIA, 2019 and Dai et al. 2020)	3
Fig 1.4 Simplified sketch of multi-barrier system in radioactive waste repositories.....	6
Fig 1.5 The classification of pore types in shales based on FE-SEM analysis (Loucks et al., 2012)	8
Fig 1.6 Cylindrical and slit pore models illustrating gas storage mechanisms in shales (Feng, et al., 2020)	9
Fig 2.1 Stratigraphic column at Bruce nuclear site (modified after Beauheim et al.2014)	20
Fig 2.2 Sample location and generalized bedrock geology (modified after Xiang et al. 2013)	21
Fig 2.3 (a) The sample cube displaying macroscopically observable heterogeneity; (b) Cylindrical samples of C, D and E drilled in three mutually perpendicular directions as indicated by red arrows; (c) Cylindrical sample B with white strip on the top surface.....	22
Fig 2.4 Sketch of the helium pycnometer for porosity measurements under unconfined conditions.....	24
Fig 2.5 Sketch of the system used for pore volume and permeability measurements under defined confining pressures.....	25
Fig 2.6 Sketch of the pressure decay curves of the conventional pulse decay (PD)	

method, the constant downstream pressure (CDP) method and the constant upstream pressure (CUP) method.....26

Fig 2.7 Micro-CT cross-section images of all samples. Top: sample B before (a) and after petrophysical experiments (b); bottom: (c) sample C after petrophysical measurement; (d) sample D before petrophysical experiments; (e) sample E after petrophysical measurement.....28

Fig 2.8 BIB-SEM images of the Cobourg limestone: (a) Angular pores with sizes up to half a micrometer form the intraparticle pores of carbonate grains and the clay matrix is distributed among carbonate grains; (b) Slit-shaped pores in the clay matrix among carbonate grains. Larger interparticle triangular pores shown in the middle of the image are uncommon; (c) Micro-fractures cut through the clay matrix near the discontinuities of sample B.....29

Fig 2.9 Fracture distribution on the cross-section area of sample B. (a) BSE map shows that two discontinuity zones are located on the upper and middle-right part of the cross-section area. The upper discontinuity is rich in bright minerals; (b-d) EDX maps exhibit the distribution of Al, Si and S on the upper part of the cross-section area (the upper red mark zone in Fig 2.9a); (e) SE2 image shows the fracture width distribution along the lower discontinuity zone (the lower red mark zone in Fig 2.9a). The average aperture of the fracture is 4.53 μm30

Fig 2.10 Relationship between effective stress and porosity in loading-unloading cycle. The circle symbols represent the porosity values in the loading path, while the square symbols denote the porosity values in the unloading path. Triangle symbols represent the porosity values determined by He pycnometry under ambient conditions. The error bars are not visible at this scale.....31

Fig 2.11 Klinkenberg plots of permeability tests using the CDP method on Cobourg limestone samples at different confining pressures (t denotes the duration of the measurement).....33

Fig 2.12 Relationship between Klinkenberg-corrected permeability coefficients and effective stress.....33

Fig 2.13 (a) Comparison of bulk densities of Cobourg limestone samples determined by caliper and water immersion porosimetry (WIP); (b) Comparison of grain densities measured by HP and WIP; (c) Comparison of porosities ($V_{\text{pore}}/V_{\text{bulk}}$) measured by HP and WIP. HP porosities were calculated twice, using V_{bulk} from caliper measurements (black dots) and from water immersion experiments (red dots).....35

Fig 2.14 (a) Relationship between exponential stress sensitivity coefficients of porosity and exponential stress sensitivity coefficients of permeability for different lithologies; (b) Relationship between Klinkenberg-corrected permeability and porosity for Cobourg limestones (the slope of γ represents the porosity sensitivity exponent).....36

Fig 2.15 Intrinsic permeability coefficients normalized to intrinsic permeability at initial effective stress ($k_{\infty}/k_{\infty,0}$) versus effective stress for both loading (solid lines) and unloading paths (dashed lines).....41

Fig 2.16 Slippage factors at different effective stresses for samples B, C, D and E in the loading and unloading paths. Black symbols represent the slippage factors in the loading path and red symbols denote the slippage factors in the unloading path.....41

Fig 2.17 The mean effective slit width at different confining pressures (the black symbols represent the slit widths derived from slippage factors at different confining pressures and different symbol shapes denote different samples, the red symbols represent the slit width of sample B calculated by equation 8 with the measured intrinsic permeability, the green dot denotes the slit width of sample B by BIB-SEM statistics at unconfined conditions).....42

Fig 3.1 (a) Rendered X-ray micro-CT image of cylindrical sample A and the location of the BIB polished region (magnified in Fig 3.2a); (b) Cylindrical sample B with white strip on the top surface; (c) Cylindrical samples of C, D and E drilled in three mutually perpendicular directions as indicated by red arrows.....49

Fig 3.2 Overview of the studied section of sample A and the corresponding ROI of BIB- and FIB-SEM. (a) The cross-section of sample A; (b) The BIB-polished region: maps 1 and 2 are the ROI where both mineral composition and pore size distributions were analyzed quantitatively and the ROI of FIB-SEM is located on the upper left corner; (c) The ROI of FIB-SEM traversed by a strip rich in clay minerals; (d) The BSE

image of map 1.....	51
Fig 3.3 Workflow of BIB-SEM image processing.....	53
Fig 3.4 Silicate mineral segmentation from the X-ray micro-CT images of sample D by grey level. (a) The original X-ray micro-CT image; (b) The segmented image (yellow standing for the silicate mineral phase and the magenta representing the carbonate mineral phase); (c) The 3D distribution of connected components of silicate mineral phase. The biggest component (yellow) connects the top with the bottom of the plug.....	54
Fig 3.5 Mineral distribution overview of BIB-polished Cobourg limestone surface (0.72 mm ²). The red squares show the areas of BIB-SEM maps 1 and 2 and the location for FIB-SEM.....	58
Fig 3.6 BSE images of Cobourg limestone. (a) Angular intraparticle pores with sizes up to a few micrometer in calcite grains and clay minerals randomly distributing among calcite grains; (b) The high resolution image showing the submicron triangular and elongated pores in the clay fraction; (c) Intraparticle pores in rhombus dolomite and microfractures at the interface between carbonate and clay fractions; (d) Intercrystalline pores in framboidal pyrites. (e) Submicron slit-shaped pores in the clay fraction; (f) Microfractures accumulating in the fine-grained silicate-rich fraction.....	59
Fig 3.7 Area fractions of slit-shaped and high circularity pores in calcite and clay mineral phases of maps 1 and 2.....	60
Fig 3.8 Frequency distributions (pore frequency vs equivalent circular pore diameter) of total visible pores in BIB-SEM map 1 (a) and map 2 (b); Frequency distributions of visible pores in calcite (c) and clay mineral (e) phases of map 1; Frequency distributions of visible pores in calcite (d) and clay mineral (f) phases of map 2.....	62
Fig 3.9 Normalized pore size distributions of total visible pores in maps 1 and 2 (a). The linear best fit is shown as a dashed line with a corresponding equation. The slope and intercept of the best fit are the minus D and log C values of Eq. 2, respectively. Cumulative porosity distributions of total visible pores in maps 1 and 2 and corresponding cumulative porosity distribution of clay and calcite phases (pore area	

normalized to respective mineral phase area) (b). Normalized pore size distributions in calcite and clay mineral phases of map 1 (c) and map 2 (d). Pore area fraction distributions of calcite and clay mineral phases in map 1 (e) and map 2 (f).....63

Fig 3.10 Dragonfly’s deep learning segmentation results for the FIB-SEM image stack: (a) Original greyscale 3D rendered structure of FIB-SEM image stack (10 nm voxel size); (b) Clay mineral phase (green) is separated from calcite phase (white) and pores in calcite (gold) and pores in clay (blue) are segmented; (c) The 3D distribution of pores in clay and calcite. The pores in calcite phase are apparently isolated to each other and no connected pores are identified in clay mineral phase when zooming in (different colors used to differentiate adjacent pores in clay).....65

Fig 3.11 Pore volume fraction distributions (a) and cumulative porosity distributions (pore volume normalized to respective mineral phase volume) (b) of calcite and clay mineral phases of FIB-SEM volume. Normalized pore size distributions in calcite and clay mineral phases based on 2D FIB-SEM image analyses (c). The linear best fit is shown as a dashed line with a corresponding equation. The slope and intercept of the best fit are the minus D and log C values of Eq. 2, respectively. The hollow blue and red squares represent the normalized frequencies of pores in calcite and clay when the equivalent circular pore diameter is equal or smaller than 51 nm, respectively. These data points are excluded to obtain linear best fits. The frequency fraction distribution of the shortest distance (edge to edge) between each pore and its nearest neighbor in calcite and clay mineral phases of the FIB-SEM volume (d).....66

Fig 3.12 Simulated permeability coefficients based on a range of tortuosity values and 2D pore cross-sections in calcite, clay and both mineral phases of map 1. The dashed bounds are the lab-measured permeability range (5.21×10^{-20} - 2.74×10^{-19} m²) of intact Cobourg limestone samples (C, D and E).....67

Fig 3.13 Extrapolation of cumulative porosity distributions obtained from BIB-SEM map 1 (a), map 2 (b) and FIB-SEM images (c). Cumulative porosity distribution obtained from FIB-SEM volume (purple data point) and HP bulk porosities of samples B, C, D and E (blue zone) are compared. D and log C values are utilized for the extrapolations of cumulative calcite and clay porosities, which are represented by the blue and red dashed lines, respectively. The extrapolation of cumulative total porosity

in map 1 and 2 is the sum of extrapolated cumulative calcite and clay porosities and represented by the yellow dashed line. As no linear relationship exists in the normalized pore size distribution of calcite phase in FIB-SEM images, D and $\log C$ are utilized for the extrapolation of cumulative total porosity in FIB-SEM images. All the porosities are pore areas or pore volumes normalized to total image areas or total structure volumes.....69

Fig 4.1 Paleogeographic map of the Yangtze Platform during Ediacaran and Cambrian times (modified after Guo et al. 2007). Well ST-101 penetrated the Ediacaran Doushantuo and Liuchapo Formations at depth between 1000 and 1200 m and well XY-1 penetrated the Silurian Longmaxi Formation at depth between 430 and 620 m.....81

Fig 4.2 Litho- and chrono-stratigraphy of the Upper Yangtze Platform (modified after Zhai, 1987 and Zhang et al. 2019).....82

Fig 4.3 High-pressure sorption setup (V1-V5 are either two-port or three-port valves and the syringe pump (Teledyne ISCO 260D) was programmed to stepwise increase the gas pressure in the reference cell).....86

Fig 4.4 Relationship between TS and TOC content (multiplied by 2) for Ediacaran and Silurian shale samples (“normal marine” line after Berner and Raiswell 1984).....89

Fig 4.5 Fractional uptake versus square root of time for (a) Ediacaran and (b) Silurian shales at about 0.5 MPa methane pressure, (c) helium and methane uptake rates of sample E1 at about 0.5 MPa gas pressure and (d) uptake rates at varying methane pressures from 0.7 to 20.5 MPa for sample E2.....90

Fig 4.6 Methane sorption isotherms at 318.15 K for (a) the Ediacaran shales at dry and moist conditions (97% relative humidity) and (b) the Silurian shales at dry conditions.....91

Fig 4.7 Comparison of Langmuir volumes and TOC contents for samples from the Ediacaran (Doushantuo and Liuchapo shales), Silurian (Longmaxi shale), Carboniferous (Barnett shale) and Cambrian/Ordovician (Alum shale).....91

Fig 4.8 Nitrogen adsorption and desorption isotherms of the Ediacaran (a) and Silurian

(b) shales at 77 K.....93

Fig 4.9 Relationships between TOC content and BET surface area (a), TOC content and CO₂ micropore volume (b) and CO₂ micropore volume and N₂ micropore volume (c).....93

Fig 4.10 Differential pore volume distribution (dV/dw) of Ediacaran (a) and Silurian (b) shales.....95

Fig 4.11 Mineral composition and respective contribution to Langmuir volume for the Ediacaran (a, b) and Silurian (c, d) shales (blue, grey and black colors represent rigid minerals, clay minerals and organic matter, respectively).....96

Fig 4.12 Relationship of estimated Langmuir volume of organic matter and equivalent vitrinite reflectance (symbols represent estimated Langmuir volumes of organic matter under the assumption of 0.1 mmol/g contribution of clay minerals to total sorption capacity and the error bars reflect assumptions of 0 and 0.2 mmol/g clay mineral contribution).....100

Fig 4.13 Estimates of excess sorption capacity (G_{ex}), free gas capacity (G_f) and total gas storage capacity (GIP) at a depth of 1200 m and corresponding temperature of 318.15 K for dry Ediacaran (a) and Silurian (b) shales (average porosity and bulk density of S1, S3 and S5 are used in the calculation of G_f for samples S2, S4 and S6 as porosities of these samples were likely enhanced by weathering).....103

LIST OF ABBREVIATIONS AND SYMBOLS

Abbreviation	Definition	Unit
A	Cross-sectional area	m ²
b	Gas slippage factor	Pa
BR _r	Solid bitumen reflectance	%
c	Adzumi constant	-
d	Mean effective pore diameter	m
D	Diameter	m
G _{ex}	Sorption storage capacity	mol kg ⁻¹
G _f	Free gas storage capacity	mol kg ⁻¹
GIP	Total amount of gas storage	mol kg ⁻¹
k	Permeability	m ²
k ₀	Permeability at zero effective stress	m ²
k _∞	Klinkenberg-corrected or intrinsic permeability	m ²
L	Length of a sample	m
l	Length of flow path	m
M	Molar mass	kg mol ⁻¹
N _i	Pore frequency	-
n _∞	Langmuir volume	mol g ⁻¹
n _{excess}	Excess sorption capacity	mol g ⁻¹
n _{abs}	Absolute sorption capacity	mol g ⁻¹
n _{trans}	Amount of transferred gas	mol g ⁻¹
n _{TOC}	Estimated Langmuir volume of organic matter	mol g ⁻¹
n _{clay}	Estimated Langmuir volume of clay minerals	mol g ⁻¹
n _{rigid}	Estimated Langmuir volume of rigid minerals	mol g ⁻¹
P	Pressure	Pa
ΔP	Pressure difference	Pa
P _L	Langmuir pressure	Pa
P _{eq}	Equilibrium pressure	Pa
P _e	Effective stress	Pa
p _m	Mean pore pressure	Pa
R	Gas constant	J mol ⁻¹ K ⁻¹
r	Geometric radius of a pore	m
r _{hyd}	Hydraulic radius of a pore	m
S _{pore}	Pore area	m ²
S _{mosaic}	Area of a mosaic map	m ²
T	Temperature	K
V _{void}	Void volume	m ³
V _{pore}	Pore volume	m ³
V _{bulk}	Bulk volume	m ³
V _{rc}	Reference cell volume	m ³
V _{sc}	Sample cell volume	m ³
VR _r	Vitrinite reflectance	%
w	Mean effective slit width	m
W _{dry}	Dry sample weight	kg
W _{sat}	Weight of water-saturated sample in air	kg
W _i	Weight of water-saturated sample immersed in water	kg
w _{TOC}	Mass fraction of total organic carbon	%
w _{clay}	Mass fraction of clay minerals	%
w _{rigid}	Mass fraction of rigid minerals	%
α	Stress sensitivity of permeability	Pa ⁻¹

β	Stress sensitivity of porosity	Pa^{-1}
γ	Porosity sensitivity exponent	-
ϕ	Porosity	-
ϕ_0	Porosity at zero effective stress	-
λ	Mean free path length	m
τ	Tortuosity	-
μ	Gas viscosity	$\text{kg m}^{-1}\text{s}^{-1}$
ρ_g	Free gas density	kg m^{-3}
ρ_a	Sorbed phase density	kg m^{-3}
ρ_w	Water density	kg m^{-3}
ρ_{bulk}	Bulk density	kg m^{-3}
TOC	Total organic carbon	%
TIC	Total inorganic carbon	%
TS	Total sulfur	%
AFM	Atomic force microscopy	
BSE	Backscattered electron	
BET	Brunauer-Emmett-Teller (physisorption theory)	
BIB	Broad ion beam	
BJH	Barrett-Joyner-Halenda (method for calculating pore volume distribution)	
DA	Dubinin-Astakhov (theory for micropore volume determination)	
DGR	Deep geologic repository	
EBS	Engineered barrier system	
EDZ	Excavation damaged zone	
EDX	Energy-dispersive X-ray	
FE	Field-emission	
FIB	Focused ion beam	
GRI	Gas Research Institute	
HIM	Helium ion microscopy	
HP	Helium pycnometry	
HLW	high-level radioactive waste	
ILW	Intermediate-level radioactive waste	
LPH	Low-pressure hysteresis	
LLW	Low-level radioactive waste	
Micro-CT	Micro computed tomography	
MIP	Mercury injection porosimetry	
NGBS	Natural geological barrier system	
PPR	Practical pore resolution	
RH	Relative humidity	
REV	Representative elementary volume	
REA	Representative elementary area	
ROI	Region of interest	
SEM	Scanning electron microscopy	
SE2	Secondary electron	
TEM	Transmission electron microscopy	
WIP	Water immersion porosimetry	
XRD	X-ray diffraction analysis	
WMI	Wood's metal injection	

1 INTRODUCTION

1.1 Energy policy in China

The current state of global warming and acute domestic air pollution have accelerated China’s energy transition from a coal-based energy system to a low-carbon energy system with less CO₂ emissions and a higher share of renewable energy (Li and Taeihagh, 2020). The share of coal in the China’ energy consumption mix has gradually decreased from 71.6% in 2009 to 59.0% in 2018, while the shares of natural gas and electricity generated from renewable energy sources (hydropower, wind power and solar power) as well as nuclear power have increased from 3.5% to 7.8% and 8.50% to 14.30% in 10 years, respectively (NBS, 2019; Fig 1.1). Compared to other fossil fuels, natural gas has the lowest CO₂ emissions and is projected to be in great demand in China based on its rapid increase in share. According to the EIA (2015), China possesses the largest technically recoverable amount of shale gas (31.6 trillion cubic meters) in the world. These resources could help the country to cut the coal’s share in the power sector and reduce strong reliance on import. Besides, to achieve the energy transition goals, the Chinese government also decided to increase the share of non-fossil energy (nuclear power and renewable energy) in the primary energy consumption to 15% by 2020 and 20% by 2030 (Guo and Guo, 2016).

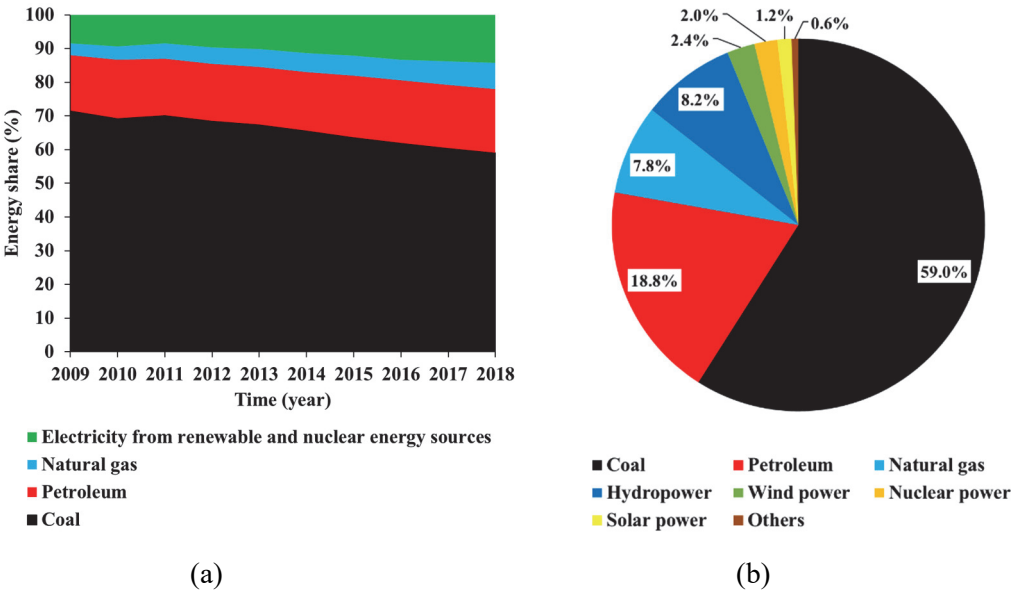


Figure 1.1 (a) The energy consumption mix of China from 2009 to 2018 (data from NBS, 2019); (b) A detailed energy consumption mix of China in 2018 (data from CEPI, 2019).

1.1.1 Nuclear power

Although most of the electricity in China is produced from coal (70.4% in 2018), the share of nuclear power in the total electricity generation capacity has increased rapidly from 1.8% in 2011 to 4.2% in 2018. This accounts for 14.2% electricity generation capacity from non-fossil sources (Fig 1.2; CEPI, 2019). Compared to hydro-, wind-, and solar power, nuclear power is more efficient in energy conversion, flexible and stable in operation and technically mature in China (Zhou et al., 2010; Guo and Guo, 2016). Currently, China has about 45 nuclear power reactors in operation and 12 under construction (WNA, 2020). However, the spent fuel generated from these nuclear power plants is expected to reach 83000 tons by 2050. It has to be reprocessed first, vitrified, and stored in geological repositories. The geological disposal of nuclear waste in China is expected to take place in three stages: (1) laboratory studies and site selection for high-level radioactive waste (HLW) repositories (2006-2020); (2) underground in-situ tests (2021-2040); (3) repository construction (2041-2050) (Faybishenko and Swift, 2016). A suitable site for HLW repository has been selected in Beishan, in the northwestern Gansu province in China. The candidate host rock is the Proterozoic granite, which is of high integrity and low fracture density, possesses very low hydraulic conductivity and is situated in an anticline with low seismicity.

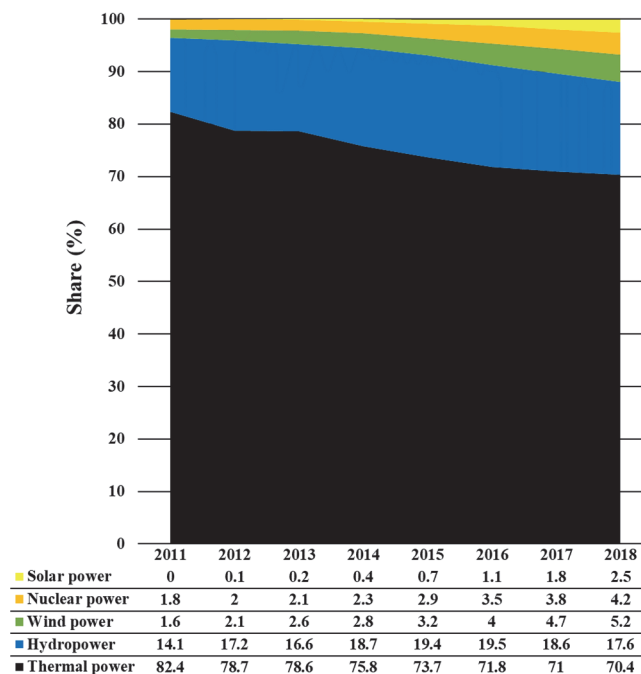


Fig 1.2 The mix of electricity generation capacity in China from 2011 to 2018 (data from CEPI, 2019).

1.1.2 Shale gas

The “Shale Gas Revolution” was initiated by the United States (US) and attracted enormous attention on the research of unconventional gas shale reservoirs worldwide. The shale gas production of the US in 2018 was 624.50 billion cubic meter (bcm) and accounted for 64.71% of its total natural gas production (EIA, 2019). Shale gas exploration and exploitation in China date back to 2009 and production progressed fast from 0.03 bcm in 2012 to 10.88 bcm in 2018 but is still in an initial stage when compared to the US (Fig 1.3; Dai et al., 2020; EIA, 2019). Shale gas production in China accounted for 6.8% of its total natural gas production in 2018. In 2012, the Chinese government introduced a series of policies including the setting of production targets, a production subsidy, waivers of price control and fees and the setting of shale gas as an independent mineral resource (Sandalow et al., 2014). Currently, major commercial shale gas production in China is limited to the Upper Ordovician Wufeng and Lower Silurian Longmaxi Formations. Therefore, an identification of additional shale gas prospects is currently prioritized in China.

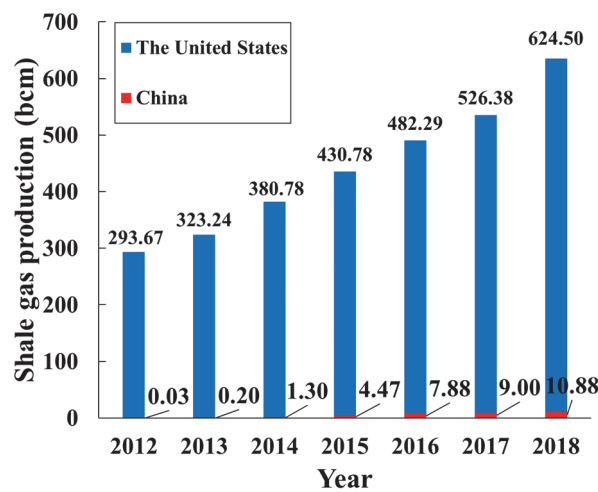


Fig 1.3 Comparison of the shale gas production between China and the US (data from EIA, 2019 and Dai et al. 2020).

1.2 Radioactive waste disposal

The management of radioactive waste varies from country to country and it may be quite different even in one country due to local factors. The management of radioactive waste is generally divided into two stages: predisposal and disposal (Faybishenko and Swift, 2016). The predisposal process includes decommissioning, pre-treatment, treatment, conditioning, immobilization, storage and transport. Disposal is the final stage of the management when

radioactive waste is placed in a designed disposal facility. It is sometimes acceptable for a small amount of effluents to be discharged into the environment within an authorized limit (Ojovan and Lee, 2014).

1.2.1 Sources of radioactive waste

We are living in a naturally radioactive world. In the 1930s, the Curies first discovered artificial radioactivity, which was then utilized in science, medicine, industry and agriculture (Zhou, 2010). However, the wide utilization of natural and artificial radioactivity inevitably leads to waste products, many of which contain high levels of radionuclides.

Basically, there are three main sources of nuclear waste: (1) the nuclear fuel cycle (NFC) in power generation and military uses; (2) non-NFC institutes (non-nuclear industries, medical and research institutions) and (3) accidents (Ojovan and Lee, 2014).

1.2.2 Classification of radioactive waste

The two main parameters considered in the classification of nuclear waste are the concentration and half-life of the radionuclide. Depending on its concentration, radioactive waste can be divided into exempt waste, low-level waste (LLW), intermediate-level waste (ILW) and high-level waste (HLW) (McKinley, 1992). Exempted waste usually has an activity level (concentration and total quantity) below the exemption level and is therefore excluded from regulatory control. As LLW has an activity level higher than the exemption level, it is assigned for landfilling. ILW has an activity level higher than LLW and needs to be isolated in handling or storage. Near-surface disposal can be applied on ILW with low content of long-lived radionuclides. HLW is generated in the nuclear fuel cycle and contains significantly higher activity level. Due to significant heat generation during radioactive decay, deep geological disposal is required for HLW (Ojovan and Lee, 2014).

Due to differences in the half-lives of radionuclides, radioactive waste can be further divided into short-lived and long-lived waste (Apted and Ahn, 2017). The short-lived waste contains low concentration level of radionuclides with half-lives longer than that of ^{137}Cs (30.2 years), while long-lived waste has a significant concentration of radionuclides with longer half-lives (Ojovan and Lee, 2014).

1.2.3 Radioactive waste disposal

To ensure long-term public safety and to create a sustainable environment for current and future generations, geologic disposal of radioactive waste is being planned in over 30 nations owning nuclear power plants. The planning involves feasibility evaluations, site selections, formation characterizations, program designs and licensing of geological repositories (Witherspoon and Bodvarsson, 2006). The first disposal facility was constructed in 1944 at Oak Ridge, Tennessee, USA, a trench filled with unconditioned waste (Ojovan and Lee, 2014). At present, waste disposal within deep geological storage facilities is being internationally developed. Deep geological disposal is based on a multi-barrier system consisting of engineered and natural geological barriers (Fig 1.4). An engineered barrier system (EBS) is composed of conditioned waste forms, a container, overpack, buffer, backfill and seal materials (Allan and Nuttall, 1997). The role of the EBS is to provide a complete containment of short-lived radionuclides and is especially important for near-surface repositories. Natural geological barrier systems (NGBS) consisting of the host rock and its surrounding formations, ensure isolation of radioactive waste from the biosphere and provide a stable and predictable environment. As potential host rocks, different lithologies such as granites, volcanic tuffs, lavas, clays, shales and limestones have been or are being investigated in many countries (Faybishenko and Swift, 2016). For salt and argillaceous rocks (clays or mudstones), isolation is guaranteed by an impermeable or low permeable matrix. With respect to granites and limestones that are prone to deform brittlely, isolation effects rely on engineered barriers. Another function of a multi-barrier system is retardation, which is achieved by a series of physical and chemical processes (e.g., sorption, complexation and precipitation) and takes place in the repository and geosphere. Furthermore, the concentration of radionuclides is diluted due to transport through large volumes of the host rock and surrounding formations (Apted and Ahn, 2017).

In this thesis, the host formation of particular interest is the Middle Ordovician Cobourg limestone from the Bruce nuclear site of Canada, which was proposed as a potentially safe setting for the construction of a deep geologic repository (DGR) for storage of low- and intermediate-level nuclear waste (NWMO, 2011). Since the main transport mechanism of radionuclides is via groundwater, isolation effects are related to the flow rate of the groundwater or the interstitial velocity. The interstitial velocity (v) is determined by the hydraulic conductivity (K), the porosity (ϕ) and the hydraulic gradient (∇H) (Eq.1). The hydraulic conductivity is related to the permeability (k) (Eq.2). Therefore, two of the most

important petrophysical properties of the host rock are the porosity and permeability.

$$v = -\frac{K}{\phi} \nabla H \quad (\text{Eq.1})$$

$$K = \frac{k\rho g}{\mu} \quad (\text{Eq.2})$$

Here ρ and μ represent the density (kg m^{-3}) and the viscosity ($\text{kg m}^{-1} \text{s}^{-1}$) of groundwater, respectively and g denotes the gravitational acceleration (m s^{-2}).

To date, several studies have revealed that the intact part of the Cobourg limestone can be classified as a “tight” rock due to low porosities (1.04-3.03%) and permeability coefficients (3.31×10^{-23} - $1.80 \times 10^{-21} \text{ m}^2$) (Vilks and Miller, 2007; Cavé et al., 2009; Letendre, 2011). In the context of the construction of deep geologic repositories, excavation of the underground will inevitably lead to stress re-adjustments which could potentially cause new rock failure and previous failure re-activation. Therefore, it is important to investigate the evolution of porosity and permeability of the host rock at different stress conditions.

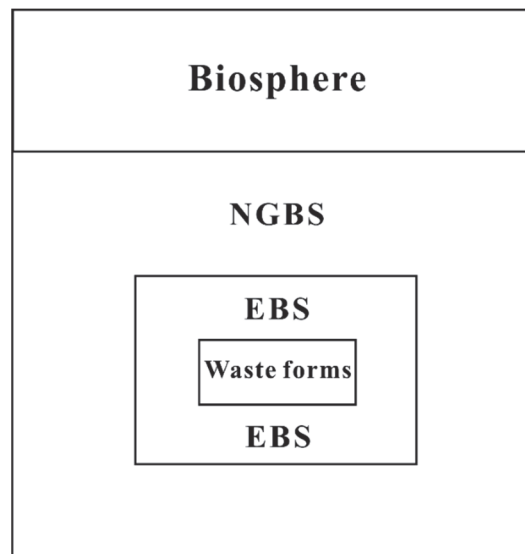


Fig 1.4 Simplified sketch of multi-barrier system in radioactive waste repositories.

1.3 Gas storage in shale gas reservoirs

Shale gas is defined as natural gas trapped in low-permeability shale formations. Typically, shales serve as source and reservoir rock. Shale gas is generally dominated by methane (90% or more) and generated in different stages of burial (biogenic gas, wet gas and dry gas) (Zou, 2017).

1.3.1 Pore classification

Unlike conventional porous media, pores in shales range greatly in size, connectivity, shape and occur in both inorganic and organic compositions (Tiab and Donaldson, 2015; Kelly et al., 2016). According to the classification of IUPAC, micropores are smaller than 2 nm, mesopores are in the range of 2-50 nm and macropores are larger than 50 nm (Sing, 1991). Klaver et al. (2015a) suggested that different compositions (clay-rich matrix, carbonates and solid bitumen) in shales show different pore size distributions. Loucks et al. (2009) utilized field-emission scanning electron microscopy (FE-SEM) to identify the pores of the Barnett shale. They observed that most of the pores in organic matter are intraparticle and have irregular, bubblelike or elliptical shapes, ranging between 5 and 750 nm. Loucks et al. (2009), Milliken et al. (2013) and Klaver et al. (2015a) found porosities extracted from images are significantly lower than porosities obtained from helium pycnometry (HP) or mercury injection porosimetry (MIP). These authors suggested that a number of pores in shale are not detectable under the resolution of SEM (5 nm). The complexity of pore structures in shales poses a major challenge in the consistency among core analysis methods.

Loucks et al. (2012) systematically classified the pores in shales into three types: interparticle mineral matrix pores, intraparticle mineral matrix pores and intraparticle organic-matter pores (Fig 1.5). These pores, along with natural fractures, form the flow path network in shales. In young shallow-buried muds, mineral matrix pores are abundant and interparticle mineral pores are more likely to form an interconnected and effective pore network than intraparticle mineral pores (Klaver et al., 2012). However, these pores diminish greatly with burial and compaction. During thermal maturation, intraparticle organic-matter pores develop and tend to form an interconnected network. Besides, intraparticle dissolution pores may also arise as acidic fluid is generated during decarboxylation of kerogen (Loucks et al., 2012; Tissot and Welte, 2013). Unlike the first two matrix-related pore types, fractures are not controlled by individual matrix particles and could play an important role in hydrocarbon transport and production (Slatt and O'Brien, 2011).

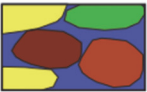


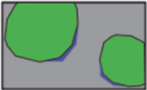
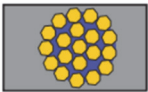
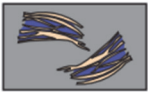
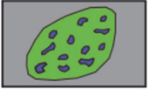
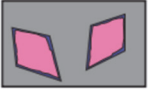
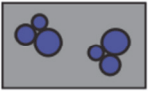
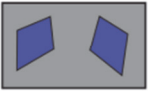



Mineral Matrix Pores Pores between or within mineral particles		Organic-Matter Pores Pores within organic matter	Fracture Pores Pores not controlled by individual particles
<p>Interparticle Pores</p>  <p>Pores between grains</p>  <p>Pores between crystals</p>  <p>Pores between clay platelets</p>  <p>Pores at the edge of rigid grains</p>	<p>Intraparticle Pores</p>  <p>Intercrystalline pores within pyrite framboids</p>  <p>Intraplatelet pores within clay aggregates</p>  <p>Pores within peloids or pellets</p>  <p>Dissolution-rim pores</p>  <p>Pores within fossil bodies</p>  <p>Moldic pores after a crystal</p>  <p>Moldic pores after a fossil</p>	<p>Organic-Matter Pores</p> 	<p>Fracture Pores</p> 

Fig 1.5 The classification of pore types in shales based on FE-SEM analysis (Loucks et al., 2012)

1.3.2 Gas storage mechanisms

Natural gas in shales can be stored in the free, dissolved and adsorbed states (Clarkson et al., 2016). Free gas is stored volumetrically in both pore and fracture space, whereas dissolved gas is the proportion of gas dissolved in formation water, liquid hydrocarbon or absorbed by kerogens. The enrichment of gas on the surface of organic matter or minerals is referred to as adsorbed gas (Gasparik et al., 2014; Clarkson et al., 2016). In this thesis, the term “sorption” covers any state of gas storage except for the free state because a differentiation between adsorption and dissolution is currently not possible in the laboratory.

Understanding the amount and relative proportion of gas stored in different states is critical for an accurate assessment of shale gas resources (Hao et al., 2013). Currently, isothermal high-pressure sorption experiments are widely applied to assess the maximum sorption capacity of shales (Gensterblum et al., 2009; Rexer et al., 2013). Methane sorption in shales is an exothermal physical process dominated by van der Waals forces between methane molecules and matrix particles. The sorbed methane molecules can overcome these forces and return to the bulk free phase when the temperature increases (Yang et al., 2018). Fig 1.6 shows

conceptual cylindrical and slit pore models in which free gas and sorbed gas occur. Influenced by van der Waals forces, some methane molecules accumulate on the pore walls and form a sorbed phase. With further distance from the pore walls, methane molecules are not attracted by the force field and therefore occur as free gas. As sorption is a dynamic physical process, a portion of methane molecules exists in the sorptive space but belongs to the bulk free phase. The excess sorption capacity is defined as the amount of gas with density higher than the bulk free phase density, while the absolute sorption capacity refers to the total amount of gas in the sorption space. Therefore, a volume correction is essential for accurate excess sorption measurements (Eq.3; Feng et al., 2020). Generally, methane sorption capacity is controlled by (1) the nature of organic matter (richness, type and maturity), (2) clay minerals (content and type), (3) moisture, (4) pressure, (5) temperature and overburden stress (Zhang et al., 2012; Ji et al., 2012; Gasparik et al., 2014; Merkel et al., 2015a; Yang et al., 2015; Yang et al., 2018; Gaus et al., 2021).

$$n_{excess} = n_{abs} - V_a \rho_g = n_{abs} \left(1 - \frac{\rho_g}{\rho_a}\right) \quad (\text{Eq.3})$$

Here, n_{excess} (mmol/g) and n_{abs} (mmol/g) denote the excess sorption capacity and absolute sorption capacity, respectively. V_a (m³), ρ_g (kg/cm³) and ρ_a (kg/cm³) represent the sorption volume, the free phase density and the sorptive phase density, respectively.

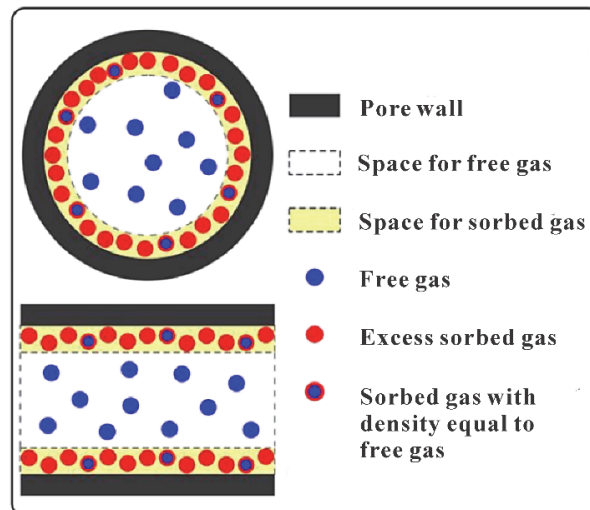


Fig 1.6 Cylindrical and slit pore models illustrating gas storage mechanisms in shales (Feng, et al., 2020).

The free gas storage capacity can be evaluated in the laboratory by determination of the pore volume, which can be achieved by various techniques. Petrophysical techniques involve direct fluid invasion such as helium pycnometry (HP), mercury injection porosimetry (MIP), water

immersion porosimetry (WIP) as well as low-pressure N₂ and CO₂ adsorption experiments. Other indirect imaging techniques include scanning electron microscopy (SEM), transmission electron microscopy (TEM), helium ion microscopy (HIM), atomic force microscopy (AFM) and micro-computed tomography (micro-CT) (Klaver et al., 2012; Keller et al., 2013; Kuila et al., 2014; Seemann et al., 2017). Advantages and limitations of these techniques will be analyzed in the next section.

1.4 Comparison of core analysis techniques

In fine-grained mudstones or claystones, the majority of the pores are in the nanometer scale and have a wide range of connectivity and shape, with different pore size distributions in different compositions (Keller et al., 2013; Klaver et al., 2015a; Kelly et al., 2016). Complex pore structures and the heterogeneity of the rock matrix pose challenges with regard to the consistency of porosity and permeability measurements by petrophysical and imaging techniques.

1.4.1 Porosity measurements

Direct fluid-invasive petrophysical techniques, including HP, MIP, WIP, low pressure N₂ and CO₂ sorption measurements, are utilized to determine the accessible and connected pore volume of rocks. As helium has access to pores down to 0.26 nm, the largest range of pore sizes is theoretically detected by HP but no direct information about the pore geometries and connectivity is given (Busch et al., 2016). The pore size distributions obtained from MIP and low-pressure N₂/ CO₂ adsorption experiments are based on assumptions of “uniform” cylindrical or slit-shaped pores, which can only be regarded as estimates. Besides, the validity of pore size distributions from MIP measurements is controversial because of mercury pressure induced deformations and wrong assignments of pore volume to pore sizes due to the "ink-bottle" effect (Hildenbrand and Urai, 2003). It should be noted that information on the pore morphology, connectivity, porosity and pore size distribution in specific minerals or compositions are absent in these evaluations.

With the development of new imaging technologies over the past years, such as TEM, HIM and AFM, much higher resolution and better-quality images as compared to SEM were achieved (Kelly et al., 2016). Pore morphology, porosity and pore size distribution can be analyzed for specific minerals or compositions. However, the view fields of these methods are limited to a small scale (μm^2) and 2D. BIB-SEM complements the preceding methods by

imaging large ($>mm^2$) and undamaged planar surfaces, allowing for a qualitative and quantitative solution for pore structure characterization (Klaver et al., 2012; Klaver et al., 2015a; Philipp et al., 2017). Nevertheless, the connectivity of pore space in 3D cannot be investigated. Focused ion beam milling-scanning electron microscope (FIB-SEM) offers serial and simultaneous sectioning and imaging, generating a sequence of high-resolution SEM images (down to a few nanometer) with uniform spacing and enabling 3D visualization of minerals, organic matter and pores. However, deviation of porosity values obtained from the restricted volumes (hundreds of μm^3) can be greater than 5%, which is in the order of magnitude of the porosity values for tight shales (Kelly et al., 2016). Keller et al. (2013) also reported that the porosity values determined from FIB-SEM reconstructions of the Opalinus Clay (about 300 μm^3) are only 20-30% of those determined from low-pressure N_2 adsorption experiments. Low-pressure N_2 adsorption captures much smaller pores which cannot be visualized by FIB-SEM.

1.4.2 Permeability measurements

A conventional permeability measurement is conducted on cylindrical samples in pseudo-triaxial flow cells. In that way, artificially created microfractures can be closed and the in-situ permeability of the sample plug can be determined with liquid or gas as the permeating fluid. Steady state and non-steady state methods can be applied for such measurements. For low and ultra-low permeability rocks, non-steady state methods (pulse decay) are preferred due to shorter measuring times as compared to steady state methods (Ghanizadeh et al., 2014). Nevertheless, these methods are very sensitive to leaks and a long time frame is required for system equilibration before the measurements. Besides, both methods do not strictly yield the same results even if the same gas is used (Sander et al., 2017). A technique known as the Gas Research Institute (GRI) technique is a derivation of the pulse decay method, which is used for permeability measurements of crushed rocks. Compared to the core plug measurement, the GRI measurement is much faster and cheaper. However, the GRI technique is conducted without a confining pressure and thus does not reflect in-situ permeability. The variation of permeability coefficients is more than two orders of magnitude when particle sizes vary from 0.7 mm to 7 mm (Tinni et al., 2012). Additionally, for all above-mentioned methods, the permeating fluid (liquid vs gas; different gas types) influences the resulting permeability coefficients. The sample preparation in different laboratories also affects the measurement, e.g., different preferential particle sizes of crushed rocks for GRI, dry or moisturized core samples (Tinni et al., 2012; Ghanizadeh et al., 2014; Fink et al., 2017). In summary, a lack of universal measuring standards leads to an inconsistency of experimental permeability measurements on low

permeability rocks.

For conventional microporous rocks like sandstones, micro-CT is successfully applied to capture a representative elementary volume (REV) and generate a 3D pore network on which permeability simulations can be performed (Mostaghimi et al., 2013; Philipp et al., 2017; Saxena et al., 2017). Mostaghimi et al. (2013) applied a finite difference method for permeability simulation of sandpacks and sandstones based on micro-CT images. The simulated permeability coefficients agree well with laboratory measurements and a linear dimension of 0.8 mm was recommended for the REV of the Berea sandstone. Saxena et al. (2017) compared permeability coefficients from laboratory measurements on sandstones with mean values of numerically computed permeabilities using various solvers and found a general good agreement. However, the resolution limitation of micro-CT is particularly significant when it comes to the imaging of nanopore networks. Curtis et al. (2012) analyzed the 3D pore network of FIB-SEM reconstructions ($125 \mu\text{m}^3$) of shales. They observed no connected pore network across a whole reconstructed volume. Kelly et al. (2016) reconstructed FIB-SEM volumes of shales and observed that each FIB-SEM domain contains thousands of independent pore networks and only a few key tortuous percolation pathways. The permeability coefficients obtained from the croppings of domains in at least one direction show variations up to three orders of magnitude. They concluded that the volume of FIB-SEM stacks below $5000 \mu\text{m}^3$ should not be considered as a REV for shale permeability evaluations. Sampling such large volumes of rocks with high resolution will inevitably lead to significant increased time in both milling and imaging procedures. The flow simulation will also be computationally expensive. Permeability simulations on FIB-SEM image stacks of nanoporous rocks are still challenging, especially in finding a balance between resolution and domain size (Bultreys et al., 2015)

1.5 Main objectives and thesis overview

This thesis is composed of 5 chapters with different focuses. The first chapter gives a concise introduction of the background and highlights the significance of this thesis. The subsequent three chapters (chapter 2-4) are focusing on topics in the form of research papers. Chapter 5 presents a summary and gives an outlook.

Chapter 2 was published as Hu, Z., Klaver, J., Schmatz, J., Dewanckele, J., Littke, R., Krooss, B.M., Amann-Hildenbrand, A., 2020. Stress sensitivity of porosity and permeability of

Cobourg limestone. *Engineering Geology*, 105632.

In the context of the construction of a deep geological repository for radioactive waste, understanding the evolution of the porosity and permeability of host rock under loading conditions is critical for providing data for performance assessment modelling. Experimental permeability measurements of low permeability sedimentary rocks face challenges: (1) widely applied steady state and non-steady methods do not always yield the same results; (2) permeating fluids affect the measurements and (3) sample preparations in different laboratories influence the measurements. A lack of universal measuring standards for low permeability rocks affects the comparability between results. Therefore, this study is part of a benchmark study aiming at the comparison of permeability data of the Cobourg limestone measured in 28 laboratories. In this study, a series of porosity and permeability measurements were conducted on four Cobourg samples at different stress states using different methods.

Chapter 3 was prepared as Hu, Z., Klaver, J., Dewanckele, J., Littke, R., Amann-Hildenbrand, A., 2020. Multi-scale characterization of petrophysical properties of Cobourg limestone – potential nuclear waste host rock in Canada.

The Cobourg limestone can be characterized as a low porosity and permeability sedimentary rock with distinct macroscopic heterogeneity, posing a challenge to obtain a representative elementary area or volume for both imaging analyses and petrophysical tests on the Cobourg limestone. Thus, analyzing the pore morphology and pore structure of the petrology homogeneity zones is crucial for understanding the potential fluid transport pathways of Cobourg limestone. Multiple imaging techniques (micro-CT, BIB-SEM, FIB-SEM) were utilized to characterize the petrophysical properties and compared with bulk measurements based on petrophysical techniques.

Chapter 4 was published as Hu, Z., Gaus, G., Seemann, T., Zhang, Q., Littke, R., Fink, R., 2021. Pore structure and sorption capacity investigations of Ediacaran and Lower Silurian gas shales from the Upper Yangtze platform, China. *Geomechanics and Geophysics for Geo-Energy and Geo-Resources*, 7(3), 1-26.

Shale gas exploitation in China is currently limited to shales from the Upper Ordovician and Lower Silurian (Wufeng and Longmaxi Formations). Therefore, the identification of additional shale gas prospects is currently prioritized in China. To evaluate the gas storage capacity of Ediacaran shales, this study, for the first time, investigated its pore structure and methane

sorption capacity and compared them with the commercially successful Lower Silurian Longmaxi shale in Upper Yangtze platform of China. The controlling factors (e.g. TOC content, clay content, moisture, thermal maturity, micropore volume) on sorption capacity for the two sets of shales were also discussed.

Chapter 5 deals with a final general discussion of the thesis and gives the following recommendations for future work.

The behavior of competitive sorption of CH₄ and CO₂ on shales has great potential to be utilized in enhanced shale gas recovery (ESGR). However, experimental measurements are widely conducted on crushed rocks at unconfined conditions. Whether the sorption selectivity parameter is different for competitive sorption on core plugs at in-situ stressed states needs to be examined in a future study.

Considering the occurrence of open stylolites and fractures, the matrix permeability of Cobourg limestone should not be considered as a critical factor for the sealing efficiency of the host rock. Therefore, the mechanism of gas migration in damaged Cobourg limestone needs to be investigated for the safety assessment of a radioactive waste repository.

Traditional experimental studies of fluid transport through geomaterials cannot provide solid evidence of microstructural changes of core samples under the impact of temperature and stress during the measurements. The combination of a triaxial flow cell and a micro-CT scanner is recommended for studying fluid transport properties of organic-rich immature shales as a function of temperature at confined conditions.

2 STRESS SENSITIVITY OF POROSITY AND PERMEABILITY OF COBOURG LIMESTONE

Keywords: Ordovician Cobourg limestone; Porosity; Permeability; Stress sensitivity; BIB-SEM; Stylolite

ABSTRACT

We have analysed the stress sensitivity of porosity and permeability of macroscopically intact limestone samples, from the Middle Ordovician Cobourg Formation, Ontario, Canada. This limestone is a potential host formation for geological storage of low- and intermediate-level nuclear waste. Porosity and permeability were measured with gas (helium) on dry cylindrical plugs under defined isostatic stress conditions. Measurements were performed only during the second loading and unloading paths (5-20 MPa) to minimize the impact of fissures induced by sample preparation.

All samples have porosity values of less than 2%. The Klinkenberg-corrected permeability coefficients of three adjacent samples drilled from one cubic block in different orientations span one order of magnitude (2.3×10^{-19} - 2.0×10^{-20} m²). The transport porosity of these samples is dominated by slit-shaped pores and micro-fractures within the clay matrix. Much higher permeability coefficients (1.5×10^{-17} - 6.2×10^{-18} m²) were measured on another sample containing open stylolites, as identified by X-ray Computed Tomography (micro-CT) and broad ion beam milling-scanning electron microscopy (BIB-SEM). Stress sensitivity coefficients of permeability range from 3.0×10^{-2} to 7.1×10^{-2} MPa⁻¹, those of porosity from 3.9×10^{-3} - 9.8×10^{-3} MPa⁻¹. A loading hysteresis effect was observed with permeability coefficients along the unloading path, up to 47% lower than values on the loading path. This is taken as an indication for creep. Due to the occurrence of stylolites in this limestone sequence, the matrix permeability is not considered as a critical factor for the sealing efficiency.

2.1 Introduction

The study of low-permeable sedimentary rocks is receiving increasing attention worldwide in the context of radioactive waste disposal (McKinley, 1992; Allan and Nuttall, 1997; Loubergé et al., 2002; Fall et al., 2014), CO₂ sequestration (Bachu, 2000; Jafari et al., 2016) and tight gas and shale gas exploitation (Zhang et al., 2016; Mahanta et al., 2017). For the storage of hazardous radioactive waste, the disposal within deep geological storage facilities is under examination (Allan and Nuttall, 1997; Fyfe, 1999). Such storage facilities consist of a multi-barrier system, i.e. engineered and natural geological barriers, which must effectively prevent migration of radionuclides over a time frame of 1 million years. So far, various types of potential host rocks have been or are being investigated in different countries. Canada, China, Finland, Russia and Sweden considered granitic rocks (IAEA, 2001). Volcanic tuffs and lavas were studied by the USA and the UK (Birkholzer et al., 2012). Clay and shale were prioritised in Belgium, Hungary, France and Russia (Ojovan and Lee, 2014). In Canada, focus was initially put on the granitic formations of the Canadian Shield, but lately the Canadian agencies shifted their attention towards the Ordovician argillaceous limestones in southern Ontario (Selvadurai and Głowacki, 2016). The formation of particular interest is the Middle Ordovician Cobourg Limestone at Bruce nuclear site. Based on its high lateral stability, extremely low horizontal and vertical hydraulic conductivity and verticle multiple low permeability barriers, it is proposed as a safe potential setting for the construction of a deep geologic repository (DGR) for the storage of low- and intermediate-level nuclear waste (NWMO, 2011). Since the construction of a DGR requires the excavation of the underground, it will inevitably lead to stress re-adjustments which could potentially cause new rock failure and previous failure re-activation. Therefore, it is of utmost importance to investigate the porosity and permeability evolution of Cobourg limestone at different stress conditions. The influence of stress on the permeability of sedimentary rocks was first documented by Fatt and Davis (1952). On sandstones, they observed an 11-41% permeability reduction at 21 MPa confining pressure. During the following decades, a range of permeability experiments on various rocks were conducted to study the evolution of permeability and porosity with changing stress. David et al. (1994) proposed three types of permeability reduction behavior induced by compaction for sandstones. In the plots of permeability versus effective stress, Type I is characterized by decreasing stress sensitivity with increasing stress. For Type II, the stress sensitivity is relatively low and shows no significant variation with stress. The stress sensitivity of Type III abruptly increases at a critical effective stress. In order to evaluate the integrated effect of the

external confining pressure and internal pore pressure on permeability, the effective stress coefficient was discussed by Terzaghi (1936), Kwon et al. (2001), Ghabezloo et al. (2009), Heller et al. (2014) and Fink et al. (2017). Various empirical and theoretical models have been proposed to characterize the stress sensitivity of permeability and porosity, for example, the natural logarithm model by Walsh (1981), the power law model by Shi and Wang (1986), the exponential function model by Katsube et al. (1991), the cubic law model by Kwon et al. (2004), the Two-Part Hooke's model by Zheng et al. (2015). Farquhar et al. (1993) observed that low permeability sandstones deposited in similar depositional environments possess similar degrees of stress sensitivity. Brower and Morrow (1985) attributed the stress sensitivity of permeability to the pores with high aspect ratio. Li et al. (2013) observed that the stress sensitivity of pore volume in low rank coals is mainly controlled by microfractures and cleats. With respect to medium and high rank coals, the micropores, mesopores and macropores are more sensitive to stress. Kwon et al. (2004) and Chalmers et al. (2012) found that the permeability parallel to bedding is more stress sensitive than permeability perpendicular to bedding. Ghanizadeh et al. (2014) and Gensterblum et al. (2015) reported higher stress sensitivity with the presence of water in shale pore system. In addition, Kilmer et al. (1987) and Kwon et al. (2004) stated that permeability is more stress-sensitive along the first loading path due to long-term stress relaxation. Most of the above-mentioned studies were conducted on sandstones or shales. So far, only a few studies were performed on tight limestones (Letendre, 2011; Selvadurai and Głowacki, 2016; Głowacki and Selvadurai, 2016).

In the context of a benchmark study aiming at the comparison of permeability data measured in different laboratories, a set of homogeneous low-permeable Cobourg limestone samples was collected and distributed among 28 laboratories (Davy et al., 2019). The main objective of this collaborative study was to validate the experimental procedures and to identify the influencing factors. A series of porosity and permeability measurements were conducted on four samples at different stress states using different methods. Here we discuss porosity and permeability development during cyclic loading process, supported by microstructural analyses (micro-CT and BIB-SEM). The gas slippage data at different stress states were used to analyse the development of pore structure with stress and the results were compared with pore geometries derived from BIB-SEM analyses.

2.2 Theory

2.2.1 Stress dependence of permeability and porosity

The most common and widely used models to describe the stress-dependence of permeability coefficients of rocks are the power law function (Shi and Wang, 1986) (Eq.1) and the exponential function (Katsube et al., 1991) (Eq.2).

$$k = k_0 P_e^{-p} \quad (\text{Eq.1})$$

Here k_0 is the permeability (m^2) at atmospheric pressure, taken as 0.1 MPa, k denotes the permeability (m^2) under the effective stress P_e (Pa) and p is an adjustable dimensionless parameter describing the stress sensitivity.

$$k = k_0 \exp(-\alpha P_e) \quad (\text{Eq.2})$$

In equation 2, the stress sensitivity is described by the adjustable parameter α (Pa^{-1}), which also denotes the compressibility coefficient.

The relationship between porosity and effective stress can be similarly described by either a power law (Eq. 3) or an exponential function (Eq. 4).

$$\phi = \phi_0 P_e^{-q} \quad (\text{Eq.3})$$

$$\phi = \phi_0 \exp(-\beta P_e) \quad (\text{Eq.4})$$

Here ϕ_0 is the porosity (%) at zero effective stress and ϕ denotes the porosity (%) under the effective stress P_e (Pa). The stress sensitivity of the porosity is expressed by the adjustable parameter q in equation 3 and the parameter β (Pa^{-1}) in equation 4, respectively.

2.2.2 Gas permeability

In contrast to the viscous flow of a liquid (i.e. Poiseuille law), the flow velocity of a gas phase at the pore walls is not zero, which results in a larger average flow velocity. This phenomenon was already described by Kundt and Warburg (1875). They described gas flow through a porous system by introducing a “slip coefficient” that is proportional to the mean free path length of the gas. Klinkenberg (1941) applied this concept systematically to determine the permeability of rocks. Permeability coefficients determined with gases typically show a decrease with increasing mean gas pressure. This results in a linear relationship between the

“apparent” permeability coefficient k_{gas} (m^2) and the inverse of mean pore pressure p_m (Pa), commonly referred to as the “Klinkenberg” relationship. Extrapolation to an “infinite” mean pore pressure yields the limiting value k_∞ (m^2), known as the Klinkenberg-corrected or intrinsic permeability coefficient (Eq.5):

$$k_{gas} = k_\infty \left(1 + \frac{b}{p_m}\right) \quad (\text{Eq.5})$$

The parameter b is the gas slippage factor (Pa), which quantifies the variability of apparent permeability due to the Klinkenberg effect at low pore pressures (Klinkenberg, 1941; Letham and Bustin, 2016). It is related to the size of the transport pores (Eq.6). Assuming the pore system is made up of cylindrical pores, the average effective pore diameter can be calculated from the slippage factor using the approach by Klinkenberg (1941):

$$d = \frac{8c\lambda p_m}{b} \quad (\text{Eq.6})$$

Here d (m) is the mean effective pore diameter, c is the Adzumi constant (0.9, Adzumi, 1937) and λ (m) is the mean free path length.

Since slit-shaped pores are more common than cylindrical pores in tight rocks, the average effective pore size of slit-shaped pores can also be calculated based on the theory from Randolph et al. (1984):

$$w = \frac{16c\mu}{b} \sqrt{\frac{2RT}{\pi M}} \quad (\text{Eq.7})$$

where w is the mean effective slit width (m), μ is the gas viscosity ($kg\ m^{-1}s^{-1}$), R is the gas constant ($J\ mol^{-1}K^{-1}$), T is the temperature (K), and M is the molar mass of the gas ($kg\ mol^{-1}$).

In the past, several fracture models were applied to estimate the permeability of fractured rocks, like the parallel plate model of Snow (1965), the longitudinal crack model of Jones (1975), the “bed of nails” model described by Gangi (1978) and the fracture density based model of Zimmermann et al. (2005). Jones (1975) (Eq.8) related the fracture aperture with the permeability for a cylindrical rock sample containing a longitudinal fracture.

$$k = \frac{w^3}{3\pi D} \quad (\text{Eq.8})$$

Here, w is the fracture aperture (m) and D is the diameter (m) of the cylindrical rock.

2.3 Samples and methods

2.3.1 Geological setting

The Cobourg limestone is part of the Middle Ordovician Formation in the Michigan Basin (Xiang et al., 2013). At the Bruce nuclear site of Kincardine, Ontario, the Cobourg limestone is found at about 680 m depth and has a thickness of 28.6 m (Fig 2.1).

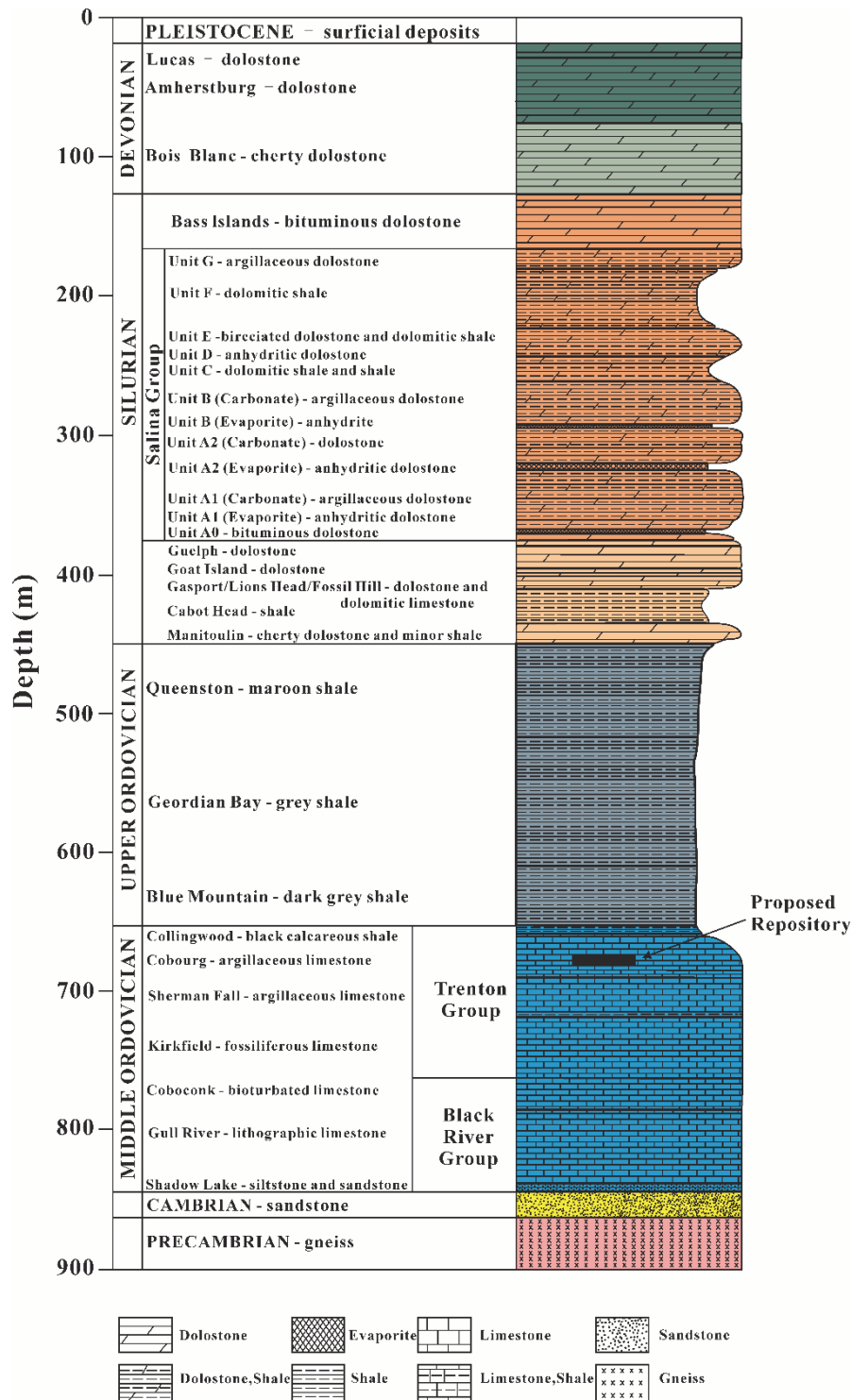


Fig 2.1 Stratigraphic column at Bruce nuclear site (modified after Beauheim et al.2014).

The Ordovician stratigraphy is composed of two parts with significantly different lithologies. The upper Ordovician unit featuring shale rocks is made up of the Blue Mountain, Georgian Bay, and Queenston Formations. The middle Ordovician unit, characterized by limestones with different contents of argillaceous sediment, is subdivided into the Black River and Trenton groups. They were deposited during a major marine transgression, covering the eroded Cambrian sandstone. The Cobourg limestone, which belongs to Trenton group, is described as a grey, fine-grained to argillaceous limestone with nodular texture (Nasseri et al., 2013; Petts et al., 2017). It is underlain by 150 m of low-permeable limestones and covered by more than 200 m of tight shales. The Cobourg limestone is considered by the Nuclear Waste Management Organization (NWMO) as a possible host rock for storing low- and intermediate-level waste because of multiple natural geological barriers, high lateral stability and extremely low hydraulic conductivity.

2.3.2 Sample material

The block sample was extracted from a shallow depth of about 70 m at the Saint Mary’s cement quarry in Bowmanville, Ontario (Fig 2.2). The quarry is on the northern shore of Lake Ontario and located on the margin of Northern Appalachian Basin. It is in 200 km distance from the Bruce nuclear site.

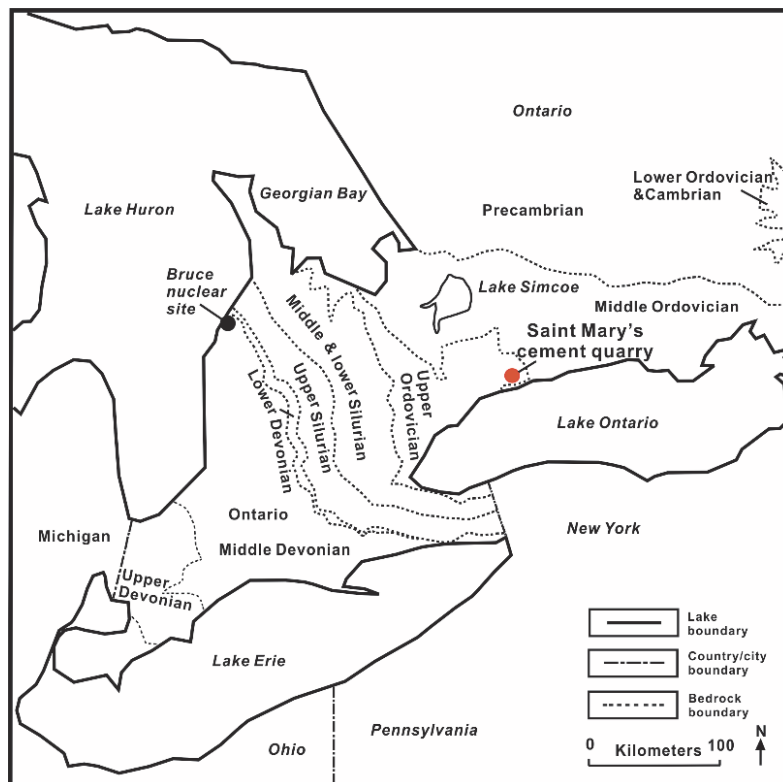


Fig 2.2 Sample location and generalized bedrock geology (modified after Xiang et al. 2013).

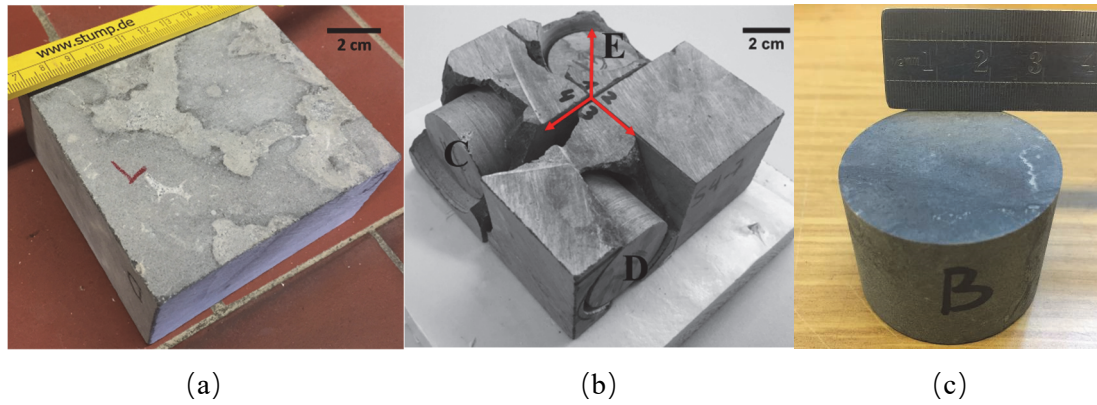


Fig 2.3 (a) The sample cube displaying macroscopically observable heterogeneity; (b) Cylindrical samples of C, D and E drilled in three mutually perpendicular directions as indicated by red arrows; (c) Cylindrical sample B with white strip on the top surface.

The Cobourg limestone was deposited in a supratidal- or tidal-flat to lagoonal marine setting and has been strongly reworked during storm floods (Nasseri et al., 2013; Petts et al., 2017). Clear bedding planes are therefore not discernible. It is a light grey nodular limestone, showing macroscopically observable heterogeneity (Fig 2.3a). In total, three cylindrical samples (C, D and E) were drilled from one dm-sized sample cube in three directions in the geotechnical laboratory of RWTH Aachen University (Fig 2.3b). Sample B was drilled and provided by the Structural Engineering Laboratory of McGill University (Fig 2.3c). As tests performed in this study were done with gas (helium) as the permeating medium, all samples were dried under vacuum at 105 °C for at least 24 h prior to the porosity and permeability measurements.

2.3.3 X-ray diffraction analysis (XRD)

X-ray diffraction patterns measured on milled and sieved rock powders were used to analyse the bulk mineralogical composition. The measurements were conducted in a Huber MC9300 diffractometer and quantitative phase analysis was processed on BGMN software. Details of sample preparation and measurement are reported in Gasparik et al. (2014).

2.3.4 Micro-CT

Micro-CT is widely used to reveal the 3D structure of geomaterials with a resolution scale from (sub-) micrometer to millimeter (Cnudde and Boone, 2013). The fundamental principle is that the intensity of X-rays radiating from the source would be attenuated when crossing through the specimen. The attenuation depends on the material density and the composition (atomic number). In a cone beam geometry, the resolution mainly depends on the position of the specimen between the X-ray source and detector: the closer to the X-ray source, the higher the

magnification and thus the higher the spatial resolution of the scan. Hence, the smaller the sample, the better the resolution will be. All samples were scanned before or after the petrophysical tests at UGCT (Centre for X-ray Tomography of Ghent University). The samples were scanned on the in-house developed scanner HECTOR, operating at 160 kV and a resolution of 44 μm . A 1 mm Cu filter was used to pre-harden the X-ray beam. Details of the setup and operation are documented in Masschaele et al. (2007) and Dierick et al. (2013).

2.3.5 BIB-SEM

BIB-SEM analyses were undertaken after petrophysical measurements, obtaining microstructural information down to the 10th nm-range. Based on the micro-CT data, a thin slab with a thickness of about 4 mm was cut from sample B with a diamond-blade saw. The cross-section area was then polished with an Ar-Ion BIB-polisher (Leica TIC 3X with a rotary stage) for 8 hours at a low angle and 5 KV acceleration voltage, resulting in a clean and smooth surface (Grobe et al., 2017). In addition, BIB cross-sections of sister samples were prepared at a high angle in a JEOL SM-09010 polisher. The BIB polished cross-sections were subsequently coated with tungsten and imaged in a Zeiss Supra 55 SEM (Klaver et al., 2012). Low-resolution overview backscattered electron (BSE) images and energy-dispersive X-ray spectroscopy (EDX) maps were acquired for studying the mineral phase distribution. Secondary electron (SE2) images were prepared and used for the analysis of micro-fractures and pores. As the sample material is heterogenous and relatively large, only selected areas of interest were investigated at high resolution.

2.3.6 Porosity measurements

2.3.6.1 Helium pycnometry

Helium pycnometry is a technique based on Boyle's law and is used to measure the grain density of rock samples. A standard helium pycnometer consists of a reference cell, a sample cell, a pressure transducer and three valves (Fig 2.4). The volumes of both sample and reference cells (V_{sc} and V_{rc}) were calibrated and a leak test was performed prior to the measurements. The experimental procedure consists of repetitive helium expansions from the reference cell into the sample cell. From the recorded pressures before and after equilibration, the mass transfer is calculated and converted to the void volume ($V_{sc}-V_s$) of the sample cell (Eq.9) where V_s is the skeletal volume.

$$V_s = V_{sc} - \frac{P_{rc} - P_{eq}}{P_{eq} - P_{sc}} V_{rc} \quad (\text{Eq.9})$$

Here P_{rc} and P_{sc} denote the pressures (Pa) of reference cell and sample cell before the gas expansion and P_{eq} represents the subsequent equilibrium pressure (Pa) of the whole system after gas expansion. When the bulk volume (V_b) is known, porosity can be calculated (Eq.10). The bulk volume is either calculated from the dimensions of the cylindrical plug determined by caliper measurements or by water immersion porosimetry (see 2.3.6.2).

$$\phi = \frac{V_b - V_s}{V_b} \quad (\text{Eq.10})$$

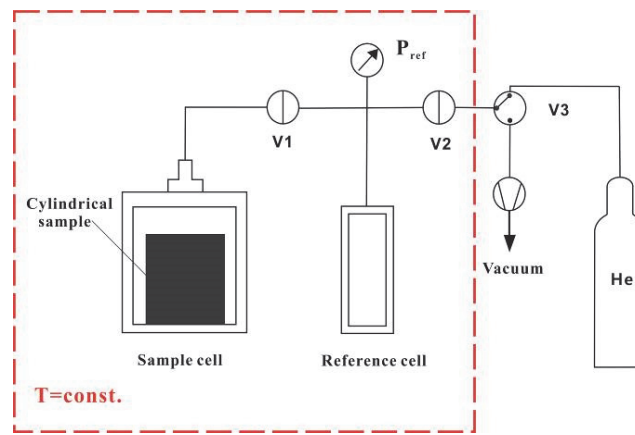


Fig 2.4 Sketch of the helium pycnometer for porosity measurements under unconfined conditions.

Porosity measurements at defined confining pressures follow the same procedure and are conducted in a triaxial flow cell (Fig 2.5). The reference cell volume (V_{rc}) consists of the volume between valves 1, 2 and 3. As a prerequisite, the system must be carefully calibrated, which is done by using a steel plug at similar confining and gas pressures as used in the actual porosity tests. The calibrated “dead” volume (V_{dead}) is subtracted from the volume detected when a sample is installed, yielding the pore volume (V_{pore}) of the sample (Eq.11).

$$V_{pore} = \frac{P_{rc} - P_{eq}}{P_{eq} - P_{up}} V_{rc} - V_{dead} \quad (\text{Eq.11})$$

The pressures (Pa) in reference cell and top and bottom compartments (P_{rc} , P_{up} and P_{down}) are recorded by PMP 4070 pressure transducers with an accuracy of 0.04% of the full-scale value (70 MPa).

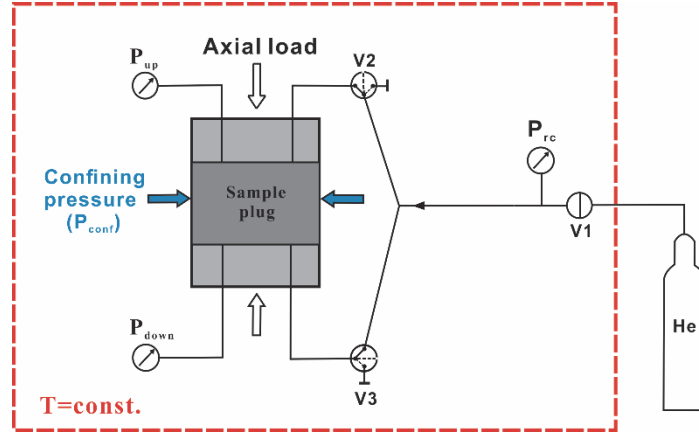


Fig 2.5 Sketch of the system used for pore volume and permeability measurements under defined confining pressures.

2.3.6.2 Water immersion porosimetry (WIP)

Porosity at unconfined conditions was also determined by water immersion porosimetry. Based on Archimedes' principle, the pore volume (V_{pore}) can be determined from the weight difference of the dry sample (W_{dry}), and the water-saturated sample in air (W_{sat}) (Eq.12). The bulk volume (V_{bulk}) is derived from the weight difference of the water-saturated sample in air (W_{sat}) and the water-saturated sample immersed in water (W_i) (Eq.13).

$$V_{pore} = \frac{W_{sat} - W_{dry}}{\rho_w} \quad (\text{Eq.12})$$

$$V_{bulk} = \frac{W_{sat} - W_i}{\rho_w} \quad (\text{Eq.13})$$

The dry weight was obtained after drying in a vacuum oven at 105 °C for at least 24 h to completely remove the remaining moisture. Before water saturation, the samples were degassed under vacuum (≤ 800 Pa) overnight. Afterwards, they were saturated with deionized water at atmospheric pressure (~ 0.1 MPa) for 22 days. Thereafter the samples were transferred into an isostatic pressure cell, where periodical pressure pulses of 15 MPa were applied for at least 3 days. Before measuring the saturated weight in air, the excess water was removed from the outside of the plug with a wet tissue. The weight was determined with an electronic balance with a maximum capacity of 320 g and a precision of 0.1 mg.

2.3.7 Gas permeability measurements at controlled stress

The triaxial flow cell was also used for gas permeability measurements at defined pressure and temperature conditions (Fig 2.5). In this study, three different non-steady state methods were applied: the conventional pulse decay (PD) method, the constant downstream pressure (CDP) method and the constant upstream pressure (CUP) method .

The principle of the first method is to create a pressure difference across the sample, which is allowed to equilibrate with time (Fig 2.6). As the volumes of the upstream and downstream pressure sides are closed, pressure will subsequently decrease and increase, respectively. The mean pressure remains constant throughout the experiment. In order to account for the slip flow, several measurements have to be performed at different mean pressures. In contrast, in the other two techniques, either the upstream or downstream pressure is held constant, which results in a changing mean pressure as pressure equilibrates. This allows for the construction of a Klinkenberg plot from only one pressure cycle. In order to maintain the downstream pressure constant, the downstream side is opened to the atmosphere. Constant upstream pressure is realized by connecting the upstream pressure side with the gas bottle equipped with a pressure regulator. One shortcoming of the CUP and CDP methods is that a mass balance cross-check between the upstream and downstream compartments cannot be performed. Thus, a perfectly leak-free system is essential, which could be ensured in the present study. For consistency, the CDP method was used throughout the study. Gas permeability coefficients were calculated by equation 14.

$$k_{gas} = -\frac{c\mu L}{AP_m\left(\frac{1}{V_1} + \frac{1}{V_2}\right)} \quad (\text{Eq.14})$$

Here A (m^2) and L (m) represent the cross-sectional area and the length of the sample, P_m (Pa) is the mean pressure of the upstream and downstream sides, c is the slope of the plot of $\ln(P_{up}(t) - P_{down}(t))$ versus time, μ is the gas viscosity ($\text{kg}\cdot\text{m}^{-1}\text{s}^{-1}$), V_1 and V_2 (m^3) are the volumes of the upstream and downstream compartments, respectively. Details of the derivation of the formulas are described in Brace et al. (1968) and Bourbie and Walls (1982).

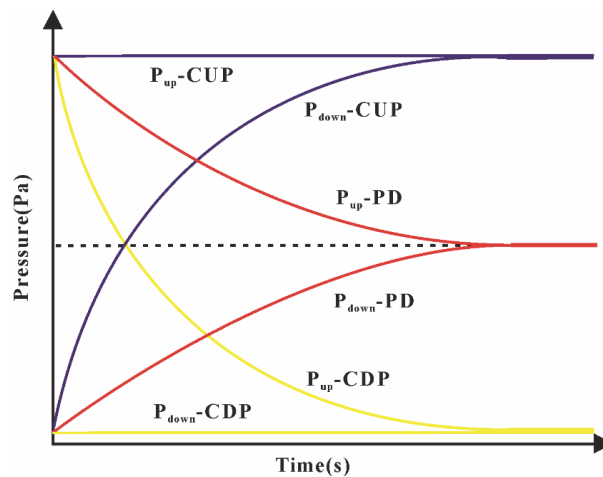


Fig 2.6 Sketch of the pressure decay curves of the conventional pulse decay (PD) method, the constant downstream pressure (CDP) method and the constant upstream pressure (CUP) method.

The samples were first loaded to 25 MPa for one week to ensure that they were fully re-compacted, and then they were unloaded to 5 MPa. Thus, permeability coefficients were not determined during the first loading/unloading paths, as these are known to be affected by damages induced by sample excavation and preparation. The measurements were subsequently conducted at different confining pressures by loading the confining pressure stepwise from 5 MPa to 20 MPa and unloading it back to 5 MPa. Each confining pressure level was held for at least five days for stress stabilization.

2.4 Results

2.4.1 XRD analysis

The results of the quantitative XRD analysis of the offcut material from the sample cube are listed in Table 2.1.

Table 2.1 XRD result of the Cobourg limestone.

Calcite (%)	Ankerite (%)	Illite/muscovite/I-S (%)	Quartz (%)	Kaolinite (%)	Pyrite (%)
79.05	9.31	5.12	4.81	1.22	0.48

2.4.2 Microstructure characteristics

All samples were scanned by micro-CT, either before and/or after petrophysical measurements (Fig 2.7). In sample B, discontinuities were observed with a mass of bright minerals accumulating around them (red circles in Fig 2.7a), as already reported by Selvadurai (2017). The dark discontinuities appeared to be widened after sample treatment for permeability and porosity measurements (Fig 2.7b). Although the other samples also show heterogeneities, no open micro-fractures were observed at the same resolution (voxel size of 44 μm) (Fig 2.7c-e).

BIB-SEM images confirm that the Cobourg limestone is very tight. Within the carbonate grains, angular pores (sizes up to 1 μm) were commonly observed (Fig 2.8a). However, these pores are mostly intraparticle (presumably remnants of fluid inclusions), isolated from each other, thus considered being irrelevant for fluid flow. Fig 2.8b shows large interparticle triangular pores (sizes up to 1 μm) of carbonate grains, which is rarely observed. Slit-shaped pores, up to several hundred nanometers in width, are distributed within the clay fraction, likely forming an interconnected pore network. In Fig 2.8c, a bunch of micro-fractures, as wide as several hundred nanometers, occur alongside pyrite grains and transect the clay matrix near the

discontinuities of sample B. These micro-fractures have mirrored edges and are therefore probably due to stress release, sample extraction and preparation.

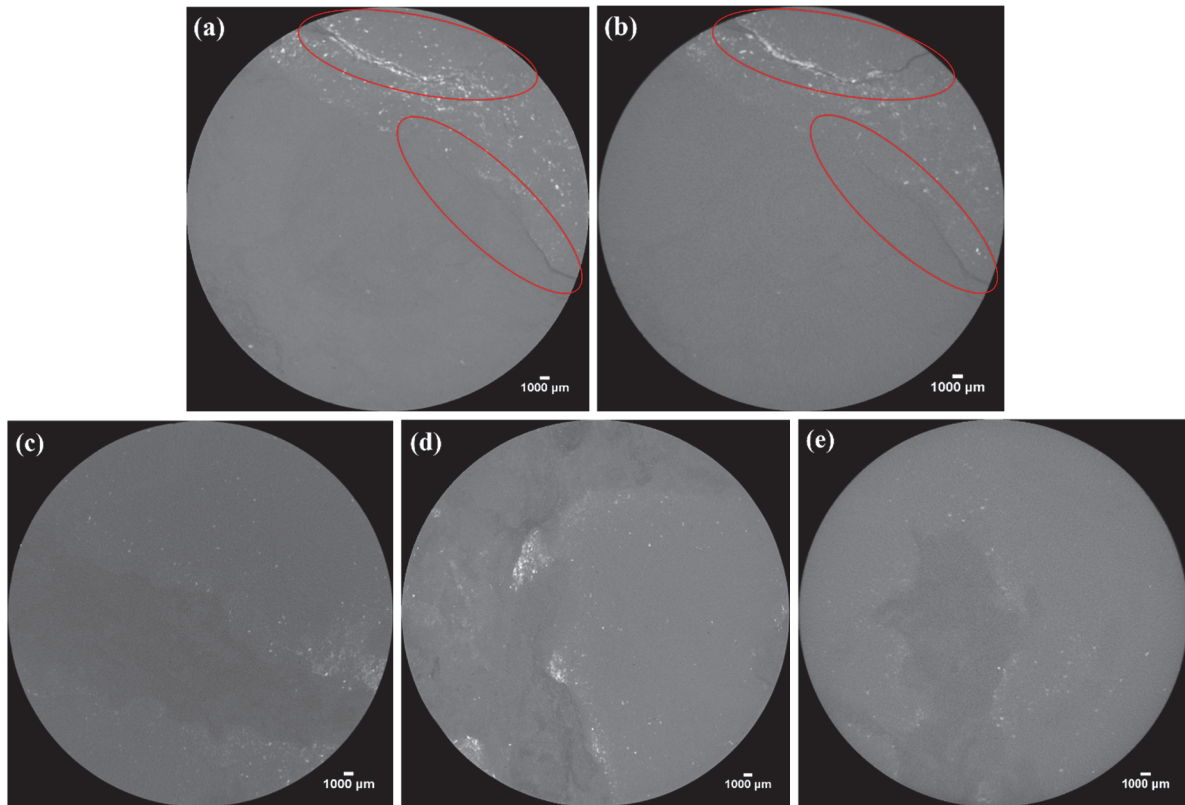
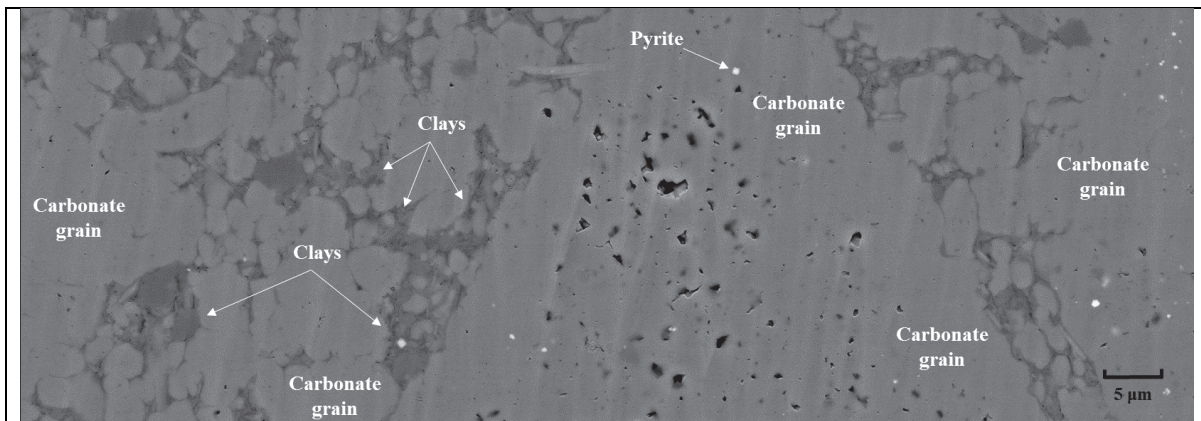
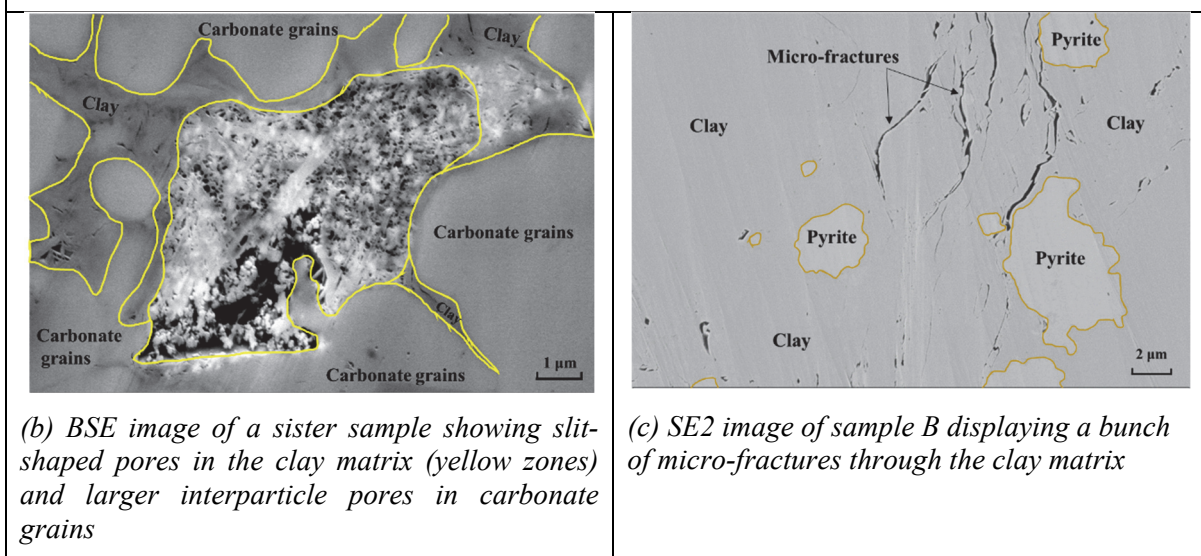


Fig 2.7 Micro-CT cross-section images of all samples. Top: sample B before (a) and after petrophysical experiments (b); bottom: (c) sample C after petrophysical measurement; (d) sample D before petrophysical experiments; (e) sample E after petrophysical measurement.

The discontinuities of sample B identified in the micro-CT scans are also clearly visible in the SEM micrographs (Fig 2.9a). The upper discontinuity zone, featuring a cluster of bright minerals, includes numerous small fractures with widths of several micrometers. The EDX element intensity maps show enrichment of Al, Si and S along the upper discontinuity zone (Fig 2.9b-d). High Al and Si intensities are interpreted as clay minerals and the high S intensity indicates pyrites. Clay minerals and pyrites tend to accumulate along the upper discontinuity zone. The enrichment of water-insoluble minerals indicate that massive pressure solution induced by chemical compaction occurred in the lithified limestone. Normally, pressure solution generates zigzag stylolites (Flügel, 2013), which can be opened during stress release. Another discontinuity zone, located at the middle-right part of the cross-section, also shows enrichment of Al and Si, though the intensities are not so pronounced. Fig 2.9e shows a SE2 image map of the fracture with an average aperture of 4.53 μm.



(a) BSE image of a sister sample showing angular intraparticle pores in carbonate grains, interparticle clay and pyrite grains



(b) BSE image of a sister sample showing slit-shaped pores in the clay matrix (yellow zones) and larger interparticle pores in carbonate grains

(c) SE2 image of sample B displaying a bunch of micro-fractures through the clay matrix near the discontinuities of sample B.

Fig 2.8 BIB-SEM images of the Cobourg limestone: (a) Angular pores with sizes up to half a micrometer form the intraparticle pores of carbonate grains and the clay matrix is distributed among carbonate grains; (b) Slit-shaped pores in the clay matrix among carbonate grains. Larger interparticle triangular pores shown in the middle of the image are uncommon; (c) Micro-fractures cut through the clay matrix near the discontinuities of sample B.

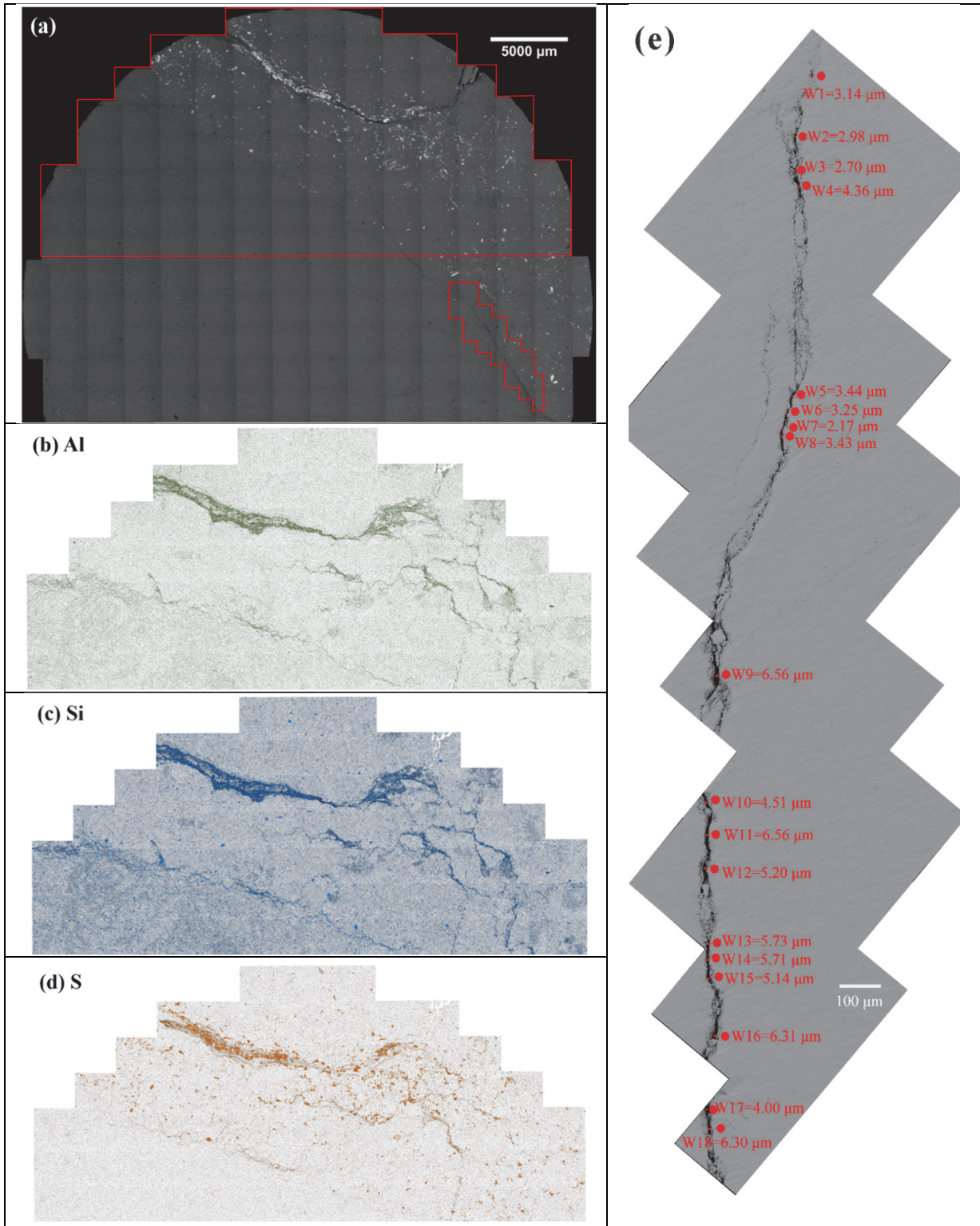


Fig 2.9 Fracture distribution on the cross-section area of sample B. (a) BSE map shows that two discontinuity zones are located on the upper and middle-right part of the cross-section area. The upper discontinuity is rich in bright minerals; (b-d) EDX maps exhibit the distribution of Al, Si and S on the upper part of the cross-section area (the upper red mark zone in Fig 2.9a); (e) SE2 image shows the fracture width distribution along the lower discontinuity zone (the lower red mark zone in Fig 2.9a). The average aperture of the fracture is 4.53 μm.

2.4.3 Porosity measurements

Porosities measured by He pycnometry and water immersion porosimetry under unconfined conditions are listed in Table 2.2, as well as those extrapolated from enhanced stress levels to ambient conditions. The helium porosities range from 0.98% to 2.51%. The porosity values measured by water immersion porosimetry are lower than those determined by He pycnometry. The extrapolated porosity values are 4-23% lower than those values determined by He pycnometry under ambient conditions.

Table 2.2 Porosity values of samples under the unconfined condition.

Sample	B	C	D	E
Helium Porosity (%)	1.02	0.98	2.51	1.83
Water immersion porosity (%)	0.94	0.48	1.68	0.87
Extrapolated porosity at zero effective stress (%)	0.98	0.75	2.14	1.41

Porosity measurements under different effective stresses were conducted on all the samples by helium expansion. As shown in Fig 2.10, porosity is decreasing by 8-13% with the increasing effective stress from 4 MPa to 19 MPa. A pronounced hysteresis between the second loading and unloading paths is not shown.

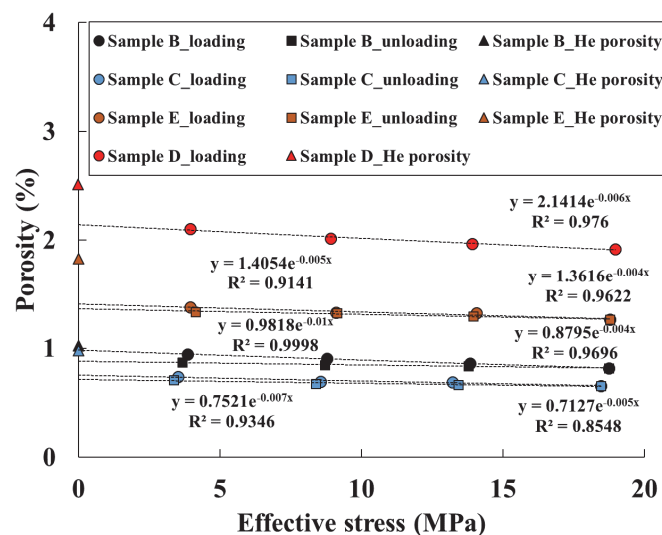


Fig 2.10 Relationship between effective stress and porosity in loading-unloading cycle. The circle symbols represent the porosity values in the loading path, while the square symbols denote the porosity values in the unloading path. Triangle symbols represent the porosity values determined by He pycnometry under ambient conditions. The error bars are not visible at this scale.

Table 2.3 Klinkenberg-corrected permeability coefficients (m^2) of Cobourg limestone samples as a function of confining pressure in the second loading-unloading cycle.

Confining pressure (MPa)	Sample B	Sample C	Sample D	Sample E
5	1.45×10^{-17}	4.64×10^{-20}	2.29×10^{-19}	1.17×10^{-19}
10	9.46×10^{-18}	2.69×10^{-20}	1.81×10^{-19}	8.43×10^{-20}
15	7.42×10^{-18}	2.30×10^{-20}	1.41×10^{-19}	7.23×10^{-20}
20	6.19×10^{-18}	1.95×10^{-20}	1.18×10^{-19}	3.84×10^{-20}
15	6.81×10^{-18}	2.03×10^{-20}	-	3.86×10^{-20}
10	8.27×10^{-18}	2.19×10^{-20}	-	4.68×10^{-20}
5	1.30×10^{-17}	3.15×10^{-20}	-	9.83×10^{-20}
Extrapolated permeability	1.79×10^{-17}	5.21×10^{-20}	2.74×10^{-19}	1.71×10^{-19}

2.4.4 Permeability measurements with helium

Permeability measurements using the CDP method were conducted on samples B, C and E during both loading and unloading cycles (Table 2.3). Unfortunately, the unloading cycle of sample D was affected by accidental water influx through a damaged sealing system during the first unloading step. Permeability coefficients significantly dropped to $8.66 \times 10^{-20} m^2$. After de-installation, water saturation had increased to 5.87%. The Klinkenberg plots of the apparent permeability coefficients of the four samples measured along the loading paths are shown in Fig 2.11. The Klinkenberg-corrected permeability coefficients of the four samples at an initial confining pressure of 5 MPa vary between 5×10^{-20} and $1 \times 10^{-17} m^2$. The Klinkenberg-corrected permeability of the fractured sample B at 5 MPa confining pressure is about 300 times higher than that of sample C. When the confining pressure was increased from 5 MPa to 20 MPa, the Klinkenberg-corrected permeability of sample B decreased from 1.45×10^{-17} to $6.19 \times 10^{-18} m^2$, that of sample C from 4.64×10^{-20} to $1.95 \times 10^{-20} m^2$, that of sample D from 2.29×10^{-19} to $1.18 \times 10^{-19} m^2$ and that of sample E from 1.17×10^{-19} to $3.84 \times 10^{-20} m^2$. The extrapolated permeability values at zero effective stress are additionally listed in Table 2.3. The relationship between Klinkenberg-corrected permeability and effective stress can be fitted by both power and exponential law (Eq.1 and Eq.2) for both loading and unloading paths (Fig 2.12). The stress sensitivity coefficients of the loading path are higher than those of the unloading path, ranging in the order of $10^{-2} MPa^{-1}$ (exponential law) and 10^{-1} (power law).

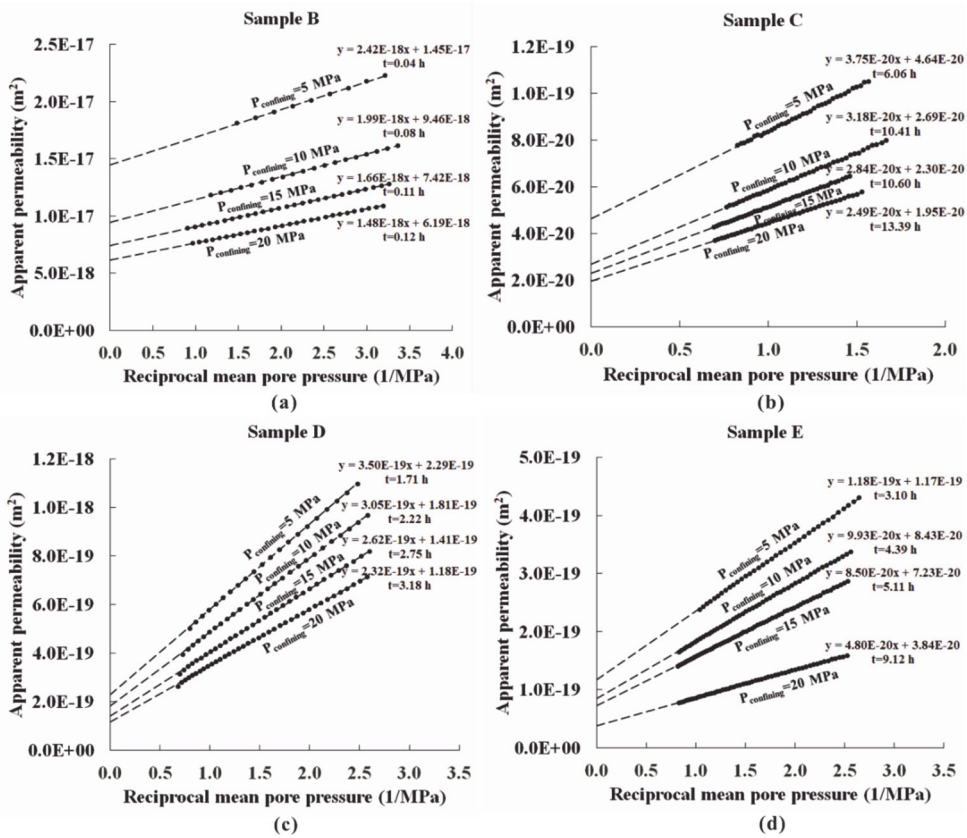


Fig 2.11 Klinkenberg plots of permeability tests using the CDP method on Cobourg limestone samples at different confining pressures (t denotes the duration of the measurement).

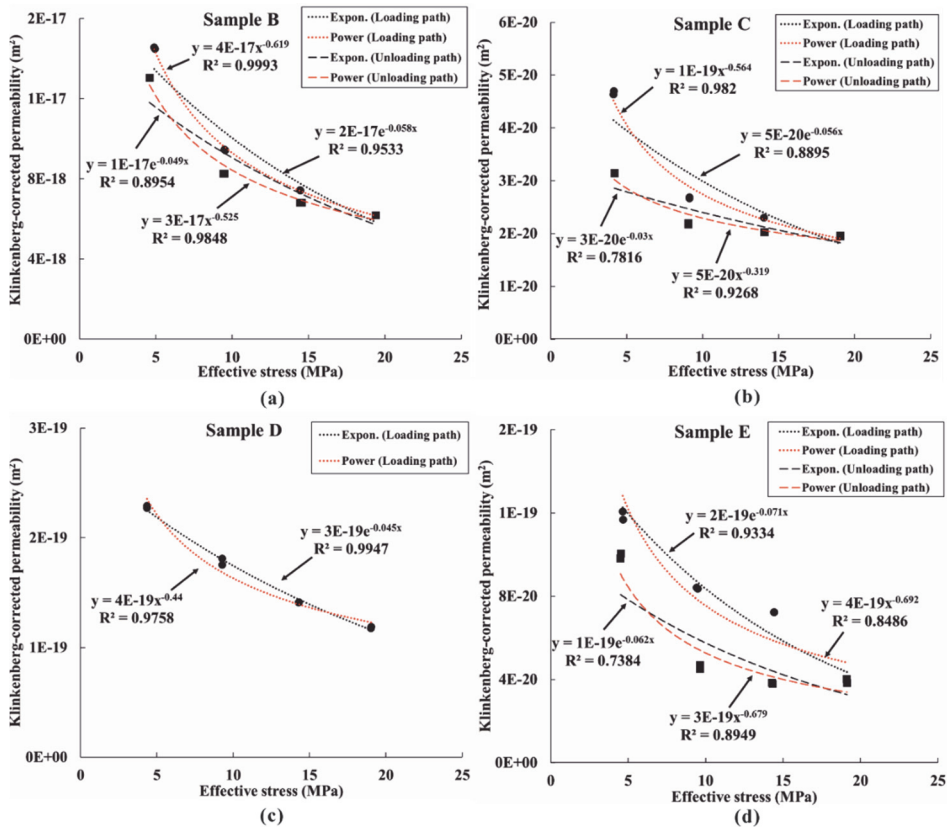


Fig 2.12 Relationship between Klinkenberg-corrected permeability coefficients and effective stress.

2.5 Discussion

2.5.1 Comparison of two porosity measurement methods

It is demonstrated that porosity values determined by helium pycnometry (HP) are larger than those from water immersion porosimetry (WIP). In Fig 2.13, bulk densities, grain densities and porosities determined by the different approaches are shown, including error bars representing the maximum systematic error, which considers the accuracy of the different experimental instruments (balance uncertainty $\delta m = 0.1\text{mg}$, pressure transducers $\delta p = 0.05\%FS = 5 \times 10^{-4}\text{MPa}$). In those cases where no error bars are shown, the error bar is smaller than the symbol. Fig 2.13a shows that the caliper-determined bulk densities are lower than those determined from WIP, likely as caliper measurements ignore surface roughness and tend to overestimate bulk volume (Rutter et al., 2017). The bulk volume determined from WIP is strictly independent of the surface roughness, “non-connected” pore space or imperfect saturation as long as the saturation level does not change during the procedure, i.e. weighing the water-saturated sample in water and at ambient conditions. For the latter measurement, it is important to remove the excess water from the sample surface. Generally, bulk volume determination could also be performed on dry samples if the immersion fluid would not penetrate the pore space (sealed sample). Therefore, we can consider the bulk volume determined from WIP to be closer to reality.

The grain densities from HP are generally higher than those from WIP (Fig 2.13b), which likely originates from He reaching a larger percentage of the accessible pore volume. Consequently, the HP-derived porosity is larger (Fig 2.13c). The fact that water had restricted access to the pore space could be explained by some remaining gas trapped within the pore space, which could not be displaced from dead-end pores (Fig 2.8a). It has indeed been observed, that even after periodic high pressure cycling for 3 days, still some gas bubbles came out of the samples. Therefore, the actual pore volumes (porosity) might be underestimated by WIP. Using the WIP bulk volume and HP grain volume, porosities of all samples are below 2% (Fig 2.13c).

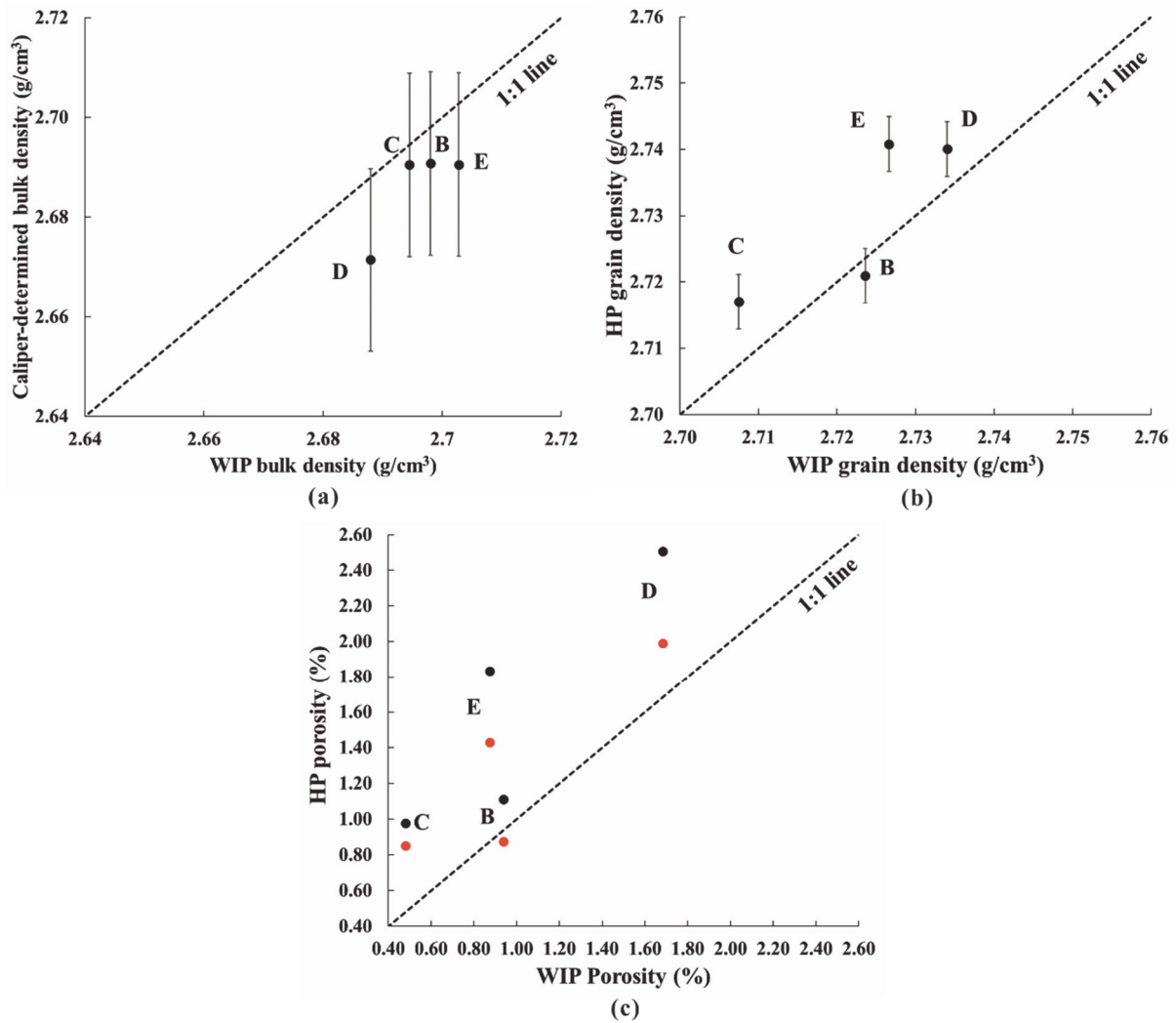


Fig 2.13 (a) Comparison of bulk densities of Cobourg limestone samples determined by caliper and water immersion porosimetry (WIP); (b) Comparison of grain densities measured by HP and WIP; (c) Comparison of porosities (V_{pore}/V_{bulk}) measured by HP and WIP. HP porosities were calculated twice, using V_{bulk} from caliper measurements (black dots) and from water immersion experiments (red dots).

2.5.2 Stress sensitivity of porosity and permeability

Stress-induced porosity and permeability changes are documented in literature for different rock types (Tables 2.4 and 2.5). Permeability consistently shows a larger stress sensitivity, which is due to the fact that permeability is strongly dependent on interconnecting restrictions, i.e. pore necks (Dong et al., 2010; Chalmers et al., 2012; Teklu et al., 2016; Fink et al., 2017). In this study, the exponential stress sensitivity coefficients for porosity and permeability range from 3.9×10^{-3} to $9.8 \times 10^{-3} \text{ MPa}^{-1}$ and 3.0×10^{-2} to $7.1 \times 10^{-2} \text{ MPa}^{-1}$, respectively. In both cases, the upper boundaries are representative of the loading path and the lower boundaries correspond to the unloading path.

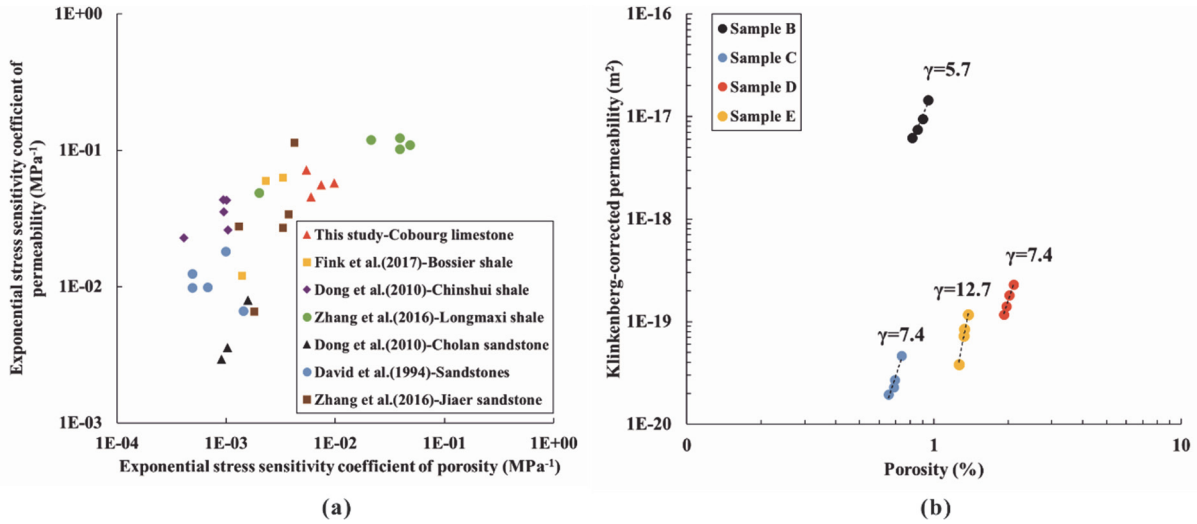


Fig 2.14 (a) Relationship between exponential stress sensitivity coefficients of porosity and exponential stress sensitivity coefficients of permeability for different lithologies; (b) Relationship between Klinkenberg-corrected permeability and porosity for Cobourg limestones (the slope of γ represents the porosity sensitivity exponent).

Table 2.4 and 2.5 summarize stress sensitivity coefficients published in the literature for different rock types. For sandstones, limestones, shales and mudstones, the stress sensitivity coefficients of permeability mainly range from 0.001 to 0.1 MPa⁻¹. A general positive relationship exists between stress sensitivity coefficients of porosity and stress sensitivity coefficients of permeability (Fig 2.14a). The higher the stress sensitivity of porosity, the larger the proportion of interconnected pores that can be compressed. This leads inevitably to a higher stress sensitivity of permeability. By plotting the absolute values of Klinkenberg-corrected permeability coefficients as a function of porosity (Fig 2.14b), a porosity sensitivity exponent γ can be determined:

$$k = k_0(\phi/\phi_0)^\gamma \quad (\text{Eq.15})$$

with k_0 (m²) and ϕ_0 (%) being the permeability and porosity at ambient conditions.

Table 2.4 Summary of stress sensitivity coefficients of permeability of sedimentary rocks.

Source	Sample	Description	Gas/water	Confining pressure (MPa)	Effective stress (MPa)	Stress sensitivity coefficient α or p			
						Exponential law: $k=k_0 \exp(-\alpha P_e)$		Power law: $k=k_0 P_e^{-p}$	
						Loading (MPa ⁻¹)	Unloading (MPa ⁻¹)	Loading	Unloading
This study	B	Calcite rich	Helium	5-20	-	5.8×10^{-2}	4.9×10^{-2}	0.6	0.5
	C	Calcite rich	Helium	5-20	-	5.6×10^{-2}	3.0×10^{-2}	0.56	0.32
	D	Calcite rich	Helium	5-20	-	4.5×10^{-2}	-	0.44	-
	E	Calcite rich	Helium	5-20	-	7.1×10^{-2}	6.2×10^{-2}	0.69	0.68
Wang et al. (2018)	Purbeck limestone	Calcite rich	Water	6-18	-	3.6×10^{-3}	-	-	-
	Indiana limestone	Calcite rich	Water	3-15	-	3.2×10^{-3}	-	-	-
	Thala limestone	Calcite rich	Water	7-15	-	1.2×10^{-3}	-	-	-
	Leitha limestone	Calcite rich	Water	7-15	-	1.1×10^{-3}	-	-	-
Ghabezloo et al. (2009)	Oolitic limestone	Calcite rich	Water	3-12	-	17.8×10^{-2}	-	0.6	-
Fink et al. (2017)	Bossier shale	Clay rich	Helium	10-40	-	-	1.2×10^{-2} - 6.3×10^{-2}	-	-
Ghanizadeh et al. (2014)	Scandinavian Alum shale	Clay rich	Helium	5-30	-	7×10^{-3} - 7×10^{-2}	-	-	-
McKernan et al. (2014)	Whitby Mudstone	Quartz and mica rich	Argon	-	10-70	2.9×10^{-2} - 3.4×10^{-2}	-	-	-
Chalmers et al. (2012)	Evie shale	Carbonate rich	Methane	-	13.8-41.4	7×10^{-6} - 1×10^{-3}	-	-	-
	Muskwa shale	Quartz rich	Methane	-	13.8-41.4	2×10^{-4} - 9×10^{-4}	-	-	-
	Otter Park shale	Carbonate and quartz rich	Methane	-	13.8-41.4	8×10^{-4}	-	-	-
	Besa River shale	Quartz rich	Methane	-	13.8-41.4	6×10^{-5} - 4×10^{-4}	-	-	-
Dong et al. (2010)	Cholan sandstone	Quartz rich	Nitrogen	-	3-120	2.9×10^{-3} - 8.0×10^{-3}	1.4×10^{-3} - 2.8×10^{-3}	0.1-0.3	0.06-0.1
	Chinshui shale	silt-shale	Nitrogen	-	3-120	2×10^{-2} - 5.2×10^{-2}	6.5×10^{-3} - 2.3×10^{-2}	0.7-2.1	0.5-1.0
David et al. (1994)	Adamswiller sandstone	Quartz rich	Water	-	80.5-151	1.2×10^{-2}	-	1.0	-
	Fontainebleau sandstone	Quartz rich	Water	-	80.5-151	1.0×10^{-2}	-	1.0	-
	Berea sandstone	Quartz rich	Water	-	80.5-151	1.0×10^{-2}	-	1.2	-
	Rothbach sandstone	Quartz rich	Water	-	80.5-151	1.8×10^{-2}	-	2.0	-
	Boise sandstone	Felspar and quartz rich	Water	-	80.5-151	6.6×10^{-3}	-	0.1	-
Morrow et al. (1984)	Illite	-	Water	5-200	-	1.8×10^{-2}	-	1.6	0.7
	Montmorillonite	-	Water	5-200	-	1.5×10^{-2}	-	1.4	0.9
	Kaolinite	-	Water	5-200	-	1.9×10^{-2}	-	1.8	0.7

Table 2.5 Summary of stress sensitivity coefficients of porosity of sedimentary rocks.

Source	Sample	Description	Confining pressure (MPa)	Effective stress (MPa)	Stress sensitivity coefficient β or q			
					Exponential law: $\phi = \phi_0 \exp(-\beta P_e)$		Power law: $\phi = \phi_0 P_e^{-q}$	
					Loading (MPa ⁻¹)	Unloading (MPa ⁻¹)	Loading	Unloading
This study	B	Calcite rich	5-20	-	9.8×10^{-3}	3.9×10^{-3}	8.8×10^{-2}	3.6×10^{-2}
	C	Calcite rich	5-20	-	7.4×10^{-3}	5.1×10^{-3}	6.6×10^{-2}	4.8×10^{-2}
	D	Calcite rich	5-20	-	6.0×10^{-3}	-	5.8×10^{-2}	-
	E	Calcite rich	5-20	-	5.4×10^{-3}	3.9×10^{-3}	5.0×10^{-2}	3.5×10^{-2}
Fink et al. (2017)	Bossier shale	Clay rich	10-40	-	-	1.4×10^{-3} - 3.3×10^{-3}	-	-
Dong et al. (2010)	Cholan sandstone	Quartz rich	-	3-120	0.9×10^{-3} - 1.6×10^{-3}	0.7×10^{-3} - 1.2×10^{-3}	3.7×10^{-2} - 5.6×10^{-2}	2.4×10^{-2} - 4.0×10^{-2}
	Chinshui shale	silt-shale	-	3-120	0.4×10^{-3} - 1.3×10^{-3}	0.1×10^{-3} - 0.8×10^{-3}	1.4×10^{-2} - 4.6×10^{-2}	0.6×10^{-2} - 3.0×10^{-2}
David et al. (1994)	Adamswiller sandstone	Quartz rich	-	80.5-151	4.9×10^{-4}	-	-	-
	Fontainebleau sandstone	Quartz rich	-	80.5-151	4.9×10^{-4}	-	-	-
	Berea sandstone	Quartz rich	-	80.5-151	6.7×10^{-4}	-	-	-
	Rothbach sandstone	Quartz rich	-	80.5-151	9.9×10^{-4}	-	-	-
	Boise sandstone	Felspar and quartz rich	-	80.5-151	1.4×10^{-3}	-	-	-
Zhang et al. (2016)	Jiaer sanstone	-	-	-	1.3×10^{-3} - 4.2×10^{-3}	-	-	-
	Longmaxi shale	-	-	-	2.0×10^{-3} - 48×10^{-3}	-	-	-

Table 2.6 Porosity sensitivity exponents of different pore models (modified after Zhang et al. 2016).

Pore model	Pore structure characteristics	γ value	Aspect ratio ($\epsilon = b/a$)
Circular pore	Cylindrical tubes	$\gamma = 2$	$\epsilon = 1$ ($a=b$)
Elliptical pore	Elliptical tubes	$2 < \gamma < 3$	$\epsilon < 1$ ($a > b$)
Sheet fracture	Fractures with parallel plates	$\gamma = 3$	$\epsilon \ll 1$ ($a \gg b$)
Dual-porosity	Type I: matrix pore radius close to the fracture width	$2 < \gamma < 3$	
	Type II: high fracture frequency; fracture width much larger than the matrix pore radius	$\gamma > 3$	
	Type III: low fracture frequency; fracture width much larger than the matrix pore radius	$\gamma \gg 3$	

In this study, γ ranges between 5.7 and 12.7 (Fig 2.14b), which is lower than the γ values of 8.1-27.4 determined by Fink et al. (2017) for Bossier shale and the γ values of 4.6-25.4

determined by David et al. (1994) for sandstones. Zhang et al. (2016) theoretically derived porosity sensitivity exponents for different pore geometries: circular pores, elliptical pores, sheet fractures and dual-porosity systems (Table 2.6). They defined the “aspect ratio” ε as the ratio between the semi-minor axis (b) and the semi-major axis (a) in an elliptical pore model. In the first three simple pore models, the porosity sensitivity exponent increases with decreasing aspect ratio and the maximum γ value is 3. The type II and type III of dual-porosity models feature high γ values and fracture widths much larger than matrix pore radii. The high γ values of Cobourg limestone are in accordance with the type II and type III of dual-porosity models in which fluid flow is dominantly occurring within the fracture system.

Ghanizadeh et al. (2015) and Xu et al. (2018a) observed that stress sensitivity coefficients of permeability of clay-rich sandstones or shales are much higher than those of clay-lean samples. Compared to the bulk modulus of calcite (73.3 GPa), dolomite (94.9 GPa) and quartz (37.8 GPa), clay minerals indeed have lower bulk moduli (5.8-11.0 GPa) and are thus easier to deform (Bass, 1995; Vanorio et al., 2003). Apart from mineralogy, the inherent arrangement of minerals, clasts or shell fragments, homogeneity and bedding orientation are also rather influential. Chalmers et al. (2012) and Gensterblum et al. (2015) reported that the permeability coefficients measured parallel to bedding are more stress-sensitive than those measured perpendicular to bedding. As clasts, clay particles or shell fragments tend to align along the lamina or bedding, intergranular pores are abundant (Kwon et al., 2004; Chalmers et al., 2012; Ghanizadeh et al., 2015). Besides, natural and artificial fractures also prefer to form along the bedding plane (Yang and Aplin, 2007; Vogler et al., 2017). Once pressurized, these interconnected “highways” are readily closed, which will significantly increase the tortuosity and lead to a stronger stress sensitivity of permeability along the bedding. For the Cobourg limestone, no bedding planes can be observed macroscopically or detected in micro-CT scans. The interconnected slit-shaped pores and micro-fractures within the clay matrix might be responsible for the high stress sensitivity.

In our study, gas permeability was measured on the second loading and unloading paths. Even though the samples had already been compressed in the first loading and unloading cycle, a permeability hysteresis was observed (Fig 2.15). The permeability values determined on the unloading path correspond to 53.3-91.8% of the values determined on the loading path. In comparison to the other samples, the permeability drop of sample E during the loading cycle is less pronounced at 15 MPa, thereafter a fast permeability decrease is documented upon stress

increase to 20 MPa. This can either be related to (a) an overestimated permeability value at 15 MPa, (b) an underestimated coefficient at 20 MPa or (c) to the efficient compression of conducting pores/fissures above 15 MPa. However, the reason is not clear. Principally, an overestimation could result from insufficient stress equilibration at 15 MPa, even after 9 days. For this pressure step, the permeability coefficients measured during the following three days differed no more than 4% and did not show a decreasing trend. An underestimation could result from water influx (sealing damage), however, the porosity measured at 20 MPa did not show a deviation and no mass change was recorded after de-installation of the sample. It is reasonable to assume that the collapse of certain pores is only achieved at higher pressures. As the permeability of the Cobourg limestone is controlled by a few open stylolites, the closure of these structures will lead to a significant permeability decrease. The amplitude of hysteresis measured for porosity is not significant (Fig 2.10), with porosity values on the unloading path of about 92.1%-99.8% of those on the loading path. Letendre (2011) also reported hysteresis effects for the Cobourg limestone. Permeability values on the unloading path (20-5 MPa) correspond to 71.3-85.0% of the values on the loading path (5-20 MPa). Morrow (1984) attributed this hysteresis effect to the irreversible grain compaction of fault gouges and pure clays. For the Wilcox shale studied by Kwon et al. (2004), permeability values at zero effective stress, extrapolated from data of the first unloading path, is about 100 times smaller than those of the first loading path. Kilmer et al. (1987) and Ghanizadeh et al. (2014) related the hysteresis behavior of permeability to the stress history. Because of long-term stress relaxation effects, permeability is more sensitive to previous stress history in the first loading curve. Raven and Gale (1985) observed the magnitude of flow-rate hysteresis decreases with successive loading cycles for five fractured granite samples with diameters ranging from 0.1 to 0.3 m, following a decreasing magnitude of permanent fracture deformation. Considering that the Cobourg limestone specimens were sampled at a shallow depth in a quarry, the blast excavation, transportation and preparation will inevitably introduce some disturbance (Fig 2.8c). Unlike natural micro-fractures exposed to weathering or shearing, the artificial micro-fractures possess larger scale asperities (Vogler et al., 2017). The “surviving” asperities during the first loading path could be crushed in the second loading path (also known as creep), which might explain the permeability hysteresis.

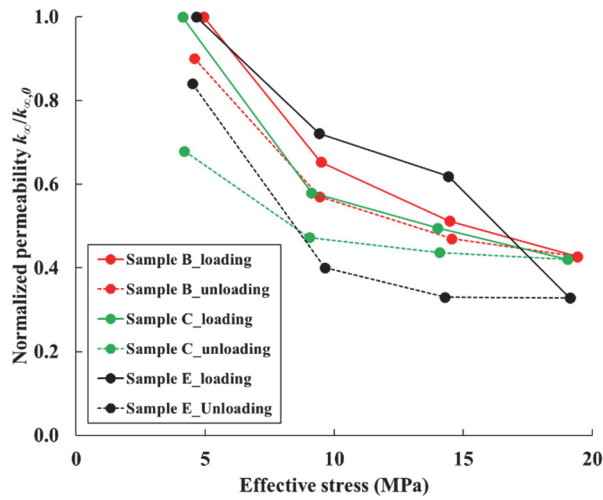


Fig 2.15 Intrinsic permeability coefficients normalized to intrinsic permeability at initial effective stress ($k_c/k_{c,0}$) versus effective stress for both loading (solid lines) and unloading paths (dashed lines).

2.5.3 Pore structure evolution with effective stress

It has been reported by several authors that the slip factor increases with increasing effective stress, indicating a decrease in average effective pore size (Letham and Bustin, 2016; Fink et al., 2017). This same trend is also obtained in this study (Fig 2.16). Table 2.7 summarizes the mean effective cylindrical pore diameters and mean effective slit widths of the present sample set, which are calculated according to equations 6 and 7. Sample B with the highest permeability has the highest mean effective cylindrical pore diameter and slit width. The effective cylindrical pore diameters of the other samples are smaller than 100 nm at different confining pressures.

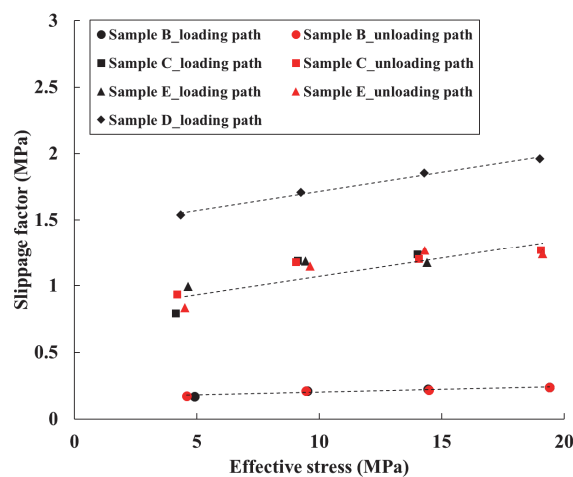


Fig 2.16 Slippage factors at different effective stresses for samples B, C, D and E in the loading and unloading paths. Black symbols represent the slippage factors in the loading path and red symbols denote the slippage factors in the unloading path.

The extrapolated slit width of sample B at zero confining pressure is 1141 nm. According to the SEM images of the lower discontinuity zone of sample B (Fig 2.9e), the average fracture aperture of 4.53 μm is larger but still at the same order of magnitude. The larger average fracture aperture derived from BIB-SEM analyses can be explained by the sampling bias as the most fractured section visible in the micro-CT was selected. Moreover, it is likely that the fractures are further opened during cyclic loading processes and sample section preparation for BIB-SEM investigation. Additionally, fractures with widths below the resolution of SEM images were not accounted for. However, these tiny seepage channels slightly contribute to the permeability compared to the large fractures identified in the micro-CT. At different confining pressures, calculated slit widths according to Jones's fracture model (Eq.8) are slightly larger than those derived from the slip flow approach (Eq.7) (Fig 2.17). Jones's fracture model is based on Snow's parallel plate model without considering matrix pores' contribution to permeability, while it is the average effective pore size that is obtained from the slippage factor for the slip flow approach. However, both two models neglect the roughness of fracture surfaces and the varying tortuosity at different effective stresses, not reflecting the complexity of the pore network.

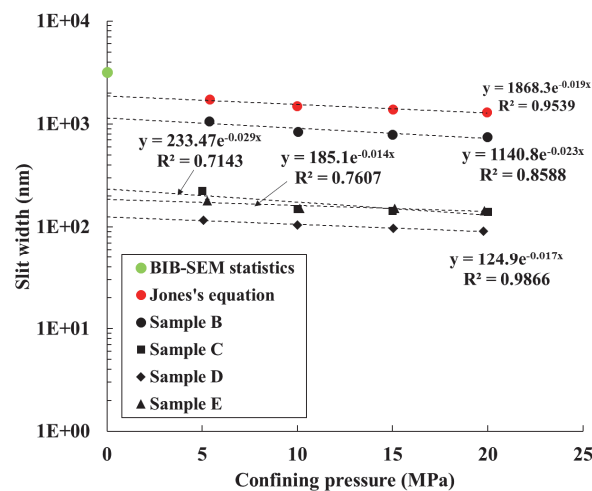


Fig 2.17 The mean effective slit width at different confining pressures (the black symbols represent the slit widths derived from slippage factors at different confining pressures and different symbol shapes denote different samples, the red symbols represent the slit width of sample B calculated by equation 8 with the measured intrinsic permeability, the green dot denotes the slit width of sample B by BIB-SEM statistics at unconfined conditions).

Regarding to the big differences of calculated slit widths (Fig 2.17) and measured permeability coefficients (Table 2.3) between sample B and the other samples, we can infer that the fluid

flow in sample B is dominated by the opening of stylolites. For the other samples that do not show any of these discontinuities at this scale (Fig 2.7), it is likely that the fluid flow is controlled by the distribution of porous clay matrix in between carbonate grains, since the pores typically show sizes (Fig 2.8b-c) close to the extrapolated mean effective slit width at zero confining pressure (Table 2.7). This hypothesis will be further investigated in an ongoing study including detailed FIB-SEM tomography of the porous network in the clay matrix. Due to the occurrence of stylolites in this limestone sequence and their conduit role for fluid flow, the matrix permeability is not considered as a critical factor for the sealing efficiency of DGR.

Table 2.7 The mean effective pore sizes of four samples at different confining pressures.

Confining pressure (MPa)	Sample B		Sample C		Sample D		Sample E	
	Cylindrical pore diameter (nm)	Slit width (nm)	Cylindrical pore diameter (nm)	Slit width (nm)	Cylindrical pore diameter (nm)	Slit width (nm)	Cylindrical pore diameter (nm)	Slit width (nm)
	5	289	1068	61	226	31	116	49
10	228	845	41	150	28	105	41	151
15	214	793	39	144	26	96	41	152
20	203	751	38	141	25	91	39	144
Extrapolated to 0 MPa	308	1141	63	233	34	125	50	185
BIB-SEM		4527						
Jones's equation		1868						

2.6 Conclusions

A comprehensive laboratory study was conducted on four Cobourg limestone samples, including petrophysical measurements of porosity and permeability under confining pressures of 5 to 20 MPa and microstructural analyses (micro-CT and BIB-SEM). Comparison of the different techniques leads to the following conclusions:

(1) Helium pycnometry (HP) yields generally larger porosity values than water immersion porosity (WIP). This is mainly attributed to incomplete water saturation in WIP. The bulk volume determined by WIP is considered more accurate than caliper measurements and should therefore be preferred for porosity calculation. The calculated He porosities are all below 2%.

Porosity only slightly changes upon loading to 20 MPa (decrease by 8-13%).

(2) A permeability hysteresis is observed between the second loading and unloading path, which is attributed to the crushing of artificial fracture asperities preserved during the first loading path. Accordingly, the stress sensitivity coefficients on the loading path vary between samples, being higher than those on the unloading path. In general, stress sensitivities of permeability and porosity are positively correlated.

(3) The major discontinuities observed in the most permeable sample B (1×10^{-17} - 6×10^{-18} m²) are identified as open stylolites (about 5 μ m), enhancing the permeability significantly as compared to the other samples. Based on gas permeability data, slip flow theory and Jones's fracture model yield characteristic fracture widths of approximately 1 μ m and 2 μ m, respectively. The difference between observed and calculated apertures is attributed to a combination of sampling bias, sample handling and preparation artefacts, limited applicability of the models and varying pore structure at different stress states. BIB-SEM investigation and the high porosity sensitivity exponents infer that major transport pathways in samples C, D and E are the slit-shaped pores and micro-fractures distributed in the clay matrix.

3. MULTI-SCALE CHARACTERIZATION OF PETROPHYSICAL PROPERTIES OF THE COBOURG LIMESTONE- A POTENTIAL NUCLEAR WASTE HOST ROCK IN CANADA

Keywords: Cobourg limestone; BIB-SEM; FIB-SEM; Pore size distribution; Permeability; Simulation

ABSTRACT

The Middle Ordovician Cobourg limestone is proposed as a potential host rock of nuclear waste in Canada. Evaluation of its sealing capacity requires a full understanding of fluid transport processes, which is essentially based on comprehensive knowledge of the pore space at multi-scale. Due to its very heterogenous grain size distribution, variable mineralogy and low permeability, it is a challenge to identify the petrophysical features relevant for storage and flow. Here, a series of imaging techniques including X-ray micro computed tomography (micro-CT), broad ion beam – scanning electron microscopy (BIB-SEM) and focused ion beam (FIB) – SEM were applied on a selection of Cobourg limestone plugs and subsamples to characterize the pore morphology and pore structure of the specific zones, and the results were compared to various bulk measurements (X-ray diffraction, helium pycnometry and permeability measurements). Mineralogy analysis on BIB-SEM images indicates that the Cobourg limestone can be characterized as a tight rock dominated by calcite grains of variable sizes (μm - cm) surrounded by idiomorphic or subhedral minerals (quartz, dolomite and pyrite) and meshy clay minerals. Qualitative and quantitative pore analyses show that calcite and clay mineral phases contribute 36.2-85.9% and 13.7-54.6% to the total visible pore area, respectively. The clay pores are relatively small and close to each other, elongated in shape and

are interpreted as interparticle pores. On the contrary, the pores associated with calcite have a large pore size range and are distant from each other, equidimensional or elongated in shape and can mostly be considered as intraparticle pores. Different pore size distributions were identified for the two phases, which can be characterized by power law relationships between pore area and normalized pore frequency with different exponents (1.93-2.18 for calcite and 2.50-2.59 for clay). Based on this relationship, extrapolated porosities were compared to porosities obtained by helium pycnometry (HP).

3.1 Introduction

In the context of the disposal of high-level radioactive waste (HLW), a broad consensus has been reached on the necessity for suitable geological formations for the safe and permanent storage of radioactive waste worldwide (McKinley et al., 1992; Allan et al., 1997; IAEA, 2001; Loubergé et al., 2002). Depths between 250 and 1000 m are considered appropriate for underground mining repositories, while depths of up to 5 km are discussed for deep borehole disposal (Birkholzer et al., 2012; Apted and Ahn, 2017). Potential waste disposal sites are generally located in a stable geological environment (i.e. no volcanic/ seismic activity or limited uplift within 1 Ma) and contain lithological units of sufficient thickness and homogeneity, characterized by a low permeability/diffusivity as well as high self-sealing ability and radionuclide sorption capacity (Witherspoon and Bodvarsson, 2006; Apted and Ahn, 2017). For salt and argillaceous rocks (claystones or mudstones), hydraulic isolation is generally ensured by an impermeable or low permeable matrix (IAEA, 2001). Highly rigid rocks such as granites and limestones, which are particular suitable for underground construction, tend to deform brittely and therefore often contain a fracture network. For these rocks, long-term isolation must thus be ensured by installation of engineered barriers (containers, bentonite backfill) (Birkholzer et al., 2012).

The Middle Ordovician Cobourg limestone, also known as “Lindsay” limestone, is proposed as a potential host rock for deep disposal of low- and intermediate-level radioactive waste in Canada. Several investigations have been carried out so far to evaluate its mechanical properties (Hekimi et al., 2012; Nasserri et al., 2013; Selvadurai et al., 2017; Nguyen et al., 2018) as well as petrological and mineralogical characteristics (Lippitt, 1959; Haeri-Ardakani et al., 2013; Petts et al., 2017). Since the main transport mechanism of radionuclides is via groundwater, isolation of radionuclides depends on the groundwater flow rate or interstitial velocity, which is determined by the porosity, hydraulic conductivity (or permeability) and

hydraulic gradient. Porosities reported from mercury injection porosimetry (MIP), water immersion porosimetry (WIP) and helium pycnometry (HP) for the Cobourg limestone range from 0.48 to 3.03% (Vilks and Miller, 2007; Cavé et al., 2009; Hu et al., 2020b). Permeability coefficients determined with water as the permeating fluid at 5 MPa confining pressure range from 3.31×10^{-23} to 1.80×10^{-21} m² (Vilks and Miller, 2007; Letendre, 2011) and intrinsic gas permeabilities at the same confining pressure range from 3.15×10^{-20} to 1.45×10^{-17} m² (Hu et al., 2020b). According to Hu et al. (2020b), large variations in permeability coefficients can be attributed to the occurrence of fractures. Furthermore, microscopic and macroscopic heterogeneities in the Cobourg limestone could be the cause of variations in the permeability coefficients. Day et al. (2017) and Hu et al. (2020b) reported that the Cobourg limestone is mainly composed of a calcite phase and surrounded by a fine-grained clay mineral phase on the basis of SEM investigation. Selvadurai (2017) observed on a macroscopic scale that the Cobourg limestone is composed of a light grey nodular calcite-rich phase and an inter-nodular dark grey clay-rich phase. The distribution of the latter phase shows a distinct heterogeneity, which was confirmed by Selvadurai (2017) during the preparation of a large cylindrical sample (150 mm in diameter and 300 mm in length). Such a heterogeneous fabric presents a major challenge in obtaining representative elementary areas or volumes (REA or REV) for both imaging analyses and petrophysical investigations on the Cobourg limestone.

Conventional permeability measurements are typically performed on cylindrical samples in pseudo-triaxial flow cells. Microfractures that are artificially generated during preparation can thus be closed and the “in-situ” permeability of the sample plug can be determined with a liquid or gas as the permeating fluid. In the latter case, permeability coefficients must be corrected for the gas slippage effect (Klinkenberg, 1941). As the gas slippage effect is related to the mean free path of the utilized gas, the gas slippage factor can be utilized to determine the mean transport pore size of the porous medium (Klinkenberg, 1941; Letham and Bustin, 2016). It should be noted that this relation is based on theoretical assumptions for the kinetic diameter of the molecules and more importantly on a simple pore geometry (cylindrical or slit-shaped). Mercury injection porosimetry (MIP) and low-pressure nitrogen or carbon dioxide adsorption are widely used to characterize the pore structure of sedimentary rocks as well (Hildenbrand and Urai, 2003; Seemann et al., 2017). However, these characterizations are also based on simplified pore geometry assumptions. Therefore, the results lack direct information on the pore morphology and connectivity. Additionally, occurrences and distributions of pores could be linked to specific mineral phases, which cannot be investigated by fluid invasion techniques

as the measurements are typically performed on the bulk rock samples (Klaver et al., 2012; Curtis et al., 2012; Anovitz et al., 2015). Digital rock physics (DRP) has the potential to simulate petrophysical properties from 3D pore reconstructions though it is necessary that the simulations take place within a REV to generate permeability coefficients comparable to those of laboratory measurements on core samples (Blunt et al., 2013; Keller et al., 2013; Grathoff et al., 2016). X-ray micro computed tomography (micro-CT) can be used as a quantitative and non-destructive imaging technique to reconstruct the 3D microstructure from a cylindrical sample (Cnudde and Boone, 2013). In conventional rocks such as sandstones, X-ray micro-CT was successfully used to determine a REV and to generate a 3D pore network from which simulation results on permeabilities are in good agreement with experimental measurements (Mostaghimi et al., 2013; Andrä et al., 2013; Kelly et al., 2016; Saxena et al., 2017). However, the resolution limitation of X-ray micro-CT becomes apparent when imaging nanoporous geomaterials. With the development of imaging technology, scanning electron microscopy (SEM) is capable of providing high resolution images, to investigate the pore space down to several nanometers. Broad ion beam milling (BIB) complements the preceding method by enabling the preparation of millimeter-sized planar surfaces, thus providing a qualitative and quantitative approach for the characterization of the pore structure free of artifacts such as cracks or scratches on a relatively large area (several mm²) (Klaver et al., 2012; Klaver et al., 2015a; Philipp et al., 2017). However, the field of observation is two dimensional and hence no information on the three-dimensional pore space connectivity can be obtained. Alternatively, focused ion beam milling in combination with SEM (FIB-SEM) enables the possibility of serial sectioning and simultaneous imaging. A series of high-resolution SEM images can be generated with uniform spacing, enabling 3D reconstruction and visualization of the microstructure. However, the limited volume raises uncertainties about its application in quantitative analysis of heterogeneous nanoporous rocks (Curtis et al., 2012; Keller et al., 2013; Bultreys et al., 2015; Kelly et al., 2016).

Due to small pore sizes and distinct heterogeneity of the Cobourg limestone, determining a REV is challenging in terms of both mineralogy and pore space with current state-of-the-art techniques, and hence upscaling is difficult. Alternatively, selective analysis of pore morphologies and pore structures of specific zones can help to improve the understanding of potential fluid transport pathways. This study aims at a detailed characterization of the pore size distribution, pore morphology down to 10 nanometers by utilization of FIB- and BIB-SEM techniques to identify microstructures relevant for flow. Self-similar characteristics of pore size

distributions in calcite and clay mineral phases are identified and utilized for extrapolation to pores cannot be resolved by BIB-SEM, showing good comparability to bulk porosities by HP, if a representative mineralogy is present in the studied map. This is the first study integrating imaging techniques on the highly heterogeneous Cobourg limestone at multi-scale.

3.2 Samples

The Cobourg limestone we investigated originates from a depth of 70 m from the Saint Mary's cement quarry in Bowmanville, Ontario, Canada. The corresponding formation at the Bruce nuclear site (200 km away) is found at a depth of approximately 680m and is being investigated as a potential host rock for disposal of low- and intermediate-level nuclear waste (Selvadurai, 2017). A benchmark study involving 28 laboratories was initiated by the McGill University to study geomechanical and fluid transport properties of the Cobourg limestone (Davy et al., 2019).

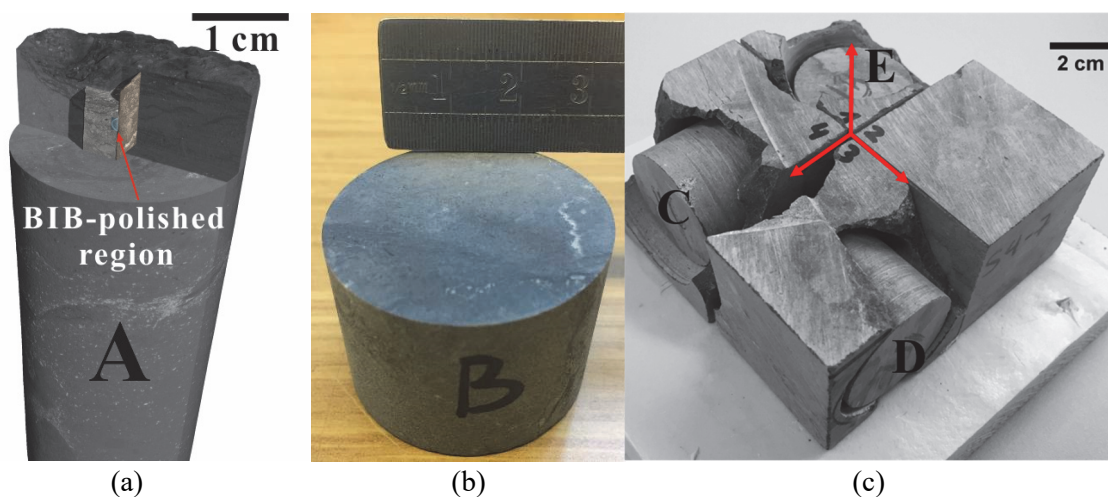


Fig 3.1 (a) Rendered X-ray micro-CT image of cylindrical sample A and the location of the BIB polished region (magnified in Fig 3.2a); (b) Cylindrical sample B with white strip on the top surface; (c) Cylindrical samples of C, D and E drilled in three mutually perpendicular directions as indicated by red arrows.

The sample utilized in this study can be characterized as a light grey nodular limestone, consisting of 79 wt.% of calcite, 9 wt.% of ankerite, 6 wt.% of clay minerals, 5 wt.% of quartz and less than 1 wt.% of pyrite (Hu et al., 2020b). Five Cobourg limestone plugs with two different sizes (4 plugs with 38 mm and 1 plug with 25 mm diameter) were drilled with water as the cooling agent. These samples were fully dried in the vacuum oven and then scanned by X-ray micro-CT. A micro core was retrieved from the 25 mm diameter core (Fig 3.1a) and used for high-resolution X-ray micro-CT and the subsequent BIB- and FIB-SEM imaging. Gas

permeability measurements were conducted on the four larger core plugs (samples B, C, D and E) and the results were published in Hu et al. (2020b) (Fig 3.1b-c). Porosities determined by helium pycnometry (HP) ranged from 0.98 to 2.51 %. For the intact samples C, D and E, extrapolated helium permeability coefficients at zero effective stress ranged from 5.21×10^{-20} to $2.74 \times 10^{-19} \text{ m}^2$. The corresponding coefficient of sample B was $1.79 \times 10^{-17} \text{ m}^2$, which is attributed to the existence of open stylolites (Hu et al., 2020b).

3.3 Imaging experiments and simulation

3.3.1 X-ray micro-CT

The X-ray micro-CT setup is generally composed of an X-ray source and a detector. In operating mode, a sample is placed between the two components and attenuates the intensity of X-ray radiating from the source. The attenuation is dependent on the sample density and the mean atomic number of constituent elements. The X-ray detector continuously records radiographic projection images under changing viewing angles when the sample is rotated over 360° . These projection images are then used for 3D volume reconstruction. The spatial resolution depends on the magnification and thus for a cone beam geometry on the position of the sample between the X-ray source and detector. Lower-resolution scans generally cover larger sample volumes and vice versa. The Cobourg limestone plugs were scanned on the HECTOR setup developed by the Center for X-ray Tomography at Ghent University (UGCT) and the TESCAN CoreTOM from TESCAN company. The X-ray micro-CT scanning was operated at 160 kV and a resolution of $40 \mu\text{m}$ for the large sample plugs (38 mm in diameter). The micro core was scanned at a high resolution of $8 \mu\text{m}$. Details of the setup and specific operation can be found in Masschaele et al. (2007) and Dierick et al. (2013).

3.3.2 BIB-SEM

A side of the extracted micro core was manually polished by utilization of a silicon-carbide paper (Fig 3.2a). In order to obtain a high-quality polished surface, a cross-section area of approximately 1 mm^2 was polished at a high angle in a JEOL SM-09010 BIB cross-section polisher at 6 kV acceleration voltage for 8 hours. The polished cross-section was then coated with tungsten, favorable for the subsequent imaging in a Zeiss Supra 55 SEM and energy-dispersive X-ray spectroscopy (EDX) analysis (Desbois et al., 2009; Klaver et al., 2012). The combination of backscattered electron (BSE) images and EDX maps was used in the mineral composition analysis. High-resolution secondary electron (SE2) images were utilized for the

analyses of pore morphology and pore size distribution.

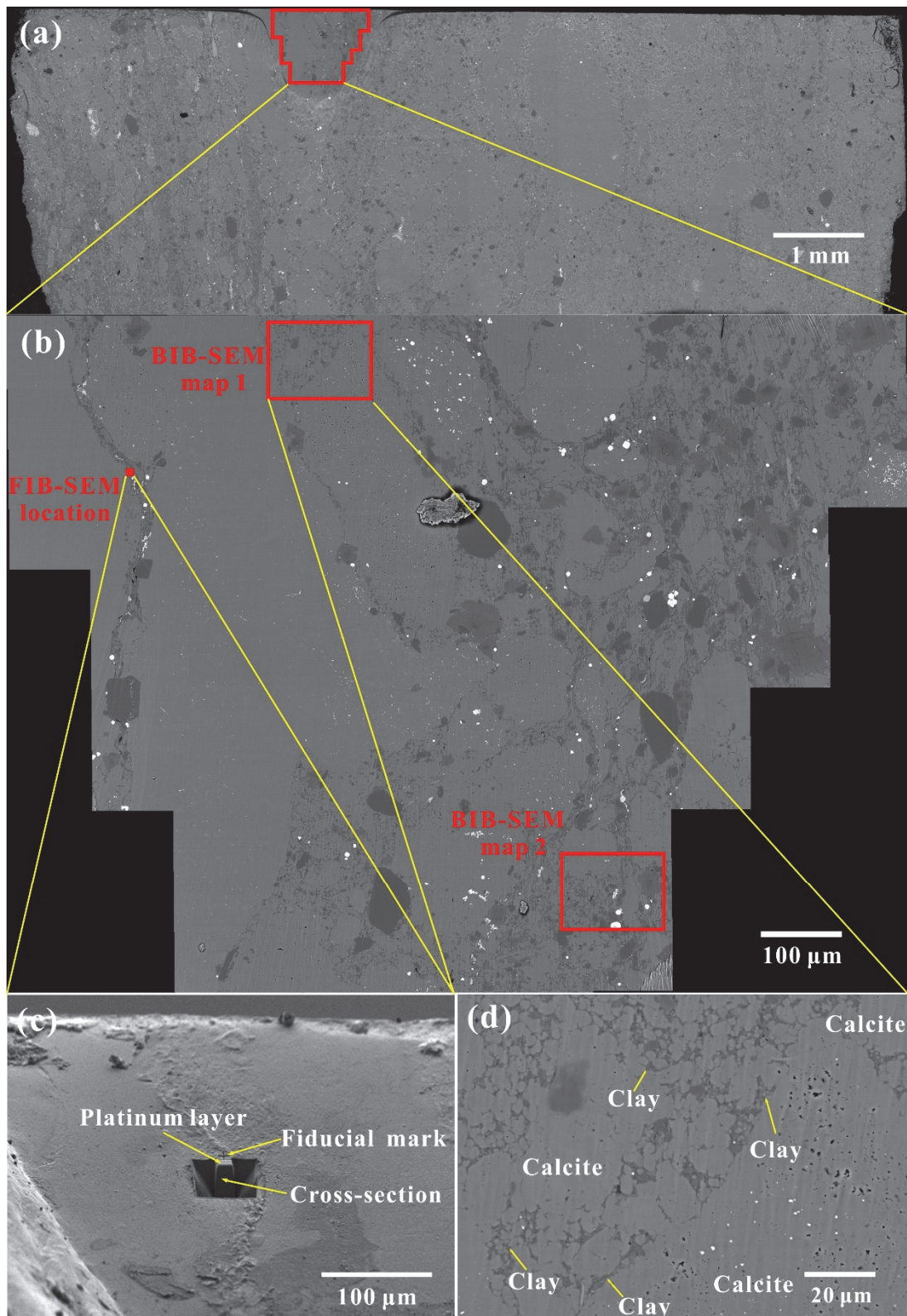


Fig 3.2 Overview of the studied section of sample A and the corresponding ROI of BIB- and FIB-SEM. (a) The cross-section of sample A; (b) The BIB-polished region: maps 1 and 2 are the ROI where both mineral composition and pore size distributions were analyzed quantitatively and the ROI of FIB-SEM is located on the upper left corner; (c) The ROI of FIB-SEM traversed by a strip rich in clay minerals;

(d) The BSE image of map 1.

As the Cobourg limestone is heterogenous (Fig 3.2b), only the region of interest (ROI) (maps 1 and 2) was analyzed quantitatively for mineral composition and pore size distribution.

3.3.3 FIB-SEM

The ROI for FIB-SEM is traversed by a strip rich in clay minerals (Fig 3.2b). The ROI was firstly covered with a layer of platinum to decrease the occurrence probability of curtaining artifacts (Curtis et al., 2012). In the working mode of the TESCAN AMBER FIB-SEM, the focused ion beam and electron beam intersect on the sample surface at the angle of 52°. A portion of limestone in this region was then removed by a Ga⁺ ion beam at accelerating voltage of 30 kV and high beam current of 20 nA, creating a prominence in a trench (Fig 3.2c). Thus, the first cross-sectioning can be implemented by the ion beam on an exposed wall of the prominence and 10 nm thickness of the wall was removed to expose a fresh and polished limestone surface. For gentle slicing of the target volume, Ga⁺ ion beam at accelerating voltage of 30 kV and low beam current of 250 pA was used to minimize milling artifacts. Subsequently, SEM imaging in BSE mode was conducted at a high resolution of 1107×1749 pixels. In this way, the ion beam cooperated with the electron beam in a repetitive milling and imaging process until the target volume was imaged. The fiducial mark was given for reference and registration of the FIB experiment (Fig 3.2c). A total number of 498 cross-sectional images with a voxel size of 10 nm were acquired for the reconstruction of the 3D structure.

3.3.4 Image analysis

Image processing and statistical analysis of BIB-SEM images were mainly conducted in ArcMap 10.5 software (Fig 3.3). Due to high grey level contrast between void space and solid phase in SE2 image, pores were automatically segmented by a built-in spatial analyst tool and the pore boundaries were automatically outlined by polygons. After the auto-segmentation, all pore boundaries were manually checked and further edited in case of segmentation errors (Klaver et al., 2012). The statistical geometrical analysis of segmented pores was focused on the morphological features including the minor axis length (W), the major axis length (L), area (A), perimeter (P), circularity ($4\pi A/P^2$) and elongation (1-W/L). Based on the mineral composition obtained from X-ray diffraction (XRD) analysis (Hu et al., 2020b), the mineral phases in the BSE image can be classified as calcite, dolomite, quartz, clay minerals and pyrite by utilization of a grey level thresholding method. The corresponding EDS image was used to

verify the classification. Due to the low contrast of grey level, quartz and clay minerals had to be segmented manually based on their different mineral morphology and distribution characteristics. Finally, the segmented pores can be assigned to different mineral phases by overlaying the pore layer on the mineral layer. Information about pore morphology and porosity can be extracted for each mineral phase. To compare the pore size distributions in different mosaics with different sizes, the pore frequency normalized to the bin width and mosaic area is plotted against the pore area down to the practical pore resolution (PPR, Klaver et al., 2012; Klaver et al., 2015a). When the data points fit a power law relationship, the pore size distribution can be considered as self-similar (Eq.1 and Eq.2).

$$\frac{N_i}{b_i S_{mosaic}} = C \cdot S_{pore}^{-D} \quad (\text{Eq.1})$$

$$\log\left(\frac{N_i}{b_i S_{mosaic}}\right) = -D \cdot \log(S_{pore}) + \log C \quad (\text{Eq.2})$$

Here, b_i is the width of bin (b_i, b_{i+1}) and b_{i+1} doubles b_i , N_i is the frequency of pores with area (S_{pore}) within bin (b_i, b_{i+1}). S_{mosaic} is the total area of the mosaic map. D is the exponent of the power law relationship and C is a constant.

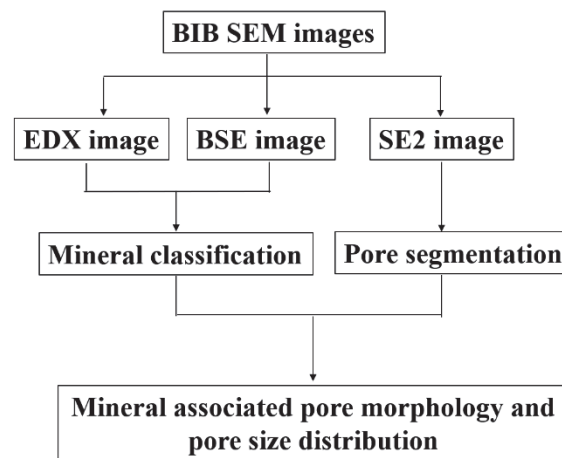


Fig 3.3 Workflow of BIB-SEM image processing.

The BSE images obtained from FIB-SEM were aligned by the software package Dragonfly from ORS company (www.theobjects.com). The reconstructed 3D structure displays 1107×1749×498 voxels with a voxel size of 10 nm. The vertical strips (curtaining artifacts), noise and shadowing effect of the image stack were reduced by destriping, 3D median and 3D background correction filters, respectively. After these image processing steps, segmentation of pores can be achieved due to the high grey level contrast to surrounding minerals. The

contrast of the clay minerals was challenging in the images stack, so Dragonfly's deep learning solution was used to perform the segmentation. By doing so, clay minerals could be separated from calcite and pores within clay minerals could be differentiated from the pores in calcite. After the segmentation, porosity and pore size distribution were analyzed by the 3D Analysis plugin of the image J software (Fiji) (Ollion et al., 2013).

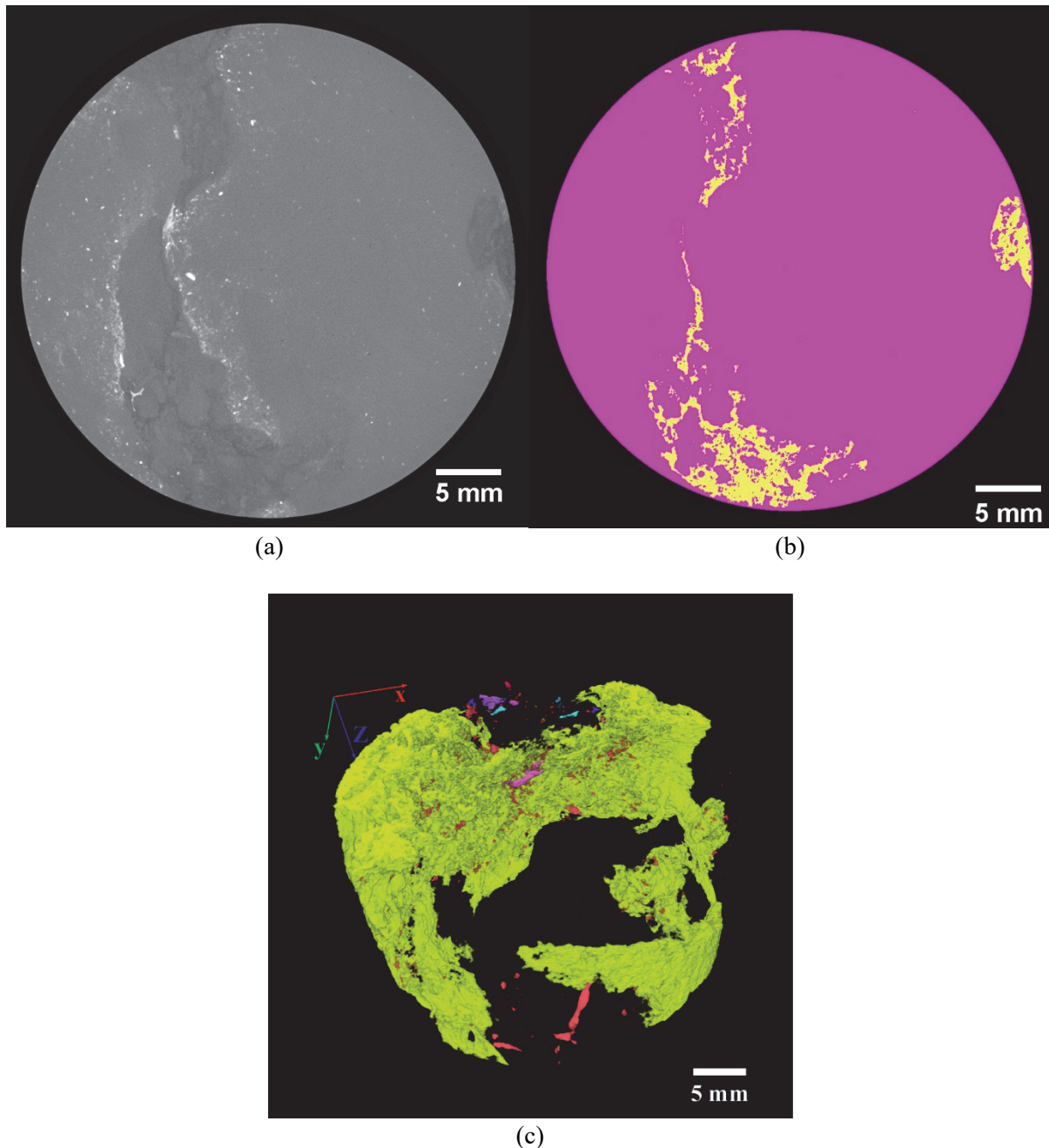


Fig 3.4 Silicate mineral segmentation from the X-ray micro-CT images of sample D by grey level. (a) The original X-ray micro-CT image; (b) The segmented image (yellow standing for the silicate mineral phase and the magenta representing the carbonate mineral phase); (c) The 3D distribution of connected components of silicate mineral phase. The biggest component (yellow) connects the top with the bottom of the plug.

The X-ray micro-CT images of sample D (1000×1000×500 voxels) were first imported into Image J software for segmentation. Although the resolution of 40 μm was not high enough to resolve a single mineral phase, the silicate mineral phase consisting of quartz and clay minerals can be segmented from the carbonate and the remaining mineral phases according to its specific grey level pattern (Fig 3.4a-b). The processing of a large number of images can be accelerated by using the machine learning Trainable Weka segmentation plugin. After segmentation, connected component analysis was conducted by utilization of the MorphoLibJ plugin (Legland et al., 2016) and the connectivity of the silicate mineral phase was visualized. A general description of the underlying theory for the analysis can be found in Breen and Jones (1996).

3.3.5 Permeability simulation

The segmented X-ray micro-CT images were imported in the GeoDict 2019 (Math2Market company) for reconstruction. Digital fluid flow simulations were computed by the FlowDict module, iteratively solving the Stokes equation for a mean flow velocity of each voxel in Z direction. Permeability is further calculated by Darcy’s law with input parameters displayed in Eq.3. Simulations will not stop until the relative difference of permeability is smaller than 1%. To mimic the permeability measurement conditions of the laboratory, helium was used as the permeating fluid and a pressure difference of 2 MPa was applied at constant temperature of 303.15K. It is worthwhile to notice that the derived permeability from the voxel-based simulation is the so-called geometric permeability without consideration of the slippage flow and Knudsen diffusion (Kelly et al., 2016).

$$Q = -\frac{kA}{\mu} \cdot \frac{\Delta P}{L} \quad (\text{Eq.3})$$

Here, Q denotes the flow rate (m³/s) of permeating fluid, k represents the permeability (m²), μ is the viscosity of fluid (Pa·s), ΔP represents the pressure difference, A denotes the cross-sectional area (m²) perpendicular to the flow direction, L is the length (m) of the sample.

Furthermore, permeability coefficients of the BIB-polished subsample were also calculated from the pore statistical analysis based on the “bundle of capillary tubes” model (Peters, 2005; Philipp et al., 2017). For a cuboid sample through which a single circular capillary tube penetrates, the volumetric flow through it can be described by the Hagen-Poiseuille’s law (Eq.4).

$$Q = -\frac{\pi r^4 \Delta P}{8\mu l} \quad (\text{Eq.4})$$

Here, r is the radius (m) of the tube, l denotes the tortuous length (m) of the tube. The combination of Hagen-Poiseuille's law (Eq.4) and Darcy' law (Eq.3) deduces the permeability of a single capillary tube (Eq.5)

$$k = \frac{\pi r^4 L}{8Al} \quad (\text{Eq.5})$$

The cross-sectional area A of the cuboid sample can be expressed as follows:

$$A = \frac{\pi r^2 l}{\phi L} \quad (\text{Eq.6})$$

Here, ϕ and L are the porosity and length of the cuboid sample, respectively. By replacing the cross-sectional area A in Eq.5 with Eq.6, the permeability of a single capillary tube can be defined as:

$$k = \frac{\phi r^2}{8(\frac{l}{L})^2} = \frac{\phi r_{hyd}^2}{8\tau^2} \quad (\text{Eq.7})$$

As suggested by Philipp et al. (2017), hydraulic radius (r_{hyd}) is preferred rather than geometric radius (r) considering the prevailing irregular cross-sectional shape of pores, which is the ratio of pore area to perimeter. The ratio of the tube length (l) to the sample length (L) is defined as the tortuosity (τ), which further simplifies the Eq.7.

With the 2D pore morphology information and assumed tortuosity values, the permeability coefficient of the Cobourg limestone can be estimated as the sum of individual tube permeabilities (Eq.8):

$$k = \sum \frac{\phi r_{hyd}^2}{8\tau^2} \quad (\text{Eq.8})$$

3.4 Results

3.4.1 BIB-SEM image analysis

3.4.1.1 Mineralogy and pore morphology

The Cobourg limestone can generally be characterized as a tight rock dominated by calcite grains of variable sizes (μm - cm) surrounded by idiomorphic or subhedral autogenetic minerals (quartz, dolomite and pyrite) and meshy clay minerals (Fig 3.5). Quantitative mineral area analysis of the overview map indicates that calcite is the dominant mineral phase (84.2%),

followed by clay minerals (6.4%), quartz (4.6%), dolomite (4.0%), pyrite (0.4%) and other unknown minerals (0.5%). Compared to the converted volume fractions of the bulk mineral composition from XRD analysis, the high consistency in carbonate and silicate mineral contents indicates a representative BIB polished section in terms of mineral composition (Table 3.1). For the high-resolution maps 1 and 2, the mineral compositions deviate to different extents from the bulk rock mineral compositions due to sample heterogeneity. BIB-SEM images show that the limestone is generally quite tight though pores can be described according to Loucks et al. (2012). Within the calcite grains, angular pores (sizes up to a few micrometer) were mostly observed (Fig 3.6a). Intraparticle pores also appear in rhombic dolomite (Fig 3.6c). Intercrystalline pores can be observed in framboidal pyrites (Fig 3.6d). However, these framboidal pyrites are relatively rare and the clusters are mostly isolated from each other, and therefore deemed irrelevant for fluid flow. Pores in the clay mineral fraction are relatively small, triangular and slit-shaped (Fig 3.6b & 3.6e), which is typical for pores in clay minerals (Desbois et al., 2009). Furthermore, microfractures also tend to appear at the interface of carbonate and clay fractions (Fig 3.6c & 3.6f). Considering the matching edges and sharp tips, these fractures are interpreted as artifacts caused by stress release during sampling, preparation and drying and are therefore excluded in the porosity and pore size analyses.

In map 1, the average pore circularity in the clay mineral phase is lower than that of the pores in the calcite phase (0.47 vs 0.59) and the average pore elongation in the clay minerals is higher than that of the pores in calcite (0.62 vs 0.48). The same trends are apparent for pores in map 2. The difference in pore shape factors indicate relatively more slit-shaped pores occurring in the clay fraction. In our study, based on the circularity values, pores in Cobourg limestone are classified as high circularity pores ($0.6 \leq \text{Circularity} < 1$), slit-shaped pores ($0.125 < \text{Circularity} < 0.6$), or as fractures ($\text{Circularity} \leq 0.125$, excluded). In the calcite phase, high circularity and slit-shaped pores account for 40-41% and 59-60%, respectively (Fig 3.7), whereas slit-shaped pores are dominant in the clay mineral phase (82-88%).

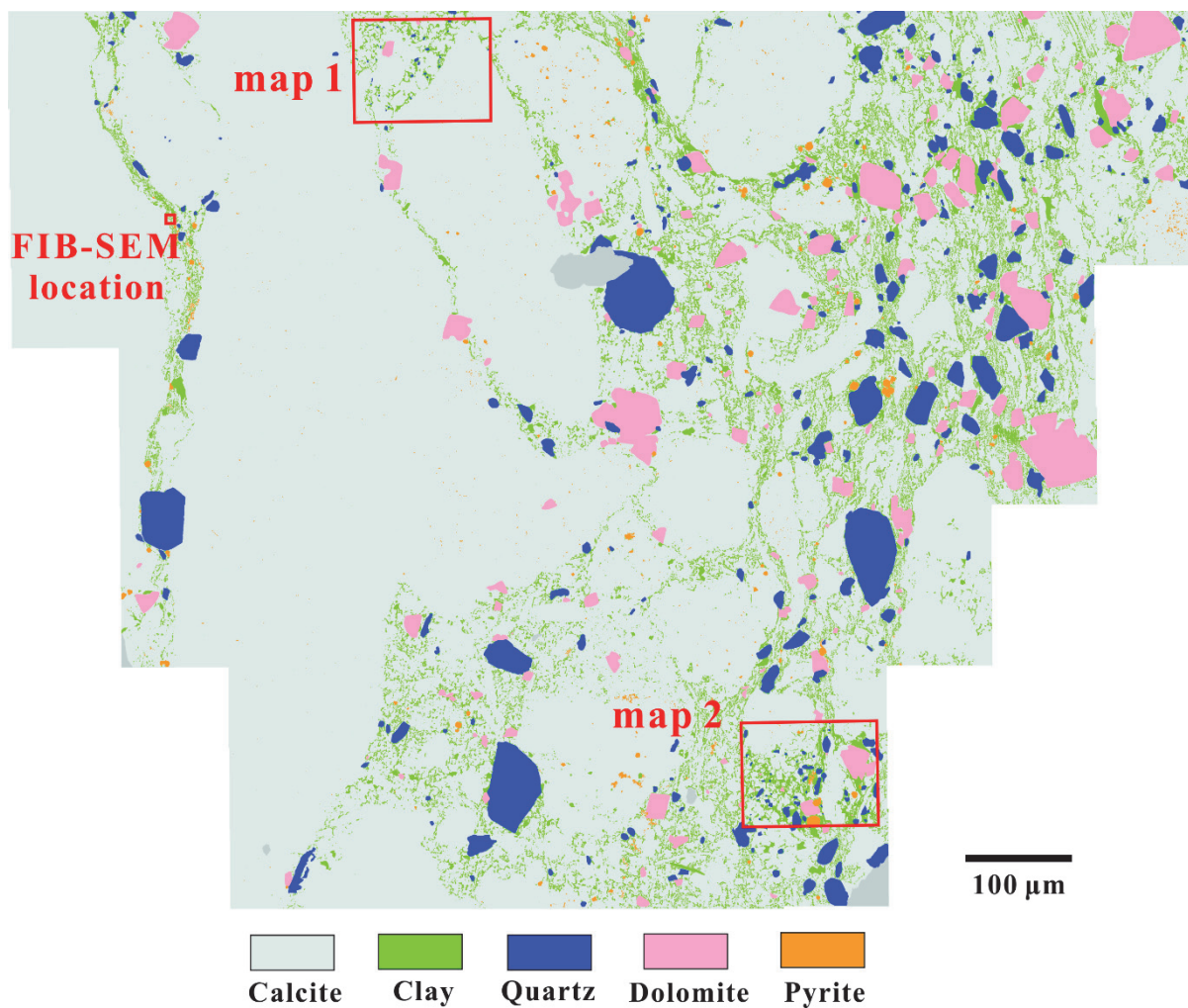


Fig 3.5 Mineral distribution overview of BIB-polished Cobourg limestone surface (0.72 mm^2). The red squares show the areas of BIB-SEM maps 1 and 2 and the location for FIB-SEM.

Table 3.1 Mineralogical composition obtained from BIB- and FIB-SEM, micro-CT and XRD analyses of Cobourg limestone.

Sample	Calcite (%)	Dolomite/Ankerite (%)	Clay minerals (%)	Quartz (%)	Pyrite (%)	Others (%)	Carbonate (%)	Silicate (%)
BIB-SEM_map 1	89.5	1.2	8.4	0.8	0.1	0.0	90.7	9.2
BIB-SEM_map 2	61.2	7.6	20.9	8.4	2.0	0.0	68.7	29.3
FIB-SEM_volume	95.6		4.39				95.6	4.39
BIB-SEM_overview map	84.1	4.0	6.5	4.6	0.4	0.5	88.1	11.1
Micro-CT_sample D							86.9	13.1
XRD analysis*	80.0	8.4	6.4	5.0	0.3	0.0	88.4	11.4

*The weight percentage of each mineral component obtained from XRD analysis has been converted to volume fraction by assigning respective density.

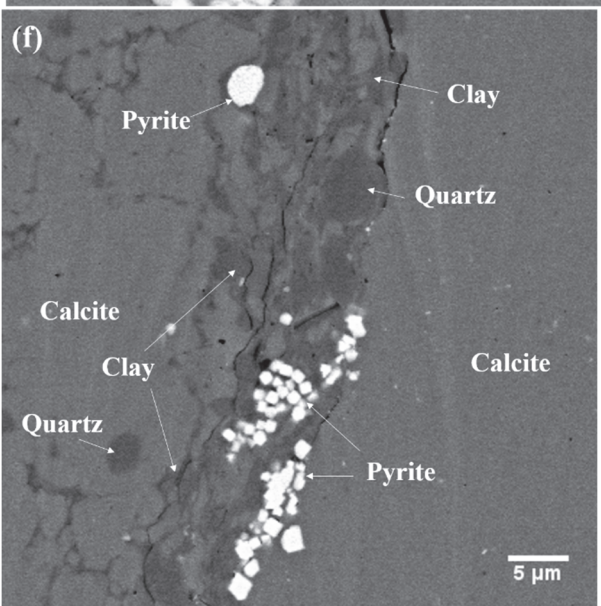
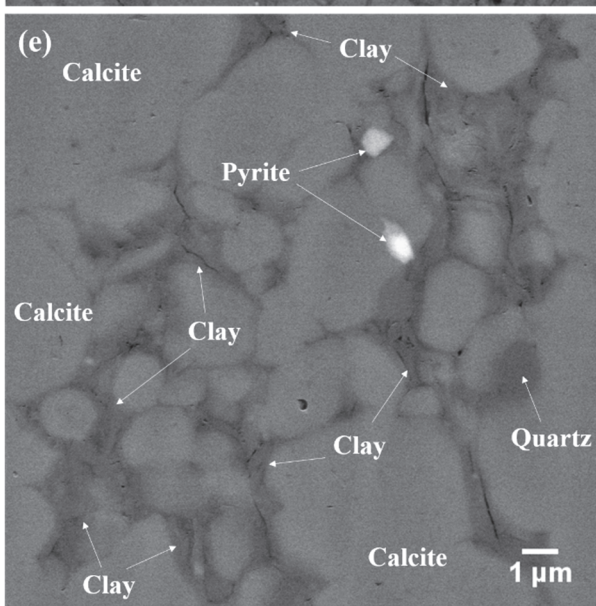
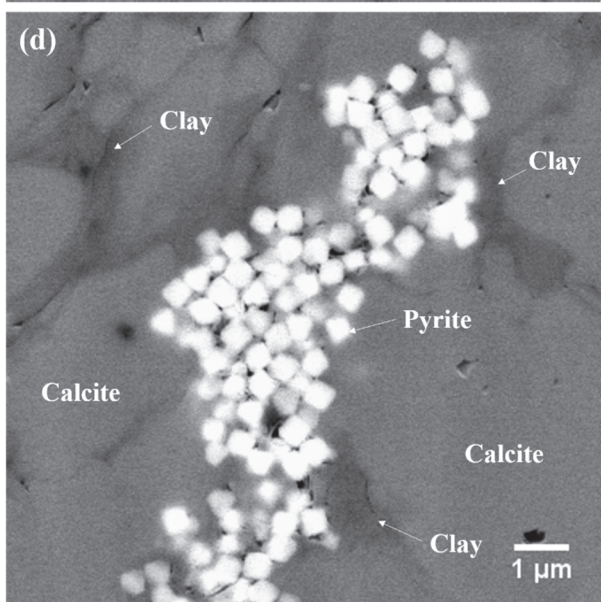
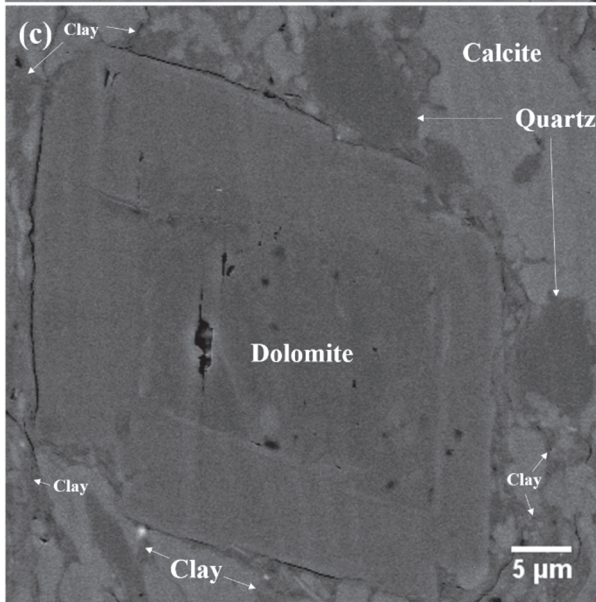
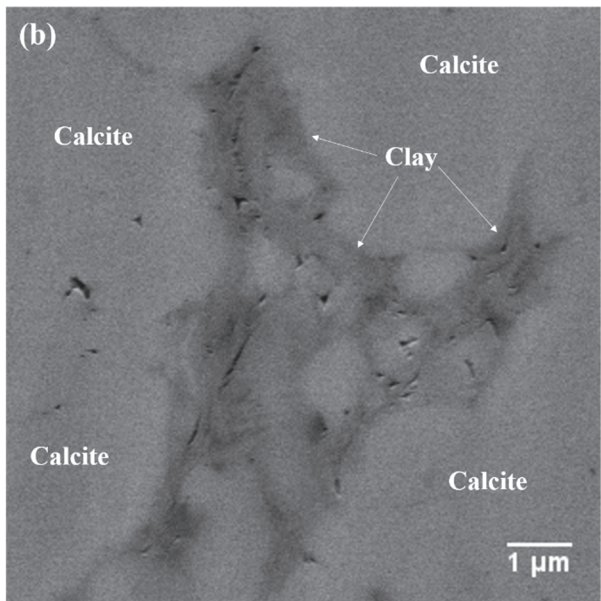
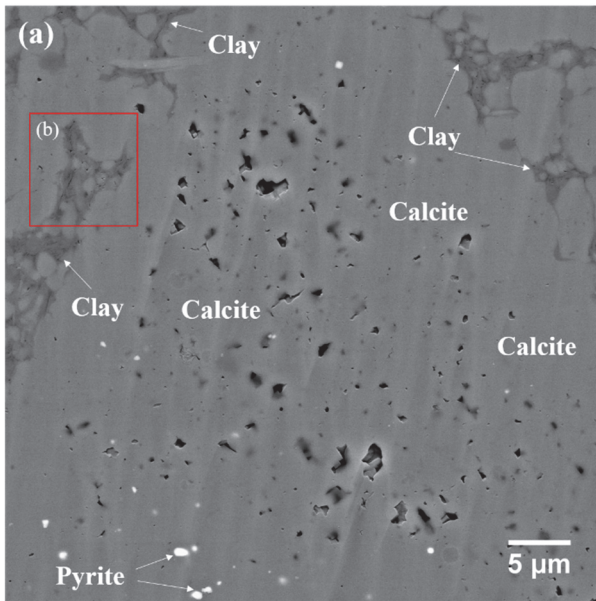


Fig 3.6 BSE images of Cobourg limestone. (a) Angular intraparticle pores with sizes up to a few micrometer in calcite grains and clay minerals randomly distributing among calcite grains; (b) The high resolution image showing the submicron triangular and elongated pores in the clay fraction; (c) Intraparticle pores in rhombus dolomite and microfractures at the interface between carbonate and clay fractions; (d) Intercrystalline pores in framboidal pyrites. (e) Submicron slit-shaped pores in the clay fraction; (f) Microfractures accumulating at the interface between calcite and clay fractions.

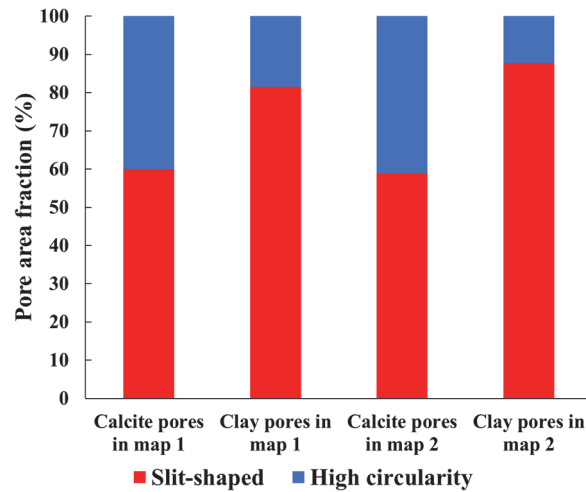


Fig 3.7 Area fractions of slit-shaped and high circularity pores in calcite and clay mineral phases of maps 1 and 2.

3.4.1.2 Porosity and pore size distribution

For quantitative porosity and pore size distribution analyses, the PPR is defined as 10 pixels, corresponding to an equivalent area of a circle with a diameter about 52 nm at a magnification of 20000 \times . The total porosities of maps 1 and 2 are 0.68% and 0.41%, respectively (Table 3.2). As expected, these values are lower than the bulk porosity values (0.98-2.51%) determined by HP for samples B, C, D and E because the majority of pores likely is in the fine meso- and micropore range and thus below the imaging resolution. Concerning the porosity of specific mineral phases, the clay mineral phase is the most porous mineral phase (1.06-1.11%) in both maps, followed by pyrite (0.60-0.88%), calcite (0.24-0.65%), quartz (0.16-0.18%) and dolomite (0.03-0.08%). Furthermore, calcite and clay mineral phases contribute 36.2–85.9% and 13.7–54.6% to the total visible pore areas in maps 1 and 2, respectively. In total, the pore area within these two phases accounts for 99.7% and 90.9% of the total visible pore areas in maps 1 and 2, respectively.

Table 3.2 Porosities of different mineral phases in BIB-SEM maps and FIB-SEM volume and bulk porosities measured by HP.

sample	BIB-SEM image analysis						He pycnometry	FIB-SEM image analysis		
	Calcite	Dolomite	Clay minerals	Quartz	Pyrite	Total		Calcite	Clay minerals	Total
A	BIB-SEM map 1	0.65%	0.03%	1.11%	0.18%	0.60%	0.68%			
	BIB-SEM map 2	0.24%	0.08%	1.06%	0.16%	0.88%	0.41%			
	FIB-SEM volume							0.32%	1.46%	0.37%
B							1.02%			
C							0.98%			
D							2.51%			
E							1.83%			

Fig 3.8a-b show pore size distributions (pore frequency vs equivalent circular pore diameter) of total visible pores in maps 1 and 2. For both maps, the equivalent circular pore diameter is up to 1155 nm and the pore frequency decreases with increasing equivalent circular pore diameter. The same trend is also evident for the individual mineral phases (calcite and clay) (Fig 3.8c-f). The calcite pores in map 1 cover a larger pore size range as compared to those in map 2. The majority of clay pores in both maps are smaller than 500 nm. The logarithm of the pore frequency normalized to the bin width and mosaic area shows a linear correlation with the logarithm of the pore area, indicating self-similar characteristics of the pore size distribution in the Cobourg limestone (Fig 3.9a and 3.9c-d). Therefore, the relationship between the logarithm of the pore area and the logarithm of the normalized pore frequency for total visible pores in maps 1 and 2 can be described by the power law exponent D between 2.04 and 2.25 and $\log C$ values between -2.91 and -2.11 (Fig 3.9a; Table 3.3). The relationship in the calcite pores can be described by D values between 1.93 and 2.18 and $\log C$ between -3.51 and -2.84, while the relationship in the clay pores is characterized by higher D values between 2.50 and 2.59 and $\log C$ values between -1.37 and -1.32 (Fig 3.9c-d). The cumulative porosity in the clay mineral phase increases stronger than that of the calcite phase with decreasing equivalent circular pore diameter (Fig 3.9b). Similarly, the pore area fraction in the clay mineral phase increases stronger, from a relatively low fraction ($< 5\%$), with the equivalent circular pore diameter decreasing from 1000 nm to 100 nm (Fig 3.9e-f). This trend also occurs in calcite pore area fraction in map 2 (Fig 3.9f). However, for the calcite pore area fraction in map 1, a peak occurs at an equivalent circular pore diameter ranging from 578 to 817 nm, followed by an approximately linear reduction of the pore area fraction with decreasing equivalent circular pore diameter (Fig 3.9e).

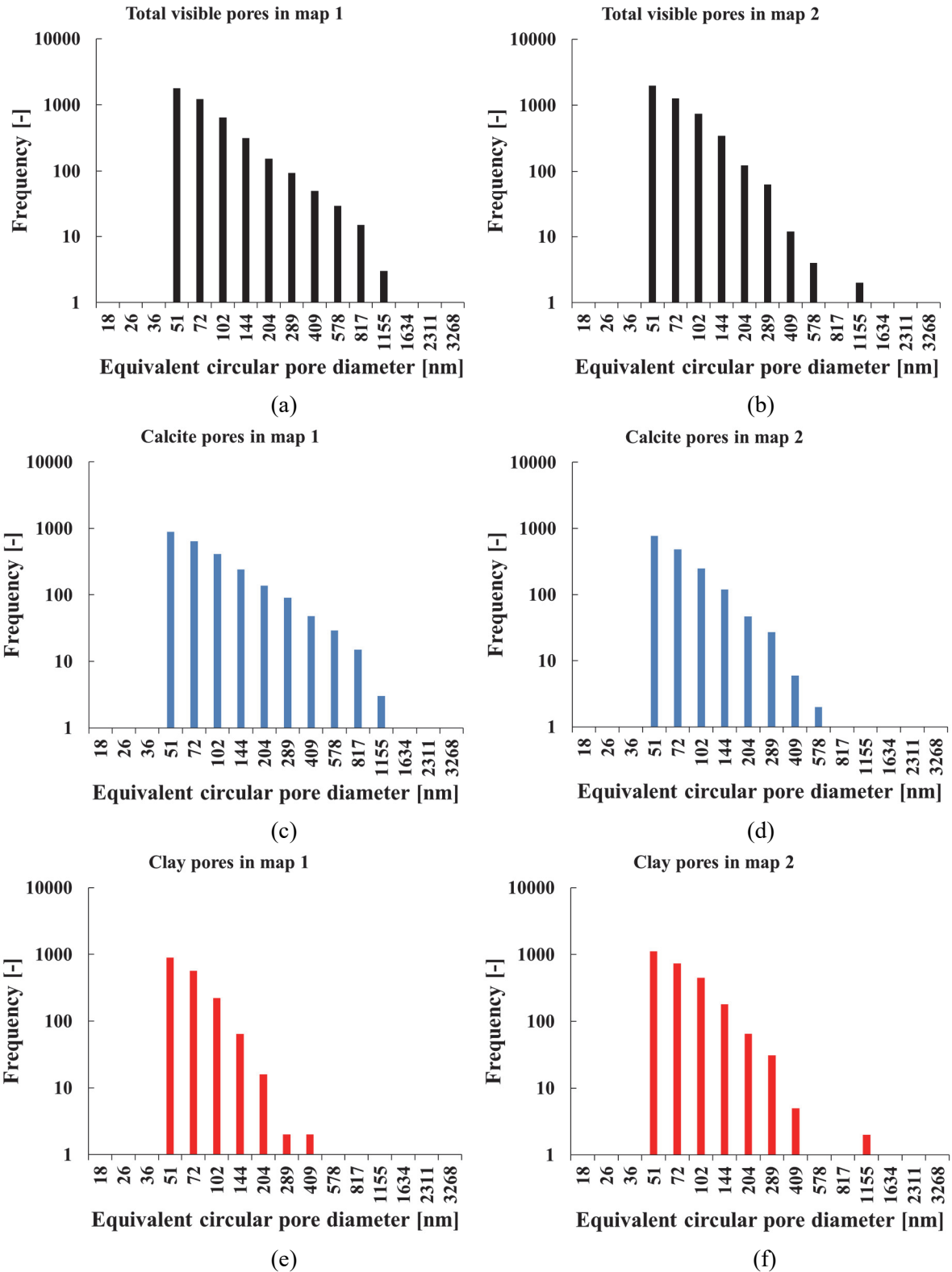
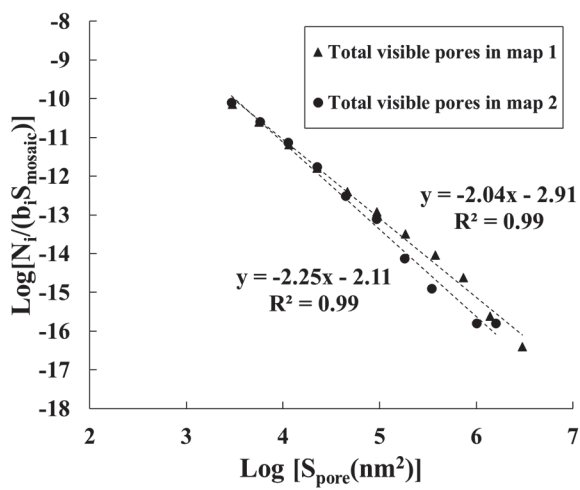
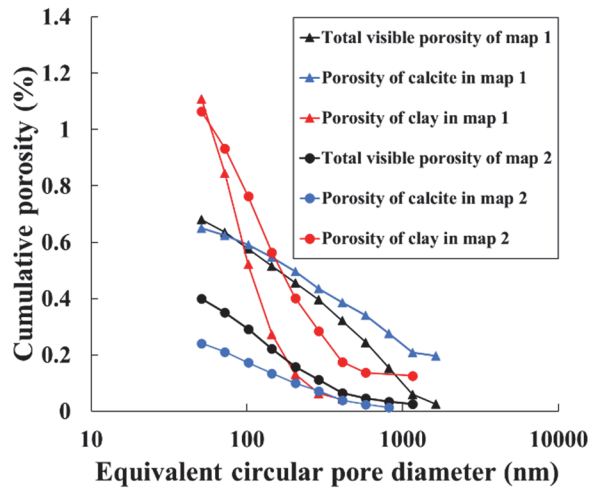


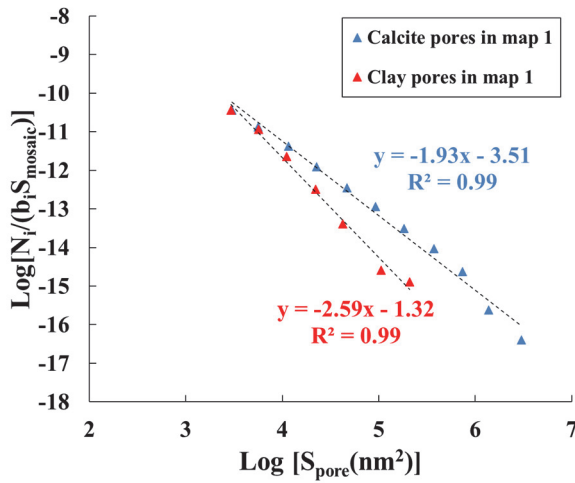
Fig 3.8 Frequency distributions (pore frequency vs equivalent circular pore diameter) of total visible pores in BIB-SEM map 1 (a) and map 2 (b); Frequency distributions of visible pores in calcite (c) and clay mineral (e) phases of map 1; Frequency distributions of visible pores in calcite (d) and clay mineral (f) phases of map 2.



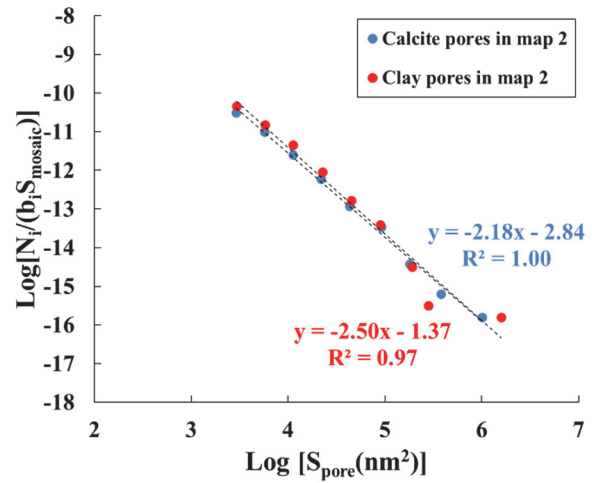
(a)



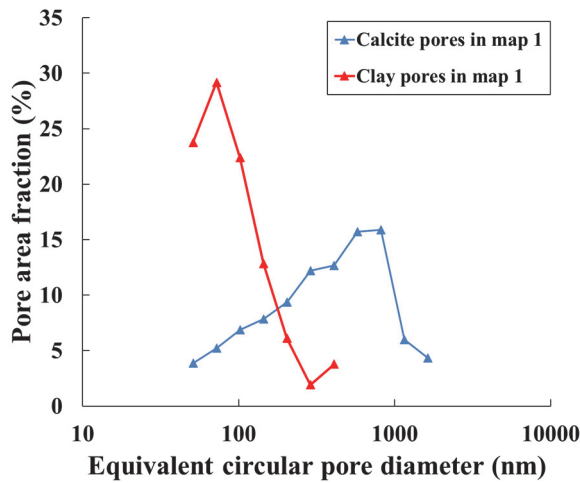
(b)



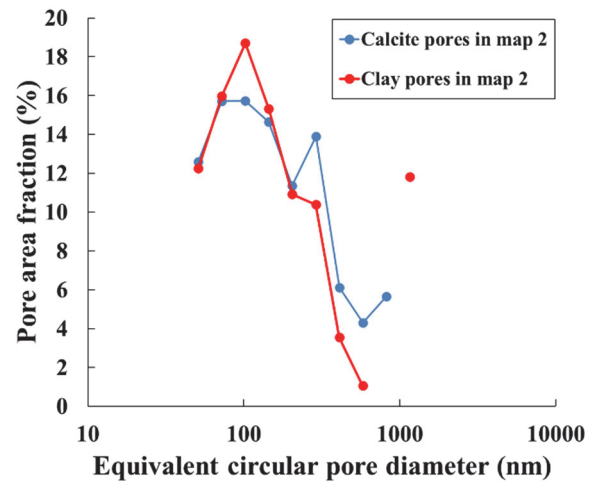
(c)



(d)



(e)



(f)

Fig 3.9 Normalized pore size distributions of total visible pores in maps 1 and 2 (a). The linear best fit is shown as a dashed line with a corresponding equation. The slope and intercept of the best fit are the minus D and $\log C$ values of Eq. 2, respectively. Cumulative porosity distributions of total visible pores

in maps 1 and 2 and corresponding cumulative porosity distribution of clay and calcite phases (pore area normalized to respective mineral phase area) (b). Normalized pore size distributions in calcite and clay mineral phases of map 1 (c) and map 2 (d). Pore area fraction distributions of calcite and clay mineral phases in map 1 (e) and map 2 (f).

Table 3.3 Power law exponents (D) and constants ($\log C$) for pores in calcite phase, clay mineral phase and total phases.

Mineral phase	Calcite		Clay		Total	
	D	log C	D	log C	D	log C
map 1	1.93	-3.51	2.59	-1.32	2.04	-2.91
map 2	2.18	-2.84	2.50	-1.37	2.25	-2.11
FIB-SEM images			2.59		2.04	

3.4.2 FIB-SEM image analysis

An area rich in clay minerals was selected on the BIB-polished surface for the FIB-SEM tomography to visualize and investigate pore networks therein (Fig 3.5). The PPR is defined as 8 voxels, corresponding to an equivalent volume of a sphere with a diameter of approximately 25 nm. Analysis of the FIB-SEM volume shows that the volumetric content of the clay mineral phase (green) is 4.39% and that of the calcite phase (white) is 95.61% (Fig 3.10). The total porosity of the bulk sample is 0.37%. The porosity of the clay mineral phase (green) is 1.46 %, which is comparable to the porosities of clay mineral phases (1.06-1.11%) obtained from maps 1 and 2 (Table 3.2). The pore size in the clay mineral phase is up to 570 nm and the sum of volumetric fractions of pores between 25 and 50 nm are 6.45% (Fig 3.11a). Regarding the calcite phase, its porosity is 0.32%, close to the value (0.24%) of map 2 (Table 3.2). The pore size in the calcite phase is up to 760 nm (Fig 3.11a). Compared to the pore size distribution of the calcite phase, pores with the size larger than 300 nm rarely develop in the clay mineral phase (only a single pore was detected with a maximum equivalent spherical pore diameter of 570 nm). For the calcite phase, the sum of volumetric fractions of pores between 25 and 50 nm is only 0.78%. Evidently, the pore volumes in both clay mineral and calcite phases are dominated by macropores, while the coarse mesopores (25-50 nm) in the clay mineral phase are more abundant than that in the calcite phase (Fig 3.11a). Similar to the BIB-SEM image analyses, the cumulative porosity in clay mineral phase increases stronger than that of calcite phase with decreasing equivalent spherical pore diameter (Fig 3.11b). The

logarithm of the 2D pore area linearly correlates well with the logarithm of the normalized clay pore frequency in the FIB-SEM images when excluding the data points below the PPR (Fig 3.11c).

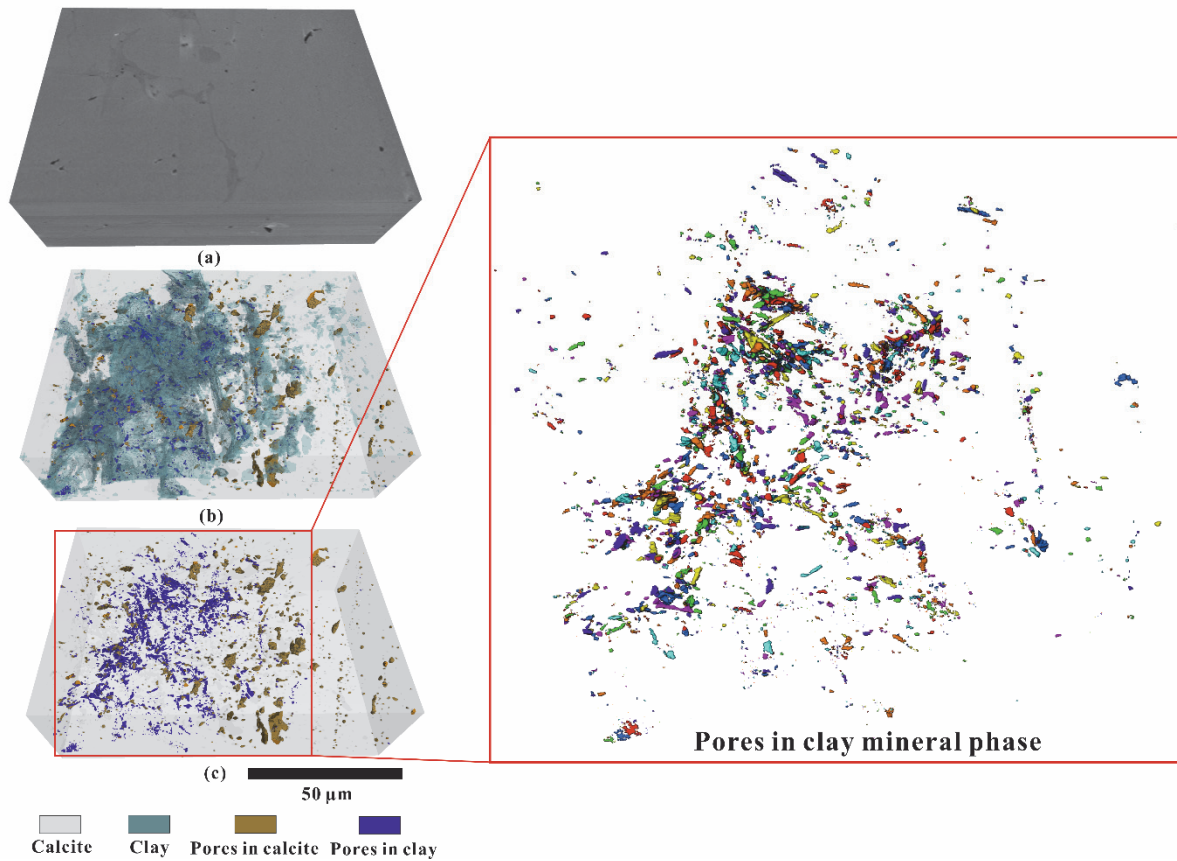


Fig 3.10 Dragonfly's deep learning segmentation results for the FIB-SEM image stack: (a) Original greyscale 3D rendered structure of FIB-SEM image stack (10 nm voxel size); (b) Clay mineral phase (green) is separated from calcite phase (white) and pores in calcite (gold) and pores in clay (blue) are segmented; (c) The 3D distribution of pores in clay and calcite. The pores in calcite phase are apparently isolated to each other and no connected pores are identified in clay mineral phase when zooming in (different colors used to differentiate adjacent pores in clay).

Due to the resolution limitation, identified pores in calcite and clay mineral phases are isolated from each other and therefore no connected pore network could be reconstructed (Fig 3.10). However, shortest distance analysis between pores and their nearest neighbors (edge to edge) shows that 80% of the pores in the clay mineral phase and 41% of pores in the calcite phase are at a distance of ≤ 100 nm from each other (Fig 3.11d). The average shortest distances are 83.5 and 224.6 nm in the clay mineral and calcite phases, respectively.

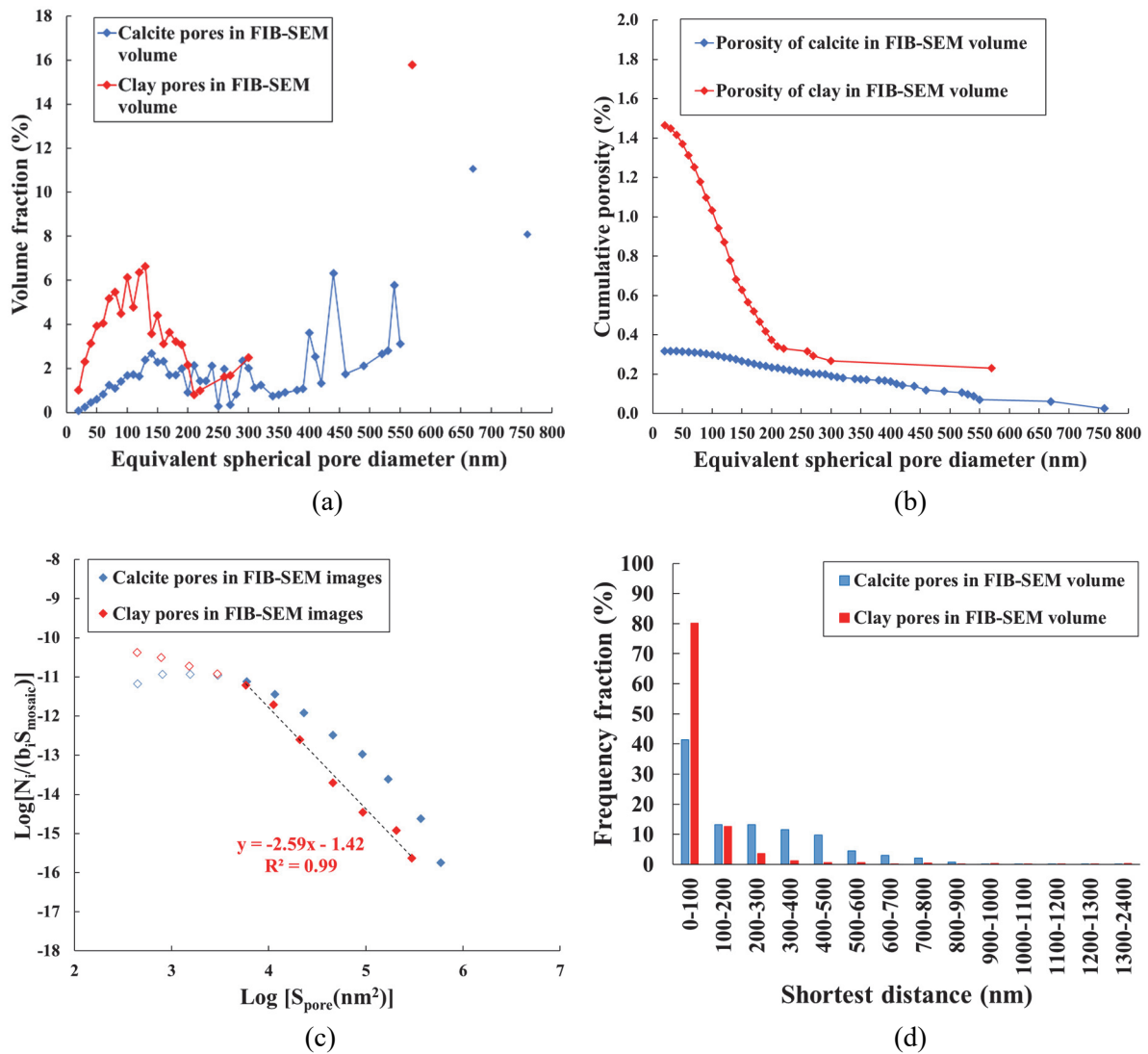


Fig 3.11 Pore volume fraction distributions (a) and cumulative porosity distributions (pore volume normalized to respective mineral phase volume) (b) of calcite and clay mineral phases of FIB-SEM volume. Normalized pore size distributions in calcite and clay mineral phases based on 2D FIB-SEM image analyses (c). The linear best fit is shown as a dashed line with a corresponding equation. The slope and intercept of the best fit are the minus D and $\log C$ values of Eq. 2, respectively. The hollow blue and red squares represent the normalized frequencies of pores in calcite and clay when the equivalent circular pore diameter is equal or smaller than 51 nm, respectively. These data points are excluded to obtain linear best fits. The frequency fraction distribution of the shortest distance (edge to edge) between each pore and its nearest neighbor in calcite and clay mineral phases of the FIB-SEM volume (d).

3.4.3 X-ray micro-CT image analysis

Because of low contrast, only silicate (quartz + clay minerals) and carbonate mineral phases could be separated. Additionally, because of resolution no pores could be segmented in either phase. The volumetric content of the silicate mineral phase in the reconstructed X-ray micro-

CT image stack is 13.09% (Table 3.1). Connected component analyses show that the silicate mineral phase is connected from top to bottom of the plug (Fig 3.4c).

3.4.4 Permeability simulation

3.4.4.1 BIB-SEM images

Permeability estimation using the “bundle of capillary tubes” model from 2D BIB-SEM images were only performed on map 1 as it is representative of the bulk sample with respect to the mineralogy (Table 3.1). Based on the 2D pore cross-sections, the sum of individual tube permeability coefficients of the different mineral phases was expressed as a function of tortuosity (Eq.8; Fig 3.12). With increasing tortuosity, permeability coefficients will invariably decrease irrespective of the mineral phase. It should be noted that the tortuosity has to be regarded as a fudge factor with only limited physical meaning (Ghanbarian et al., 2013). Nevertheless, it can be used to converge permeability coefficients from BIB-SEM analyses with laboratory measurements (5.21×10^{-20} - 2.74×10^{-19} m²). Taking into account all pores (calcite and clay mineral phases), BIB-SEM derived permeabilities match those from laboratory measurements at a tortuosity range from 8 to 15. If the calcite phase is excluded from the calculation, permeability coefficients of the clay mineral phase converge with permeability coefficients measured in the laboratory, if the tortuosity is ≤ 1 .

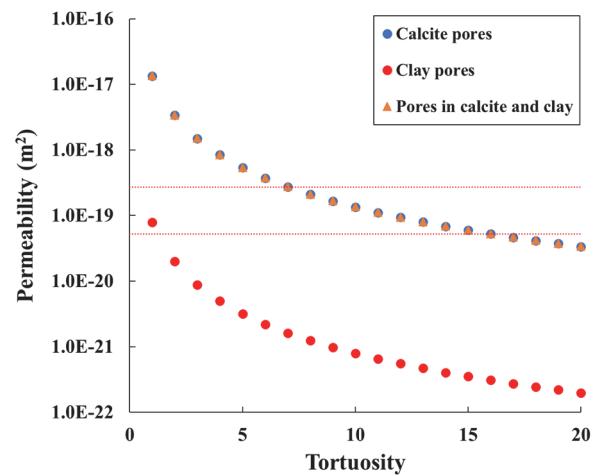


Fig 3.12 Simulated permeability coefficients based on a range of tortuosity values and 2D pore cross-sections in calcite, clay and both mineral phases of map 1. The dashed bounds are the lab-measured permeability range (5.21×10^{-20} - 2.74×10^{-19} m²) of intact Cobourg limestone samples (C, D and E).

3.4.4.2 X-ray micro-CT image stack

Permeability coefficients of specific mineral phases can theoretically be inversely calculated from the laboratory-measured permeability coefficients. If the silicate phase is considered as an impermeable phase, then the permeability coefficient of the carbonate phase can be inversely calculated. Therefore, a series of isotropic permeability coefficients (10^{-18} , 10^{-17} , 10^{-16} m²) were assigned to the carbonate phase (Table 3.4). The simulated permeability for the whole reconstructed volume linearly increases with increasing isotropic permeability assigned to the carbonate phase. Based on this relationship, the isotropic permeability coefficients of the carbonate phase range from 6.87×10^{-20} to 3.61×10^{-19} m² to match laboratory derived permeabilities for the intact bulk samples (samples C, D and E). If, however, the carbonate phase is taken as an impermeable phase, which can be regarded as an endmember case in which all pores of the carbonate phase occur as isolated pores, the isotropic permeability coefficients of the silicate phase range from 1.74×10^{-18} to 9.17×10^{-18} m² to match laboratory derived permeabilities. The sensitivity of the permeability simulation was evaluated by dilating the segmented silicate phase by 1 voxel, which is equivalent to an increase of 13.09 to 17.92 vol.% of the silicate phase. Results showed that the permeability coefficient increases significantly by 90% after dilation (Table 3.4).

Table 3.4 The simulated permeability coefficients of sample D at corresponding isotropic permeability, pressure difference and temperature by using the FlowDict module of GeoDict. Isotropic permeability is assigned to silicate or carbonate phase when silicate or carbonate phase is taken as the only permeable phase.

Pressure difference (MPa)	Temperature (K)	Only carbonate phase permeable		Only silicate phase permeable		
		Isotropic permeability (m ²)	Simulated permeability (m ²)	Isotropic permeability (m ²)	Simulated permeability (m ²)	Simulated permeability after dilation* (m ²)
2	303.15	1.00×10^{-18}	5.15×10^{-19}	1.00×10^{-18}	2.99×10^{-20}	
2	303.15	1.00×10^{-17}	5.15×10^{-18}	1.00×10^{-17}	2.99×10^{-19}	5.65×10^{-19}
2	303.15	1.00×10^{-16}	5.15×10^{-17}	1.00×10^{-16}	2.99×10^{-18}	

3.5 Discussion

3.5.1 Methodological comparison of porosity

Total porosities obtained from BIB- (0.41 to 0.68%) and FIB-SEM (0.37%) were lower than effective porosities obtained from HP (0.98 – 2.51%). Differences between BIB-SEM and HP

derived porosities can be attributed either to the resolution of generated BIB-SEM images or sample heterogeneity.

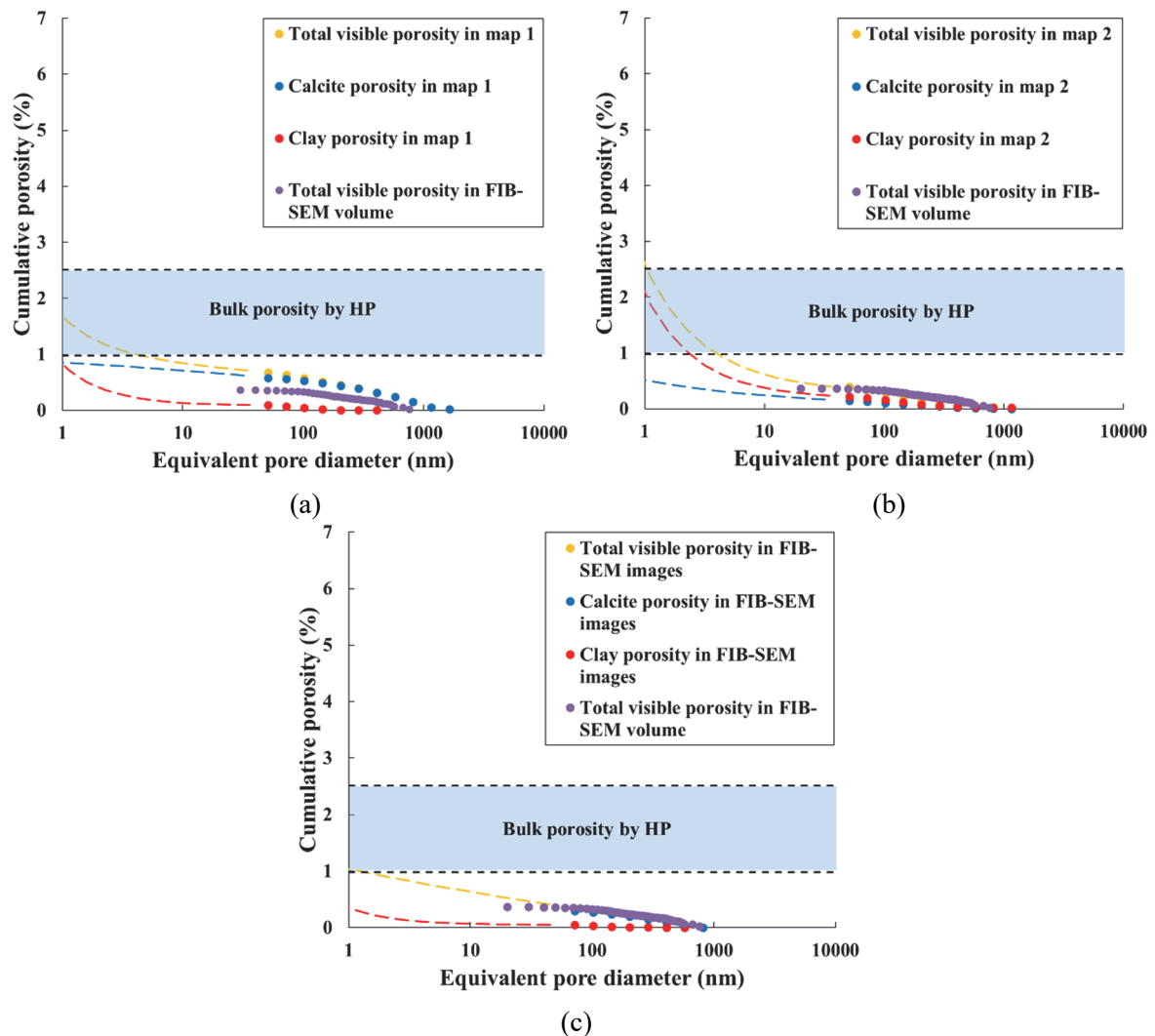


Fig 3.13 Extrapolation of cumulative porosity distributions obtained from BIB-SEM map 1 (a), map 2 (b) and FIB-SEM images (c). Cumulative porosity distribution obtained from FIB-SEM volume (purple data point) and HP bulk porosities of samples B, C, D and E (blue zone) are compared. D and $\log C$ values are utilized for the extrapolations of cumulative calcite and clay porosities, which are represented by the blue and red dashed lines, respectively. The extrapolation of cumulative total porosity in map 1 and 2 is the sum of extrapolated cumulative calcite and clay porosities and represented by the yellow dashed line. As no linear relationship exists in the normalized pore size distribution of calcite phase in FIB-SEM images, D and $\log C$ are utilized for the extrapolation of cumulative total porosity in FIB-SEM images. All the porosities are pore areas or pore volumes normalized to total image areas or total structure volumes.

Recognition of pores in the BIB-SEM maps starts from an equivalent circular pore diameter of 52 nm (pore area equivalent to 10 pixels at 20000 \times), whereas helium has access to pores down

to 0.26 nm (Joos and Freeman, 2013). Clay minerals in the Cobourg limestone are dominated by illite and interstratified illite/ smectite (Day et al., 2017; Hu et al., 2020b). Since the smallest basal spacing of these TOT type clays is 1 nm (Jlassi et al., 2017) D values obtained from imaging analyses can be used to extrapolate down to the pore size of 1 nm in order to compare porosities from imaging methods and HP measurements. It is evident for map 1 that after extrapolation, total visible porosities from map 1 are well within the range of HP derived porosities (Fig 3.13a; Table 3.2), whereas total visible porosities for map 2 and FIB-SEM images are at the upper and lower boundaries of HP derived porosities. Similar findings were also made by Klaver et al. (2015a) who compared MIP and BIB-SEM derived porosities of the Haynesville and Bossier shales. This indicates that extrapolation to pore areas that are otherwise unresolved by imaging techniques can be used to give first approximations of HP derived porosities. It should be noted that HP derived porosities only give information on the effective (accessible) porosity whereas BIB-SEM derived porosities should give information about effective as well as isolated porosities. Since the porosities are in the same range, this might indicate that there is no significant amount of isolated porosity in these maps, as the extrapolated porosities from BIB-SEM images would otherwise have to be higher when compared to HP derived porosities.

Heterogeneity is always a critical factor in the interpretation of petrophysical rock properties (Peters, 2005; Philipp et al., 2017; Kelly et al., 2016). It can be seen from Fig 3.13 and Table 3.2 that porosities for sample B, C, D, and E vary by an absolute porosity of 1.53% at an average porosity of 1.58%. Additionally, total visible porosities of map 1, map 2 and FIB-SEM images differ strongly, which can be related to a significantly different mineralogical composition (Table 3.2; Fig 3.13). Total visible porosities from map 1 can be regarded as the most representative porosities when compared to the bulk rock HP measurements because of a similar mineralogical composition, whereas map 2 and FIB-SEM images rather reflect upper and lower boundaries with respect to the heterogenous distribution of clay minerals on the micro scale.

3.5.2 Pore morphology and pore size distribution

Based on quantitative analyses of the BIB-SEM images, it is evident that the pore geometry and pore size distribution of the Cobourg limestone are closely related to the mineralogy. In this study, the focus was on the calcite and clay mineral phases since the pore areas in these two phases represented the majority of the total pore area (up to 99.7 %). To investigate the

pore morphology, quantitative circularity analyses revealed that most of the visible pores in the clay mineral phase were generally present as slit-shaped pores, whereas those in the calcite phase were present as slit-shaped and high circularity pores with comparable amounts (Fig 3.7). Within the common resolvable pore size range (> 51 nm), the normalized pore size distributions in the clay mineral phase from FIB-SEM images are similar to those from BIB-SEM images. D values derived from both methods measured in the clay mineral phase (2.50-2.59) are higher than those measured in the calcite phase (1.93-2.18) (Fig 3.9c-d & 3.11c). Similar findings are reported by Klaver et al. (2015a) for shales from the Haynesville and Bossier Formations. Although no linear relationship exists in the normalized pore size distribution of the calcite phase in the FIB-SEM images, a trend of lower frequencies for pore sizes below the PPR in the calcite phase as compared to the clay mineral phase is evident (Fig 3.11c). Therefore, based on the D values, once extrapolated to pores smaller than PPR, the frequency of pores that cannot be resolved by imaging techniques in the clay mineral phase is expected to be much higher than that in the calcite phase.

A relatively larger volume fraction of large mesopores (25-50 nm) in the clay mineral phase is evident when compared to the calcite phase as well (Fig 3.11a). Nevertheless, visible pore volumes in both phases are dominated by macropores. However, this observation is probably related to the resolution limit of the imaging technique. It is likely that fine mesopores and micropores significantly influence the total pore volume. This can be seen in Fig 3.13, where micro- and mesopores that cannot be resolved in the SEM images account for up to 73% of the total pore volume.

The pore space distribution of the 3D reconstructed volume from FIB-SEM images is displayed in Fig 3.10 and indicates that all pores, irrespective of the mineral phase, are isolated. The reason is that the connections of the pores are likely below the resolution of FIB-SEM images. It should be noted that pores in the clay mineral phase are generally closer to each other as compared to pores in the calcite phase, which is also indicated by the shortest distance analysis (Fig 3.11d). Hence, it is more likely that these pores are connected more frequently with pore throats below the resolution (10 nm) of the FIB-SEM images as compared to pores in the calcite phase (Curtis et al., 2012; Keller et al., 2013; Kelly et al., 2016).

Increasing D values in the order of FIB-SEM images (2.04, 4.39% clay content), map 1 (2.04, 8.4% clay content) and map 2 (2.25, 20.9% clay content) illustrate the influence of the clay mineral content on the pore size distribution (a shift towards smaller pores) (Table 3.3). Philipp

et al. (2017) studied the pore size distribution of the shaly (75.9-83.6% clay content), sandy (40.6-71.9% clay content) and carbonate-rich (29.6-37.6% clay content) facies of Opalinus Clay and also observed increasing D values with increasing clay mineral content in the order of carbonate-rich facies (1.84-2.05) < sandy facies (2.20-2.43) < shaly facies (2.30-2.50).

3.5.3 Dominant flow pathways

This study investigated a potential feasibility of FIB-SEM and X-ray micro-CT reconstructed volumes as well as 2D BIB-SEM images for permeability simulations in the Cobourg limestone. The main motivation for the image analyses used here is that the Cobourg limestone shows an exceptionally high variability of permeabilities by up to 6 orders of magnitude. This is likely related to combined effects of heterogeneity, anisotropy and fractures (Davy et al., 2019) and could potentially be investigated by image analyses. Especially the existence of a relatively dark (clay-rich) and relatively light (carbonate-rich) fraction of the rock was postulated to significantly influence the permeability (Cavé et al., 2009; Letendre, 2011; Day et al., 2017), even as such that only the relatively dark (clay-rich) phase was assumed to be mainly relevant for flow (Selvadurai and Głowacki, 2018; Selvadurai et al., 2019; Hu et al., 2020b).

In this study FIB-SEM was performed on such a macroscopically relatively dark (clay-rich) fraction of the rock to investigate transport properties in more detail. However, a lack of pore connectivity and therefore percolation pathways in the FIB-SEM reconstruction implies that permeability simulations are not feasible for this rock using FIB-SEM (i.e. pore throats are below the resolution of imaging). Additionally, FIB-SEM is known to lack rock representativity because of the small sample volume of approximately 1000 μm^3 (Keller et al., 2011; Kelly et al., 2016), which is especially relevant for the heterogenous Cobourg limestone.

Although X-ray micro-CT captures larger sample volumes ($\sim 40 \text{ cm}^3$), neither pores nor clay and quartz could not be distinguished and hence only the bulk silicate mineral phase could be segmented from the carbonate mineral phase. Under assumption of an impermeable carbonate mineral phase (dominant flow pathways in the relatively dark fraction of the rock), permeability coefficients of the silicate phase were inversely computed to be 1.74×10^{-18} to $9.17 \times 10^{-18} \text{ m}^2$. Such high permeability coefficients for fluid pathways in clay-dominated rocks, however, appear to be unrealistic if compared to measurements performed on mudstones with varying clay contents and porosities (Yang and Andrew, 2007; Yang and Andrew, 2010; Ghanizadeh et al., 2014; Mckernan et al., 2014). This indicates that flow through the silicate

mineral phase only is not likely. It should be mentioned that the upper limit of computed permeability coefficients from CT for the silicate mineral phase only is approaching the extrapolated permeability ($1.79 \times 10^{-17} \text{ m}^2$) of fractured sample B at zero effective stress. The feasibility of X-ray micro-CT imaging for permeability computation is thus questionable since it can only be used to inversely match laboratory permeability coefficients, which gave unrealistic permeability coefficients for the silicate mineral phase in this study, and since pores and different mineralogical phases cannot be separated due to resolution.

Permeability simulations based on 2D images from BIB-SEM showed that permeability coefficients derived from the clay mineral phase could be fitted to the laboratory measurements by assigning a tortuosity value of ≤ 1 . Such rather unrealistic tortuosity values (Soeder, 1988; Keller et al., 2011; Backeberg et al., 2017) also support the interpretation that fluid flow cannot be controlled by pores in the clay mineral phase alone.

Based on detailed characterizations of the pore size distribution, pore morphology and its connectivity in the calcite and clay mineral phases, arguments for or against the concept that the clay mineral phase exclusively provides flow pathways can be formulated.

Arguments for clay mineral phase to be in charge of fluid flow are:

(a) Identified pores in the calcite phase are bound to individual grains and therefore could potentially be isolated (Fig 3.5). Although calcite is the dominant mineral phase, the clay mineral phase finely disperses throughout the whole sample. Additionally, the clay mineral phase is mixed with other fine-grained silicate minerals, often enveloping the carbonate grains to a large extent (Fig 3.5). The silicate mineral phase in the 3D micro-CT reconstruction shows a generally good connectivity (Fig 3.4c).

(b) Shortest distance analyses of the FIB-SEM reconstruction indicate that pores in the clay mineral phase are closer to each other as compared to those in the calcite phase, which implicates higher possibility of these pores to be connected.

(c) The dominant slit-shaped pores in the clay mineral phase are likely to form a connected pore network considering the high elongation of these pores and highest visible porosity (1.06-1.46%). Besides, microfractures tend to occur at the interface between calcite and clay mineral phases and could potentially intensify the connectivity of the pore network (Fig 3.6f).

Arguments against clay mineral phase to be in charge of fluid flow are:

(a) From 3D micro-CT reconstruction, it can be seen that both silicate and carbonate phases are connected. The connectivity of the carbonate phase is significantly better due to the fact that approximately 80 vol.% of the rock is composed of carbonate. It is therefore assumptive to attribute flow exclusively to the silicate (13 vol.%) or clay mineral phase (6 vol.%) based on this argument.

(b) Inversely computed permeability coefficients from 3D micro-CT reconstruction for the silicate phase yield unrealistically high permeability coefficients. It should be noted that these would be even higher for the clay mineral phase only since the volumetric fraction of clays is even smaller.

(c) All pores appear to be isolated irrespective of the mineral phase based on the 3D FIB-SEM reconstruction. Although shortest distance analyses indicate pores to be closer to each other in the clay mineral phase, it is only assumptive to consider pores in the calcite phase isolated and pores in the clay mineral phase connected.

(d) Extrapolated porosities from mineralogical representative map 1, including calcite and clay mineral phases, are similar to the HP derived porosities. As the HP derived porosity measured on plugs represents an effective porosity, this is another supporting evidence that pores in the calcite phase are not isolated.

(e) BIB-SEM derived permeability coefficients for the clay mineral phase can only be matched to laboratory derived permeability coefficients with tortuosity ≤ 1 . Such tortuosity values appear unrealistic considering that pore throats could not be visualized (e.g., all pores are isolated based on FIB-SEM) and clays finely disperse throughout the rock making up only 6 vol.% of the bulk rock.

(f) Slit-shaped pores and microfractures are generally more susceptible to deformation than cylindrical pores. Under realistic conditions (burial depths of 250 – 1000 m for underground mining repositories), the proportion of slit-shaped pores and microcracks would likely be significantly lower than in this study. Additionally, the calcite phase is much more rigid than the clay mineral phase leading to better preservation potential of pores.

In order to provide more evidence to confirm the dominant flow pathways in the intact Cobourg

limestone, investigations on the accessibility of pores in calcite and clay mineral phases are particularly important. He pycnometry measurements on finely crushed rock sample (particle size smaller than 1 μm) and whole core sample could provide useful grain density information for comparison as most of the larger pores ($>1 \mu\text{m}$) occur in the calcite phase. Besides, woods metal injection experiments in combination with BIB-SEM could be an alternative way to directly image the transport pores in both mineral phases.

3.6 Conclusions

This contribution was an attempt to identify the mineral phases and associated microstructures relevant for fluid transport in the intact Cobourg limestone by using multiple imaging techniques covering a large scale (from nanometer to centimeter). The following conclusions can be reached:

(1) Based on the mineral composition analysis of BIB-SEM images, the Cobourg limestone can be characterized as a tight rock dominated by calcite grains of variable sizes (μm - cm) surrounded by idiomorphic or subhedral minerals (quartz, dolomite and pyrite) and meshy clay minerals. The silicate mineral phase in the 3D micro-CT reconstruction shows generally good connectivity.

(2) Qualitative and quantitative pore analyses indicate that calcite and clay mineral phases together contribute over 90% of the total pore areas in two BIB-SEM maps. The clay pores are relatively small and close to each other, dominated by slit-shaped pores and are interpreted as interparticle pores. The pores associated with calcite have larger pore size range and are distant from each other, equidimensional or elongated in shape and can mostly be considered as intraparticle pores.

(3) The calcite and clay mineral phases show typical different pore size distribution, which can be characterized by a power law relationship between pore area and normalized pore frequency. The power law exponent D values measured in clay mineral phase (2.50-2.59) are higher than those measured in the calcite phase (1.93-2.18).

(4) The discrepancy in porosity values measured by HP and BIB-SEM can be attributed to the sample heterogeneity and the lower resolution of BIB-SEM. The similarity between extrapolated porosities (down to 1 nm) and bulk porosities measured by HP indicates that valid porosity models can be reached by BIB-SEM imaging and interpretation towards smaller sized

pores, if a representative mineralogy is present in the studied map.

(5) Based on detailed characterizations of the pore size distribution, pore morphology and the uncertainty with respect to the connectivity of pores in the calcite and clay mineral phases, it cannot be concluded that the clay mineral phase exclusively provides pathways for flow, rather it is possible that microfractures enhance the flow as well as interconnected pore networks in the calcite phase. However, this has to be investigated in more detail.

4. PORE STRUCTURE AND SORPTION CAPACITY INVESTIGATIONS OF EDIACARAN AND LOWER SILURIAN GAS SHALES FROM THE UPPER YANGTZE PLATFORM, CHINA

Keywords: Ediacaran; Silurian; Sorption capacity; Pore structure; Mineralogy; Thermal maturity

ABSTRACT

The shale gas potential of Ediacaran and Lower Silurian shales from the Upper Yangtze platform is assessed in this study with a focus on the contributions of clay minerals and organic matter to sorption capacity. For this purpose, a multidisciplinary assessment was carried out using petrophysical, mineralogical, petrographic and geochemical methods.

In terms of TOC contents (4.2%), brittle mineral contents (68.6%) and maximum gas storage capacities (0.054 - 0.251 mmol/g), Ediacaran shales from this study show comparable properties to other producing shale gas systems although the thermal maturity is extremely high ($VR_r = 3.6\%$). When compared to lower Silurian shales from the same region, it is evident that (1) deeper maximum burial and (2) a lack of silica-associated preservation of the pores resulted in a relatively lower mesopore volume, higher micropore volume fraction and lower overall porosity (Ediacaran shales: 1.4 - 4.6%; Silurian shales: 6.2 - 7.4%). Gas production is therefore retarded by poor interconnectivity of the pore system, which was qualitatively demonstrated by comparing experimental gas uptake kinetics.

TOC content exhibits a prominent control on sorption capacity and micropore volume for both

shales. However, different contributions of clay minerals to sorption capacity were identified. This can partly be attributed to different clay types but is likely also related to burial-induced recrystallisation and different origins of illite. Additionally, it was shown that variations in sorption capacity due to incorrect estimates of clay mineral contribution are in the same range as variations due to differences in thermal maturity.

4.1 Introduction

Shale gas production in China progressed fast from 0.025 billion cubic meter (bcm) in 2012 to 10.88 bcm in 2018 but is still in an initial stage when compared to the United States (624.40 bcm in 2018) (Zhai et al., 2018; Wang et al., 2019; Dai et al., 2020). Therefore, the identification of additional shale gas prospects is currently prioritized in China (Nie et al., 2009; Han et al., 2013; Zou et al., 2014; Dang et al., 2016; Li et al., 2020). With respect to the economic potential of shale gas reservoirs, an accurate estimation of the maximum amount of gas stored (Gas in Place, GIP) is essential. Hence, investigations of gas storage estimates (porosity, excess sorption capacity) and their controlling properties (TOC content, clay content, moisture, thermal maturity, micropore volume, and accessibility) are of major interest.

To date, major commercial shale gas production in China is limited to the Upper Ordovician Wufeng and Lower Silurian Longmaxi Formations with an annual production of approximately 6 bcm in the Fuling gas field in 2017 (Chen et al., 2018). Additionally, a series of test wells were drilled on over-mature Cambrian and Ediacaran shales in the western Hubei province. The “Eyiye-1” test well, targeting the Cambrian Shuijingtuo Formation, produced $6.02 \times 10^4 \text{ m}^3$ gas per day in May 2017 (Chen et al., 2018). Retrieved cores from test wells “Zidi 1” and “Zidi 2” targeting the Ediacaran Doushantuo Formation revealed a total gas content of 0.337-1.666 m^3/t (0.015-0.073 mmol/g) at IUPAC standard conditions (273.15 K and 10^5 Pa) from canister desorption experiments on site (Li et al., 2019). Additionally, for the horizontally drilled “Eyangye-2HF” well, a gas production rate of up to $5.53 \times 10^4 \text{ m}^3/\text{day}$ was achieved from the Ediacaran Doushantuo Formation in 2018 (Wang et al., 2019). When compared to the average gas production rate ($12.87 \times 10^4 \text{ m}^3/\text{day}$) and total gas content (1.9-8.0 m^3/t or 0.083-0.352 mmol/g at IUPAC conditions) of the Wufeng and Longmaxi shale Formations (Zou et al., 2014; Zou et al., 2016), these test wells indicate good exploitation potential of Proterozoic shales in the Yangtze platform. Therefore, an appraisal of the economic potential of Ediacaran shale gas reservoirs is of particular importance. While numerous studies were performed to characterize storage properties of the Wufeng-Longmaxi shales (Yang et al., 2015; Wang et al., 2016; Yang

et al., 2016; Yang et al., 2017), only a few studies thus far focused on shales from the Ediacaran (Chen et al., 2016; Yang et al., 2020). These shales, though extremely high in thermal maturity (approximately 4.0% in equivalent vitrinite reflectance), are abundant in organic matter (TOC content of up to 8.0 wt.%) and widely distributed in the area of the Upper Yangtze platform with thicknesses of 200 to 900 m. The well-studied Silurian Longmaxi Shale in the Sichuan Basin has a lower thermal maturity (2.0-3.2%), smaller thickness from 100 to 500 m, exhibits high TOC contents (up to 8.3 wt.%) as well as porosity (3.4-8.2%) (Zou et al., 2014; Yang et al., 2015; Zhang et al., 2019).

Natural gas in shales can be stored in the free, dissolved and adsorbed state (Gasparik et al., 2014; Clarkson et al., 2016). Free gas is stored volumetrically in both pore and fracture space, whereas dissolved gas is the proportion of gas dissolved in formation water, liquid hydrocarbon or absorbed by solid kerogen (Zhang et al., 2012). The enrichment of gas on the surface of organic matter or minerals is referred to as adsorbed gas (Hildenbrand et al., 2006). In this study, the term “sorption” covers any state of gas storage except for the free state because a differentiation between adsorption and dissolution is currently not possible in the laboratory.

Several studies imply that gas stored in the sorbed phase can contribute up to 60% of the total gas storage capacity of shales (Lu et al., 1995; Rexer et al., 2013). Sorption capacity can therefore not be neglected in the evaluation of gas-in-place estimations. In this context, isothermal high-pressure methane sorption experiments are widely applied to assess the maximum sorption capacity of shales (Gensterblum et al., 2009; Rexer et al., 2013). Major controls on methane sorption capacity were identified as organic matter content and type, thermal maturity, clay mineral content and type, moisture, temperature and stress (Krooss et al., 2002; Chalmers and Bustin, 2007; Ross and Bustin, 2009; Ji et al., 2012; Zhang et al., 2012; Gasparik et al., 2014; Rexer et al., 2014; Merkel et al., 2015a; Yang et al., 2015; Yang et al., 2017; Gaus et al., 2021). In recent studies, positive correlations among sorption capacity, total organic carbon content (TOC) and micropore volume were found in organic-rich shales (Chalmers and Bustin, 2007; Ross and Bustin, 2009; Rexer et al., 2014; Yang et al., 2017). Ross and Bustin (2009) and Zhang et al. (2012) demonstrated that sorption capacities normalized to TOC increase with thermal maturity for Devonian–Mississippian shales from northern British Columbia and Mississippian Barnett shale from the Fort Worth Basin. This was attributed to an increased micropore volume in the organic matter or an increase of aromaticity of the kerogen residue. Gasparik et al. (2014) and Yang et al. (2015) further

observed a reverse trend at a vitrinite reflectance higher than 2.4% (dry gas stage) on Carboniferous shales from northern Germany and the Netherlands and on the Silurian Longmaxi shale from the Sichuan Basin. This could potentially result from an increasing carbonization of the organic matter and an associated destruction of micropores therein (Yang et al., 2015). With regard to the organic matter type, an increasing trend of sorption capacity following the order: type I < type II < type III organic matter was suggested (Clarkson and Bustin, 1996; Zhang et al., 2012), which could be interpreted as either an increasing trend of kerogen aromaticity (Zhang et al., 2012) or a higher amount of microporous vitrinite potentially providing more sorption sites (Chalmers and Bustin, 2007). Clay minerals generally feature relatively high specific surface area and the corresponding sorption capacities increase in the following order: illite < chlorite < kaolinite < I-S mixed layer < smectite (Ji et al., 2012). Moisture negatively influences sorption capacity by predominantly occupying polar sorption sites, which would otherwise be occupied by methane molecules (Gasparik et al., 2014; Merkel et al., 2015a; Yang et al., 2017).

The main objective of this study is to investigate gas storage capacities (porosity and sorption capacity) and controlling mechanisms of over-mature Ediacaran (Doushantuo and Liuchapo Formations) shales and to compare them with the widely characterized Lower Silurian (Longmaxi Formation) shales from the Upper Yangtze platform.

4.2 Geological setting

The shale samples studied originate from the Upper Yangtze platform (UYP), South China (Fig 4.1). The basement of the Yangtze platform is mainly composed of Neoproterozoic epimetamorphic rocks that were formed at 0.75-0.82 Ga (Charvet, 2013; Ren et al., 2013). A stable platform formed and consolidated after the Jinning orogenic movement (Wang and Tan, 1994). During the Ediacaran - Cambrian transition, a large-scale uplift (Tongwan movement) led to the creation of an unconformity (Tan et al., 2013; Wu et al., 2016; Fig 4.2). Inner shelf, outer shelf, slope and basin were distributed in sequence from northwest to southeast during that time interval (Fig 4.1; Guo et al., 2007). During the Late Ordovician to Early Silurian, the Yangtze platform gradually evolved into a foreland basin, accumulating large volumes of sediment. During this time interval, graptolite-rich shales were formed (Wufeng and Longmaxi Formations; Zhai et al., 2018). Since the end of the Middle Silurian, two major uplift and erosion events largely affected the upper Yangtze platform. The first event was caused by the late Caledonian movement and lasted for 120 Ma. Erosion thickness within the southeastern

Sichuan Basin is estimated to be between 100 and 200 m (Yuan et al., 2013). The second event is ongoing since the Late Cretaceous and causes another continuous uplift and erosion of the upper Yangtze platform. Deng et al. (2009) utilized apatite fission track dating to investigate the thermal uplift history of the Sichuan Basin from the Late Cretaceous onwards and estimated erosion thicknesses in southeastern Sichuan Basin to be approximately 3000 m.



Fig 4.1 Paleogeographic map of the Yangtze Platform during Ediacaran and Cambrian times (modified after Guo et al. 2007). Well ST-101 penetrated the Ediacaran Doushantuo and Liuchapo Formations at depth between 1000 and 1200 m and well XY-1 penetrated the Silurian Longmaxi Formation at depth between 430 and 620 m.

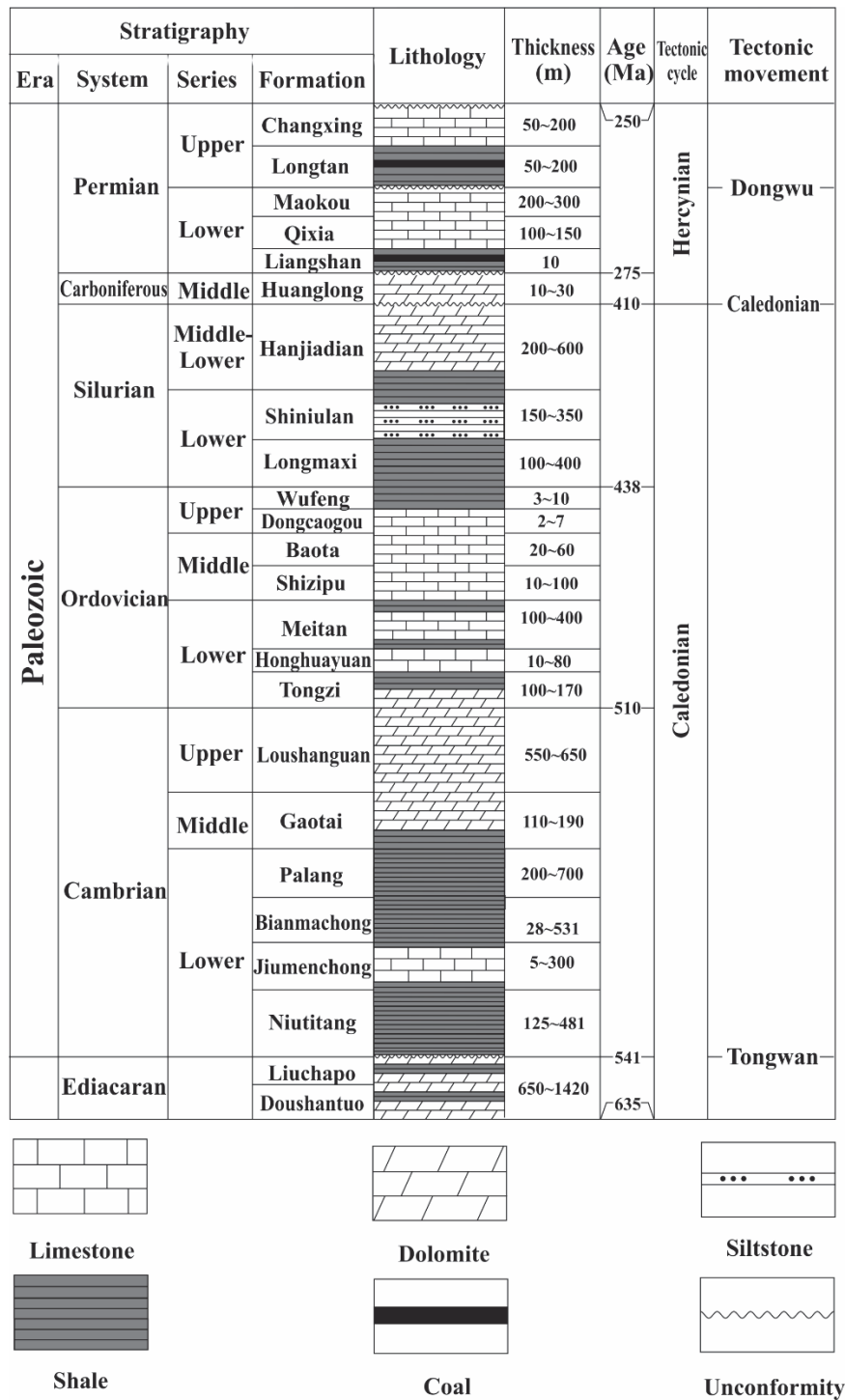


Fig 4.2 Litho- and chrono-stratigraphy of the Upper Yangtze Platform (modified after Zhai, 1987 and Zhang et al. 2019).

4.3 Samples and experiments

4.3.1 Samples

In this study, six Ediacaran shale samples were retrieved from cores taken from depth intervals

of 1047 to 1170 m during drilling operations of well ST-101 in the Songtao district of the Northeastern Guizhou Province (Table 4.1, Fig 4.1). Sample IDs are sorted according to the order of TOC content. Samples E2 and E5 belong to the lower Doushantuo Formation and E1, E3, E4 and E6 are part of the upper Liuchapo Formation (Fig 4.2). The study area is located on the slope belt between the carbonate platform and the basin (Fig 4.1). For comparison, six shale samples of the Lower Silurian Longmaxi Formation were collected from the Guizhou, Hubei and Sichuan Provinces. Samples S1 and S5 were cored from intervals of approximately 600 m during drilling operations of well XY-1 in the Northern Guizhou Province. S2-S4 and S6 were collected about 0.5 m below the surface to minimize the weathering effect.

Table 4.1 Characterization of Ediacaran and Silurian shale samples based on elemental composition (TOC, TS), solid bitumen reflectance (BR_r), equivalent vitrinite reflectance (VR_r) and mineral composition.

*1 Sample ID	Well/Outcrop location	Formation	Depth (m)	TOC (wt.%)	TS (wt.%)	*2BR _r / VR _r (%)	Mineral composition (wt.%)					
							Quartz	Feldspar	Clay+ Mica	Pyrite	Carbonate	Anatase +Rutile
E1	Well ST-101	Liuchapo	1047.3	1.0	1.4	3.8/3.6	77.6	7.0	14.0	1.4	0.0	-
E3	Well ST-101	Liuchapo	1057.2	3.6	1.3	3.7*/3.5	65.2	8.9	21.3	4.4	0.2	-
E6	Well ST-101	Liuchapo	1082.2	7.9	2.5	3.8*/3.6	57.6	13.3	20.4	3.7	5.0	-
E4	Well ST-101	Liuchapo	1104.2	3.7	3.4	3.6*/3.5	32.8	14.9	42.1	3.7	6.6	-
E5	Well ST-101	Doushantuo	1160.8	6.1	5.6	3.8*/3.7	23.5	21.9	39.6	9.1	5.9	-
E2	Well ST-101	Doushantuo	1170.0	2.9	2.7	3.9*/3.7	62.3	8.0	25.8	3.0	0.9	-
S5	Well XY-1	Longmaxi	597.0	5.2	1.1	2.9*/2.9	52.1	8.1	34.1	2.0	3.7	0.0
S1	Well XY-1	Longmaxi	612.0	1.2	0.9	3.0/3.0	24.2	9.0	55.9	1.7	8.3	0.9
S2	Hubei	Longmaxi	0	2.5	0.1	2.1*/2.1	55.1	15.5	28.3	0.0	0.0	1.7
S4	Chongqing	Longmaxi	0	4.0	0.2	2.0/2.1	70.6	5.1	23.4	0.0	0.0	0.9
S3	Chongqing	Longmaxi	0	3.2	1.0	2.8/2.8	28.7	10.6	24.3	1.0	35.5	0.0
S6	Chongqing	Longmaxi	0	6.6	0.5	2.8/2.8	62.3	10.6	26.2	0.0	0.0	0.9

*1 Sample IDs are sorted according to the order of TOC content.

*2 Solid bitumen reflectances were taken from Zhang et al. (2019) and converted to vitrinite reflectances by using Eq. 1 after Mählmann and Frey (2012).

4.3.2 Microscopy

Sample sections were cut perpendicular to bedding and embedded in epoxy resins. The upper surfaces of the epoxy resins were ground flat and the exposed sample surfaces were

subsequently polished. Solid bitumen reflectance measurements were performed on a Zeiss Axio Imager microscope equipped with a tungsten-halogen lamp (12 V, 100 W), a 50×/0.85 Epiplan-NEOFLUAR oil immersion objective and a 546 nm filter. Cubic zirconium (3.125% in reflectance) was selected as the mineral standard for calibration. Since pre-Silurian shales generally do not contain vitrinite, solid bitumen was used as a substitute. Solid bitumen reflectance was converted into vitrinite reflectance according to Eq. 1 after Mählmann and Frey (2012). Details of the measurement procedures and guidelines are found in Taylor et al. (1998) and Littke et al. (2012).

$$BR_r = -0.519 + 1.341 * VR_r - 0.0977 * (VR_r)^2 + 0.0151 * (VR_r)^3 \quad (\text{Eq. 1})$$

Here, VR_r (%) and BR_r (%) represent the equivalent vitrinite and solid bitumen reflectance.

4.3.3 Elemental analysis

The total organic carbon (TOC) and total inorganic carbon (TIC) were measured by a liquiTOC II analyzer. This apparatus continuously records the CO₂ release in a phased heating process. Based on the theory that TOC and TIC are released at different temperature ranges, organic and inorganic carbon can be separately detected in a single analytical run. Total sulfur (TS) content was measured by a Leco S200 analyzer with a detection limit of 0.002%.

4.3.4 X-ray diffraction analysis (XRD)

X-ray powder diffraction (XRD) was used for quantification of the mineral composition. A particle fraction greater than 400 μm was gently crushed in a mortar and 0.2 g/g of Baikowski α-Al₂O₃ were added as an internal standard serving as quantification control. To avoid excess strain, heat damage and mineral dissolution, a McCrone micronizing mill was used for 15 min with ethanol as coolant. The suspension was air-dried and homogenized in a mortar before the powder bed was prepared via a top-fill procedure. XRD powder patterns were measured on a Bruker D8 using Cu Kα radiation (40 kV, 40 mA). Mineral quantification was performed by means of Rietveld refinement using the BGMN based software Profex (Doebelin and Kleeberg, 2015). For clay mineral quantification, customized clay mineral structures were used (Ufer et al., 2008; Ufer and Kleeberg, 2015).

In addition to the bulk mineralogical analysis, oriented clay samples were prepared for four selected samples (E4, E5, S1 and S5). Before the clay fraction was separated through sedimentation, carbonates and organic matter were removed. Quantitative carbonate removal

was achieved by hydrochloric acid treatment. The pH was adjusted to approximately 4.8 by a buffer mixture of Na-acetate and acetic acid. Organic matter was oxidized at alkaline conditions (pH of 9.5) at room temperature using sodium hypochlorite as suggested by Mikutta et al. (2005). Prior to size fractionation, excess salts were removed by extensive flushing to reduce the ionic strength of the suspension and to ensure unhindered settling of the clay fraction in the Atterberg cylinders. After enrichment of the clay-size fraction, oriented clay samples were produced from suspensions using distilled water. For qualitative identification of the particular clay mineral, oriented clay samples of (i) pure samples, (ii) samples treated with glycerol and (iii) heated samples were measured on a Bruker D8 using Cu K α radiation (40 kV, 40 mA), respectively.

4.3.5 Water immersion porosimetry (WIP)

Water immersion porosimetry (WIP) based on Archimedes' principle was utilized to obtain information on the pore volume of irregular-shaped samples. The weight difference of the dry sample (W_{dry}) and the fully water-saturated sample in air (W_{sat}), together with the water density, allow for determination of the pore volume (V_{pore} ; Eq. 2). The bulk volume (V_{bulk}) is calculated from the weight difference of the water-saturated sample in air (W_{sat}) and the water-saturated sample immersed in water (W_i ; Eq. 3). The porosity equals the ratio of pore to bulk volume. A detailed discussion on the operation of WIP is given in Kuila et al. (2014) and Hu et al. (2020b).

$$V_{pore} = \frac{W_{sat} - W_{dry}}{\rho_w} \quad (\text{Eq. 2})$$

$$V_{bulk} = \frac{W_{sat} - W_i}{\rho_w} \quad (\text{Eq. 3})$$

4.3.6 High-pressure methane sorption measurements

To remove moisture, crushed samples (63-354 μm) were first dried in a vacuum oven at 378.15 K until weight equilibration for at least 24 h. High pressure methane sorption measurements were then conducted in a manometric setup at 318.15 K and pressures up to 20 MPa. In this apparatus, the reference cell volume consists of the dead volume of the capillary volume among valve 4 (V4), valve 5 (V5) and the pressure transducer (Fig 4.3). The volumes of both sample and reference cells were pre-calibrated and a leak test was performed before each sorption measurement. Leak tests were conducted with helium at 20 MPa and a leak rate <500 Pa/h was achieved prior to measuring. Hereafter, the void volume of the filled sample cell was calibrated

by helium expansion. Similar to the procedure of void volume calibration, the methane sorption measurement was programmed by sequentially transferring methane molecules from the reference cell into the sample cell until the final equilibrated pressure was reached. In the measurement, a syringe pump (Teledyne ISCO 260D) was programmed to stepwise increase the gas pressure in the reference cell.

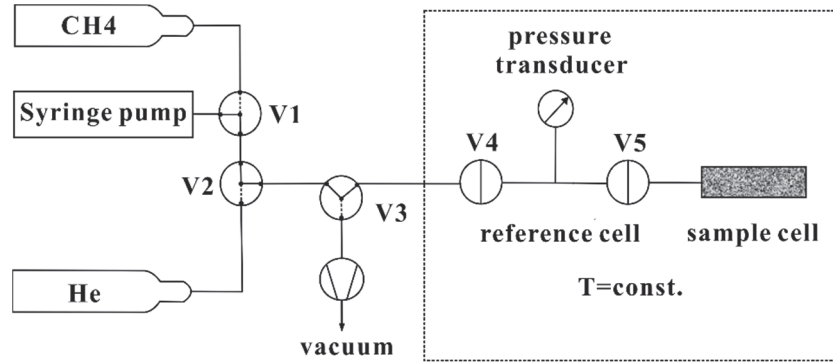


Fig 4.3 High-pressure sorption setup (V1-V5 are either two-port or three-port valves and the syringe pump (Teledyne ISCO 260D) was programmed to stepwise increase the gas pressure in the reference cell).

The excess sorption amount (n_{excess}) is equivalent to the difference between the total transferred gas amount (n_{trans}) from the reference cell to the sample cell and the amount of “free” gas occupying the void volume (V_{void}) of the sample cell.

$$n_{excess}(P, T) = n_{trans}(P, T) - \rho_g(P, T) \cdot V_{void} \quad (\text{Eq. 4})$$

Here, the methane density (ρ_g ; kg/m³) as a function of pressure P (Pa) and temperature T (K) was calculated by the GERG equation of state (EOS; Kunz and Wagner, 2012).

Considering potential systematic errors of temperature and pressure recordings, for example, due to the impurity of methane or the interaction between methane molecules and the internal surface of the apparatus, a blank measurement with methane is particularly important to generate reproducible isotherms when different setups are used (Gasparik et al., 2014). Therefore, stainless steel balls of known volume were used instead of the actual shale samples. The derived “blank” isotherm was subtracted from measured excess sorption isotherms of the shale samples. The “blank-corrected” isotherms could be described by a Langmuir-type function (Eq. 5),

$$n_{excess}(P, T) = n_{\infty} \frac{P}{P+P_L(T)} \left(1 - \frac{\rho_g(P, T)}{\rho_a}\right) \quad (\text{Eq. 5})$$

Here, $n_{excess}(P, T)$ (mmol/g) represents the “blank-corrected” excess amount of methane at pressure P (Pa) and temperature T (K). n_{∞} (mmol/g) and P_L (Pa) denote the Langmuir volume and Langmuir pressure, respectively. The Langmuir volume is the maximum amount of sorbed gas when the “Langmuir monolayer” is fully occupied. The Langmuir pressure corresponds to the pressure at which half of the Langmuir volume is reached. ρ_a (kg/m³) and $\rho_g(P, T)$ (kg/m³) are the densities of the sorbed and free gas at P and T . In this study, the sorbed phase density is kept constant at 423 kg/m³ (liquid methane density at 10⁵ Pa and 111.65 K) to reduce the amount of adjustable parameters (Dreisbach et al., 1999).

Additionally, two dry Ediacaran samples (E4 and E6) were moisturized in a desiccator with a super-saturated K₂SO₄ solution to ensure 97% relative humidity (RH) at 293.15 K. After the sample weights remained constant, sorption measurements were repeated on these moisture-equilibrated samples.

Based on the experimental data, the in-situ excess sorption capacity at specific temperatures can be estimated (Eq. 5). The free gas capacity can also be calculated with porosity, bulk rock density and in-situ free gas density (Eq. 6). Therefore, the GIP amount equivalent to the sum of free gas and excess sorption capacities can be estimated by setting of the following parameters (Eq. 7).

$$G_f = \frac{\phi \rho_g(P, T)}{M \rho_{bulk}} \quad (\text{Eq. 6})$$

$$GIP = G_{ex} + G_f = n_{\infty} \frac{P}{P+P_L(T)} \left(1 - \frac{\rho_g(P, T)}{\rho_a}\right) + \frac{\phi \rho_g(P, T)}{M \rho_{bulk}} \quad (\text{Eq. 7})$$

Here, GIP (mmol/g), G_{ex} (mmol/g) and G_f (mmol/g) represent the total amount of gas storage, excess sorption storage capacity and free gas storage capacity, respectively. ϕ (-), ρ_{bulk} (kg/m³) and M (g/mol) denote the porosity and bulk density of the shale as well as molar mass of methane, respectively.

4.3.7 Low-pressure nitrogen and carbon dioxide adsorption measurements

These measurements were performed on a dry 200 – 400 μm particle-size fraction of the bulk sample material using the manometric setup Gemini VII 2390t apparatus (Micromeritics Instrument Corporation, Norcross, GA, USA). Firstly, samples were evacuated at 378 K for at

least 16 h in a VacPrep 061 to remove liquids occupying the pore space (Micromeritics Instrument Corporation, Norcross, GA, USA). To obtain N₂ isotherms, the amounts of N₂ adsorbed at 93 discrete pressure points between 0.001 and 0.995 p/p⁰ were measured at 77 K in a cryogenic nitrogen bath. The saturation pressure (p⁰) was determined separately for each pressure point and operational equilibrium was assumed at a pressure drop of less than 0.01% over a time interval of 30 s. To assess the micropore volume, CO₂ sorption isotherm measurements were performed at 273 K at 25 discrete pressure steps between 0.001 and 0.036 p/p⁰. The highest measurable partial pressure was restricted to 0.036 due to the high saturation pressure (3.49 MPa) of carbon dioxide at operational temperature. An equilibrium criterion of 10 s was applied assigning equilibrium when the pressure fluctuates less than 0.01% over the given time.

The pore structure was characterized by traditional physisorption theories including Brunauer-Emmett-Teller (BET) theory for specific surface area quantification, Barrett-Joyner-Halenda (BJH) theory for pore volume distribution calculation, Gurvich's rule (GV) for total pore volume assessment and Dubinin-Astakhov theory (DA) for micropore volume determination (Gurvich, 1915; Brunauer et al., 1938; Barrett et al., 1951; Dubinin and Astakhov, 1971). Detailed explanation of the fundamentals of the individual theories can be found in Rouquerol et al. (2013) and references therein.

4.4 Results

4.4.1 Mineral composition

XRD analysis results of Ediacaran and Silurian shales are listed in Table 4.1. For both shales, quartz is the dominating phase ranging from 23.5 to 77.6 wt.%, followed by clay minerals ranging from 14.0 to 55.9 wt.% and feldspars ranging from 5.1 to 21.9 wt.%. Minor contributions (<10 wt.% on average) of carbonates and pyrite as well as traces of anatase and rutile (heavy minerals) were detected as well. The average brittle mineral content (quartz + feldspar + carbonates) of Ediacaran shales (68.6 wt.%) is higher than that of Silurian shales (66.5 wt.%), while the average clay content of Ediacaran shales (27.2 wt.%) is lower than that of Silurian shales (32.0 wt.%). Based on the texture preparations, clay types were qualitatively distinguished (appendix 1). Whereas illite/muscovite was the only identified clay type in the Ediacaran shales, illite/muscovite and chlorite were distinguished for the Silurian shales.

4.4.2 TOC, TS and thermal maturity

TOC contents of the Ediacaran and Silurian shales vary from 1.0 to 7.9 wt.% (4.2 wt.% on average) and 1.2 to 6.6 wt.% (3.8 wt.% on average), respectively (Table 4.1). TS contents of the Ediacaran shales (1.3-5.6 wt.%) are generally higher than those of the Silurian shales (0.1-1.1 wt.%). The equivalent vitrinite reflectances of Ediacaran shales range between 3.5% and 3.7% (dry gas stage; Table 4.1). Values of Longmaxi shales are lower and range between 2.1% and 3.0% (dry gas stage).

Due to the difference of dissolved sulfate concentration between marine and fresh water environments, the TOC/TS ratio is a useful parameter to distinguish organic-rich fresh water from marine sediments (Berner and Raiswell, 1984). Considering the loss of organic matter during maturation, the TS content was plotted against $2 \times$ TOC content (Uffmann et al. 2012; Fig 4.4). Most of the shale samples distribute along the “normal marine” line, while three Silurian shales (S2, S4 and S6) display a significantly lower TS/TOC ratio. These samples were taken from outcrops and therefore likely subjected to weathering, which likely led to relative enrichment of TOC when compared to TS (Littke et al., 1991).

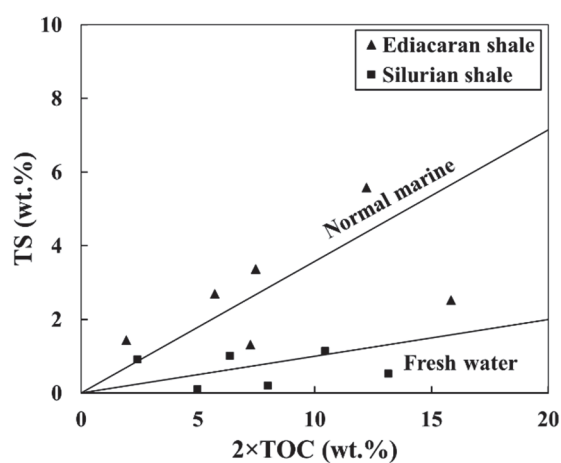


Fig 4.4 Relationship between TS and TOC content (multiplied by 2) for Ediacaran and Silurian shale samples (“normal marine” line after Berner and Raiswell 1984).

4.4.3 Pressure equilibration and uptake kinetics

Pressure equilibration is a prerequisite to study storage properties in shales by gas expansion methods such as helium pycnometry and high-pressure methane sorption. Therefore, it was closely monitored during this study (Fig 4.5). Equilibration times for all samples with similar particle sizes (between 64 and 354 μm) are exemplarily shown for equilibrated methane

pressures of ~ 0.5 MPa (Fig 4.5a & b) and range between 49 to 292 min and 20 to 150 min for the Ediacaran and Silurian shales, respectively. Helium uptakes were generally faster than methane uptakes as is exemplarily shown for sample E1 at approximately equivalent mean gas pressures of 0.5 MPa (Fig 4.5c) and equilibration times decrease with increasing mean gas pressure which is exemplarily shown for sample E2 with methane pressures from 0.7 to 20.5 MPa (Fig 4.5d).

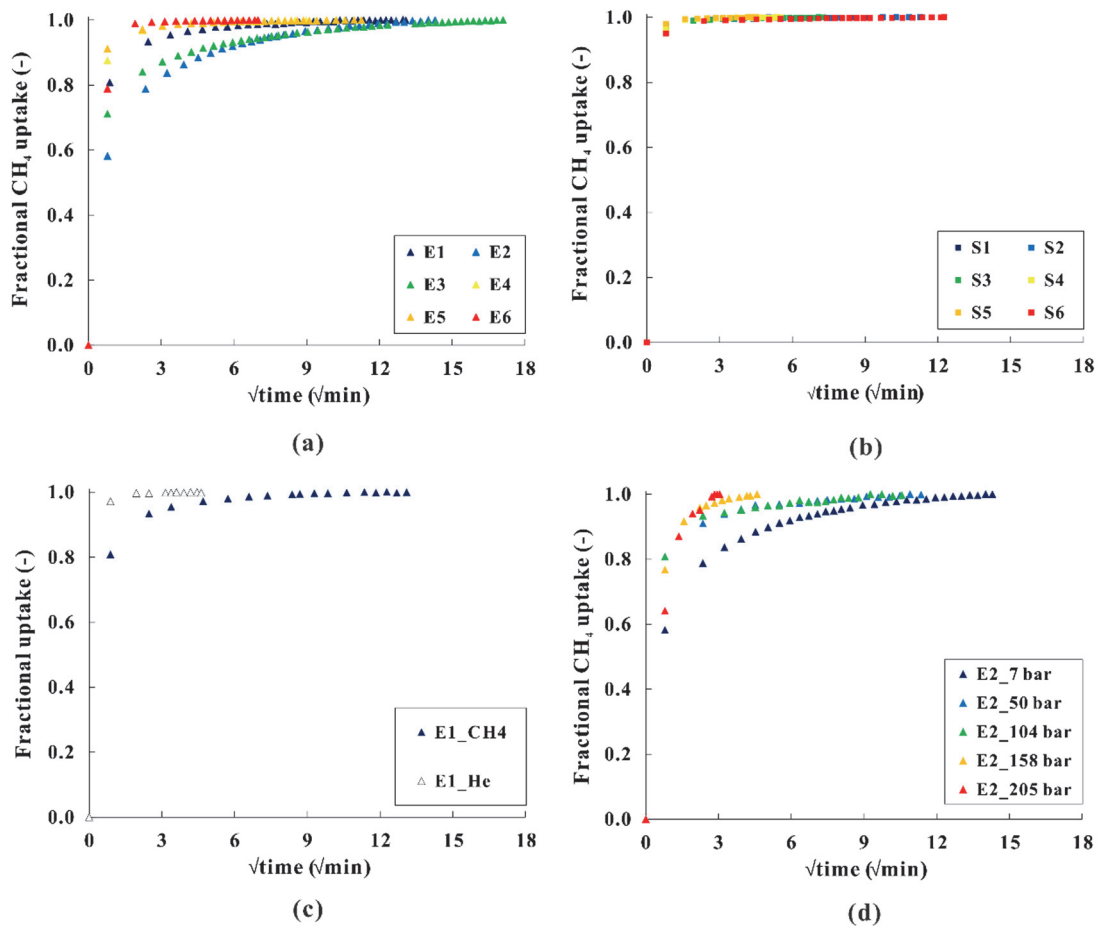


Fig 4.5 Fractional uptake versus square root of time for (a) Ediacaran and (b) Silurian shales at about 0.5 MPa methane pressure, (c) helium and methane uptake rates of sample E1 at about 0.5 MPa gas pressure and (d) uptake rates at varying methane pressures from 0.7 to 20.5 MPa for sample E2.

4.4.4 High-pressure methane sorption

Methane sorption isotherms at dry and moist conditions were measured at 318.15 K (approximately equivalent to current in-situ temperatures of the Ediacaran samples) (Fig 4.6). For all samples measured in the dry state, experimental results demonstrate a wide variation in the maximum excess methane sorption capacity (0.016 - 0.135 mmol/g). All excess sorption

isotherms obtained at dry conditions are similar in shape and exhibit maxima between 9 and 14 MPa methane pressure. Therefore, Eq. 5 was used to fit the experimental results. Fitted Langmuir pressures and Langmuir volumes normalized to either sample weight or sample weight and TOC content are listed in Table 4.2. Langmuir pressures of the Silurian shales, ranging from 3.12 to 8.42 MPa (5.63 MPa on average), are higher than the Ediacaran shales with values ranging from 2.05 to 5.19 MPa (3.56 MPa on average). Langmuir volumes normalized to sample weight range between 0.02 and 0.19 mmol/g (0.10 mmol/g on average) and 0.08 - 0.21 mmol/g (0.13 mmol/g on average) for the Ediacaran and Silurian shales, respectively. A positive correlation between Langmuir volumes and TOC contents was observed for both shales (Fig 4.7). The Ediacaran samples E4 and E6 were additionally moisturized at a relative humidity of 97%. Equivalent water contents were 2.1 and 3.1 wt.% and Langmuir volumes decreased by 32 and 48%, respectively (Table 4.2). The reduction of excess sorption capacity at 10 MPa is between 61 and 64%.

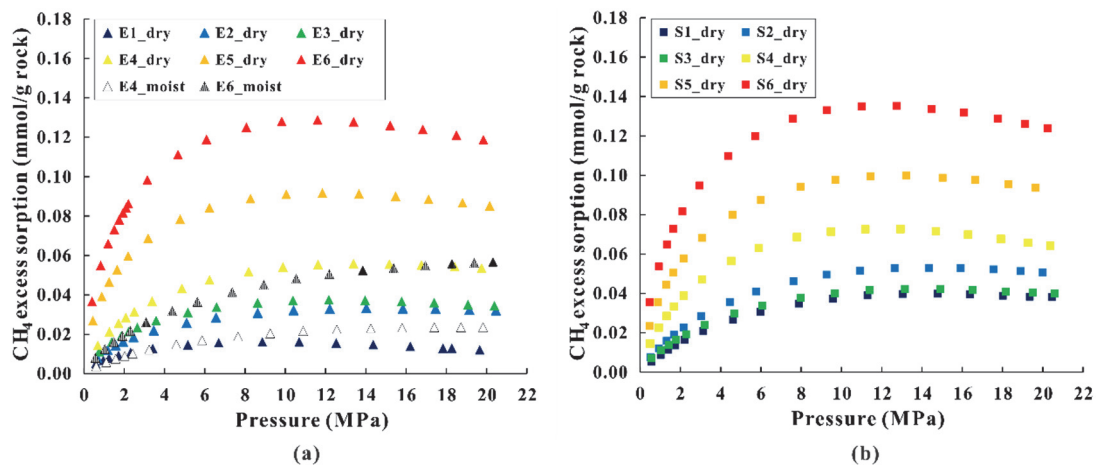


Fig 4.6 Methane sorption isotherms at 318.15 K for (a) the Ediacaran shales at dry and moist conditions (97% relative humidity) and (b) the Silurian shales at dry conditions.

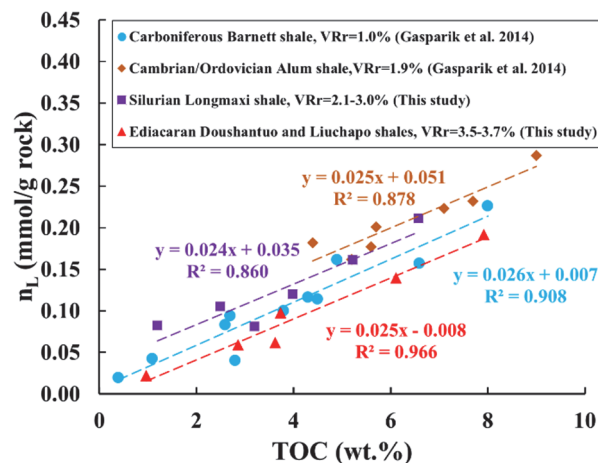


Fig 4.7 Comparison of Langmuir volumes and TOC contents for samples from the Ediacaran (Doushantuo and Liuchapo shales), Silurian (Longmaxi shale), Carboniferous (Barnett shale) and Cambrian/Ordovician (Alum shale).

Table 4.2 Excess sorption capacities at 10 MPa (n_{ex}^{10MPa}), Langmuir volumes (n_{∞}) normalized to sample weight or sample weight and TOC content as well as Langmuir pressure (P_L) for Ediacaran (E1-E6) and Silurian (S1-S6) shales at dry and moist (97% relative humidity) conditions.

Sample ID	Water		Methane excess sorption (45°C)			
	content (wt.%)	TOC (%)	n_{ex}^{10MPa}	n_{∞}	n_{∞}	P_L (MPa)
			(mmol/g)	(mmol/g)	(mmol/g TOC)	
E1	0	1.0	0.016	0.022	2.253	2.05
E2	0	2.9	0.032	0.059	2.065	5.19
E3	0	3.6	0.038	0.062	1.708	4.02
E4	0	3.7	0.055	0.098	2.702	4.97
	2.14	3.7	0.021	0.051	1.439	9.84
E5	0	6.1	0.093	0.139	2.279	2.65
E6	0	7.9	0.132	0.192	2.423	2.44
	3.08	7.9	0.048	0.131	1.709	12.37
S1	0	1.2	0.038	0.082	6.850	8.42
S2	0	2.5	0.051	0.105	4.221	7.49
S3	0	3.2	0.041	0.081	2.548	6.93
S4	0	4.0	0.073	0.120	3.000	4.18
S5	0	5.2	0.100	0.161	3.093	3.65
S6	0	6.6	0.137	0.211	3.210	3.12

4.4.5 Low-pressure nitrogen adsorption

According to the IUPAC classification, N_2 adsorption isotherms of all samples can be described by a Type IV isotherm that is characteristic of a hysteresis loop (Thommes et al., 2015; Fig 4.8a & b). The preliminary phase of fast adsorption accumulation with pressure results from micropore filling followed by monolayer-multilayer adsorption of N_2 . As the pressure decreases, the desorption branch falls abruptly forming a hysteresis loop with the adsorption branch. The hysteresis loops of the studied shales belong to Types H3 and H2 (Seemann et al., 2017). The closure points of hysteresis loops in Type IV isotherms generally arise at a lower relative pressure of 0.42, which is mainly dependent on the adsorptive and the pore structure (Thommes et al., 2015; Yang et al., 2015; Seemann et al., 2017). However, closure points of most of the samples occur at relative pressures lower than 0.42. This low-pressure hysteresis (LPH) indicates incomplete equilibrium and can be attributed to slow diffusion in ultra-

micropore space. BET specific surface areas of the Ediacaran and Silurian samples range from 1.19 to 24.32 m²/g (10.20 m²/g on average) and 5.45 to 24.86 m²/g (17.27 m²/g on average), respectively. No correlation was observed between BET specific surface area and TOC content (Fig 4.9a).

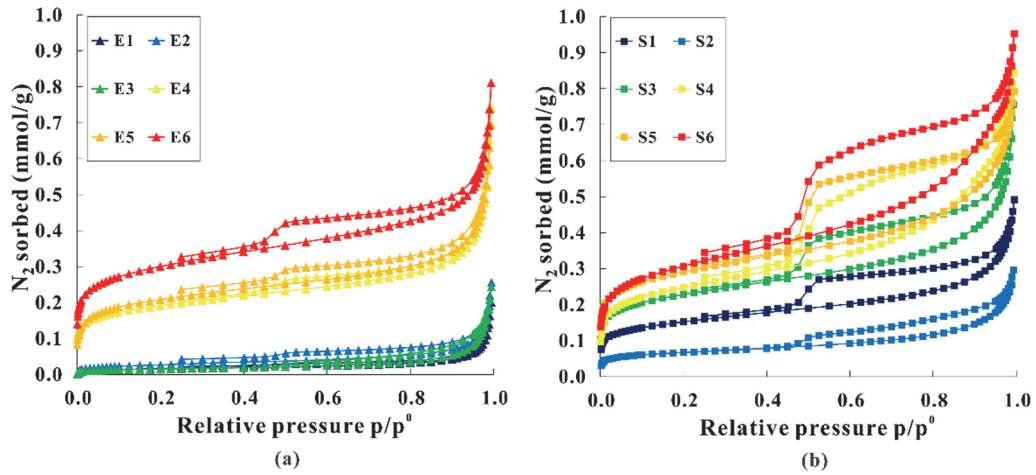


Fig 4.8 Nitrogen adsorption and desorption isotherms of the Ediacaran (a) and Silurian (b) shales at 77 K.

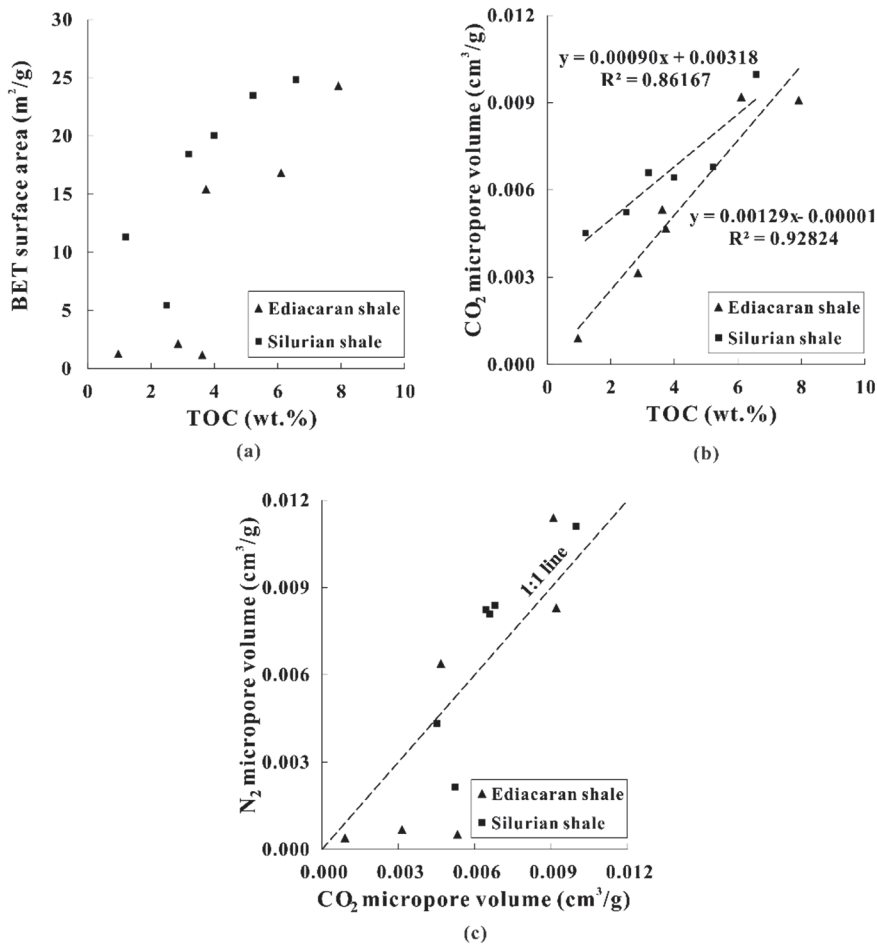


Fig 4.9 Relationships between TOC content and BET surface area (a), TOC content and CO₂ micropore

volume (b) and CO₂ micropore volume and N₂ micropore volume (c).

4.4.6 Porosity and pore size distribution

WIP porosity values of the Ediacaran shales range from 1.4 to 4.6% (3.5% on average; Table 4.3). WIP porosities of the Silurian shales (excluding weathered samples S2, S4 and S6) are higher, ranging from 6.2 to 7.4% (6.8% on average). Correspondingly, the average specific pore volumes of Ediacaran and Silurian shales are 0.0135 and 0.0271 cm³/g, respectively.

Table 4.3 Porosity and pore structure analysis results from N₂ and CO₂ adsorption measurements on Ediacaran (E1-E6) and Silurian (S1-S6) shale samples.

Sample ID	Porosity (%)	N ₂ BET specific surface area (m ² /g)	CO ₂ micropore surface area (m ² /g)	CO ₂ micropore volume (cm ³ /g)	N ₂ mesopore volume (cm ³ /g)	Mesopore/micropore volume ratio	Total pore volume (cm ³ /g)
E1	1.4	1.28	2.53	0.0009	0.0025	2.77	0.0053
E2	3.8	2.16	8.75	0.0031	0.0037	1.17	0.0147
E3	4.6	1.19	12.64	0.0053	0.0037	0.70	0.0183
E4	3.0	15.43	12.36	0.0047	0.0100	2.15	0.0114
E5	3.7	16.83	22.41	0.0092	0.0101	1.09	0.0137
E6	4.4	24.32	23.17	0.0091	0.0118	1.30	0.0175
Mean	3.5	10.20	13.64	0.0054	0.0070	1.53	0.0135
S1	6.7	11.33	10.90	0.0045	0.0090	1.99	0.0265
S2	14.8	5.45	14.10	0.0052	0.0058	1.11	0.0658
S3	7.4	18.45	15.98	0.0066	0.0129	1.96	0.0295
S4	10.0	20.06	17.07	0.0064	0.0180	2.80	0.0430
S5	6.2	23.50	17.25	0.0068	0.0154	2.26	0.0253
S6	9.6	24.86	23.90	0.0100	0.0200	2.01	0.0418
Mean	6.8*	17.27	16.53	0.0066	0.0135	2.02	0.0271*

* The value of average porosity or average total pore volume is calculated from samples S1, S3 and S5 considering the weathering effect to the other outcrop samples.

Interpretation of N₂ adsorption isotherms using the BJH theory shows that the pore sizes range between 1.6 and 153 nm for all samples (Fig 4.10a & b). The mesopore volume of the Silurian shales, varying between 0.0058 and 0.0200 cm³/g (0.0135 cm³/g on average), is approximately two times higher than that of the Ediacaran shales with values ranging from 0.0025 to 0.0118 cm³/g (0.0070 cm³/g on average; Table 4.3). Based on the interpretation of CO₂ adsorption branch data using the DA theory, the derived micropore volumes of the Ediacaran shales (0.0009-0.0092 cm³/g, 0.0054 cm³/g on average) are in the same range as those of the Silurian shales (0.0045-0.0100 cm³/g, 0.0066 cm³/g on average). A positive correlation between CO₂

micropore volume and TOC content was observed for both shales (Fig 4.9b). Normalized to the specific total pore volume determined by WIP, micro- and mesopores of the Ediacaran shales account for 37.9% (16.9-67.0%) and 53.5% (20.2-88.1%) on average, respectively. Excluding the weathered samples (S2, S4 and S6), the average proportions of micro- and mesopores for Silurian samples are 22.1% (17.1-26.9%) and 46.2% (34.0-60.8%), respectively.

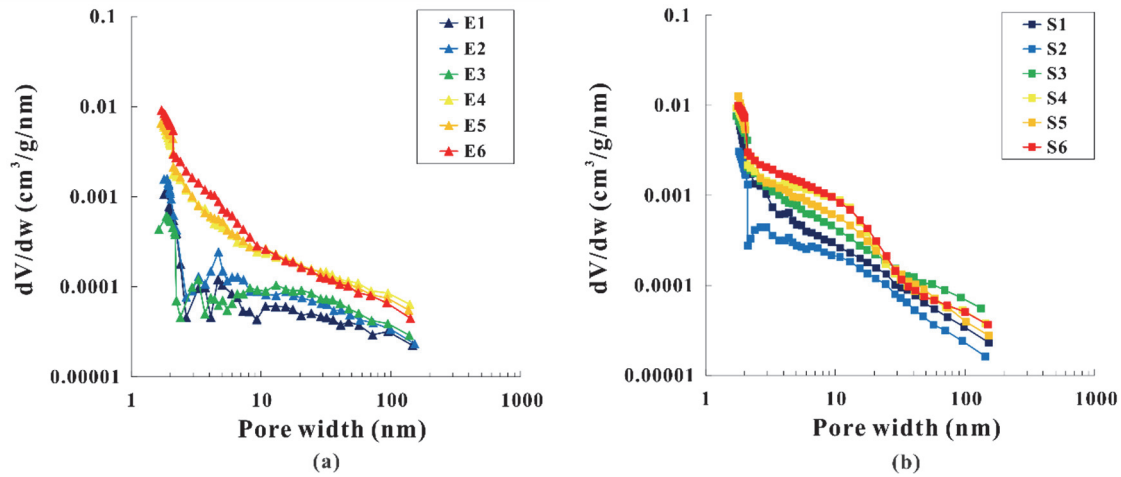


Fig 4.10 Differential pore volume distribution (dV/dw) of Ediacaran (a) and Silurian (b) shales.

4.5 Discussion

4.5.1 Effect of organic matter and clay minerals on methane sorption capacity

Data collected in this study suggest that sorption capacity is equally important as a storage mechanism for the Ediacaran and Silurian samples (Δ average Langmuir volume = 0.03 mmol/g, Table 4.2). A strong positive correlation between Langmuir volumes and TOC contents for both sample sets indicates a first-order influence of TOC content on sorption capacity. The use of low-pressure CO₂ adsorption measurements in this study additionally confirmed that sorption predominantly occurs within organic matter micropores for both shales (positive correlation between CO₂ micropore volume and TOC in Fig 4.9b). Similar results were also reported by Gasparik et al. (2014). From both figures (Fig 4.7 & 4.9b) it is also evident that Langmuir and micropore volumes are exclusively related to the TOC content in the Ediacaran shale (linear regression to 0 wt.% TOC). For the Silurian shale, on the other hand, the linear regression yields 0.035 mmol/g rock (Fig 4.7) and 0.0032 cm³/g (Fig 4.9b) at 0 wt.% TOC, indicating that not only TOC content but also inorganic minerals contain micropore volume for sorptive storage. This was additionally tested by a linear combination approach in the following form:

$$n_{\infty} = n_{TOC}w_{TOC} + n_{clay}w_{clay} + n_{rigid}w_{rigid} \quad (\text{Eq. 8})$$

Here, n_{∞} (mmol/g) is the Langmuir volume obtained from experimental data, n_{TOC} , n_{clay} , n_{rigid} (mmol/g) represent the fitted individual Langmuir volumes of organic matter, clay minerals and rigid minerals, respectively. Correspondingly, w_{TOC} , w_{clay} and w_{rigid} denote the experimentally determined mass fractions of the rock constituents. It should be noted that this approach was applied simultaneously to the entire sample set and therefore provides a single value for n_{TOC} , n_{clay} and n_{rigid} that characterizes the entire sample set.

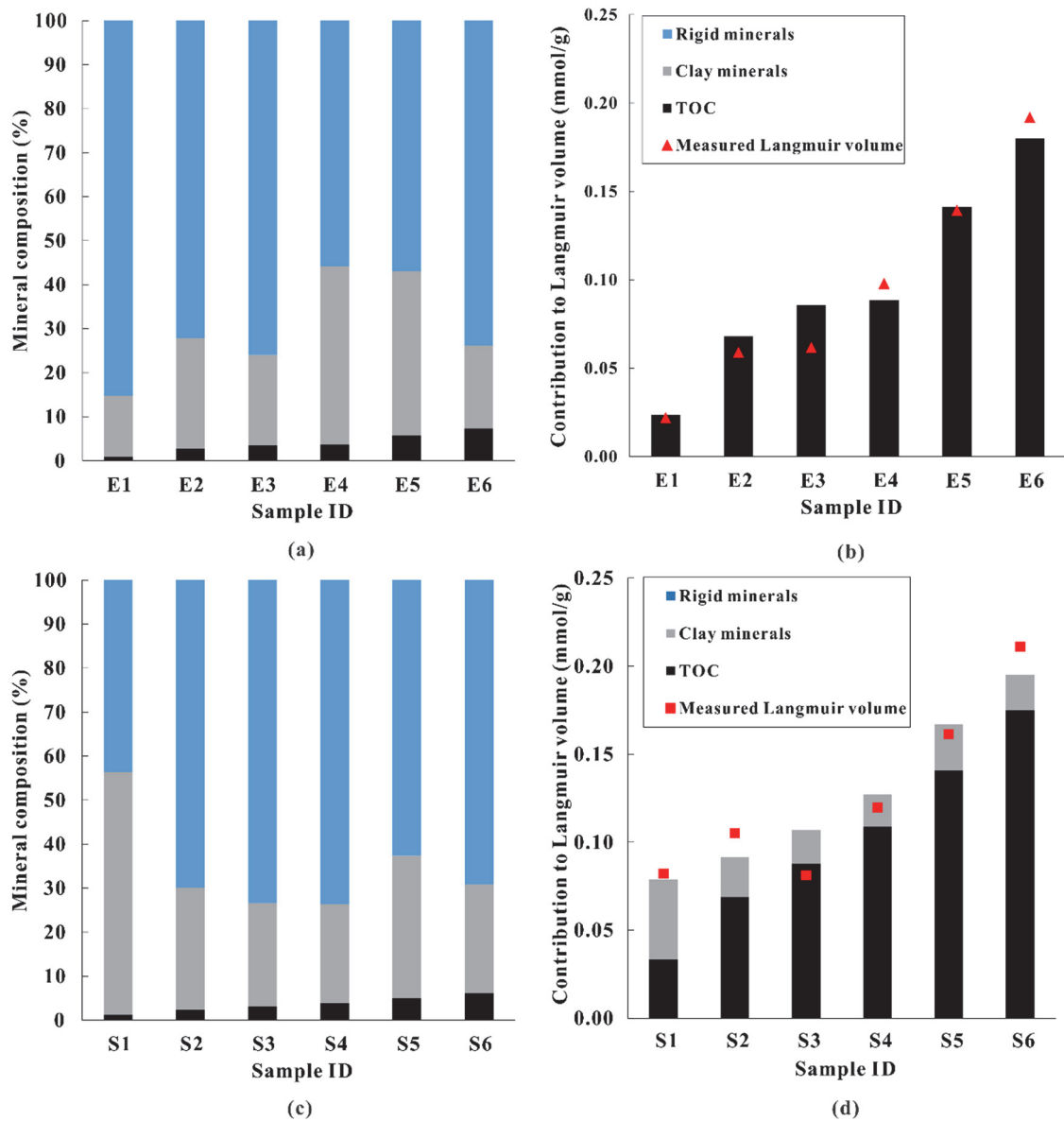


Fig 4.11 Mineral composition and respective contribution to Langmuir volume for the Ediacaran (a, b) and Silurian (c, d) shales (blue, grey and black colors represent rigid minerals, clay minerals and organic matter, respectively).

Results for the Ediacaran samples indicate a contribution of 2.452 mmol/g for organic matter and 0 mmol/g for clay minerals as well as rigid minerals (Fig 4.11a & b). For the Silurian shales, on the other hand, estimated Langmuir volumes were 0, 0.082 and 2.834 mmol/g for rigid minerals, clay minerals and organic matter, respectively (Fig 4.11c & d). Accordingly, the average contribution of clay minerals to the total Langmuir volume is $\approx 23\%$ for the Silurian shales and 0% for the Ediacaran shales, although both shales have similar clay contents. Ji et al. (2012) suggested that sorption capacities for different clay mineral types vary strongly from 0.079 to 0.380 mmol/g and increase in the order of illite < chlorite < kaolinite < I-S mixed layer < smectite. Thus, higher sorption capacities of the clay fraction for the Silurian samples as compared to the Ediacaran samples could be the result of the abundance of chlorite (appendix 1). However, this does not explain as to why zero sorption was computed for the muscovite/illite phase of the Ediacaran samples. Reported maximum excess methane sorption capacities for illite range from 0.055 mmol/g to 0.13 mmol/g (Ross and Bustin, 2009; Ji et al., 2012; Liang et al., 2016). McDowell and Elders (1980) observed that, at temperatures of approximately 548.15 K, illite/mica changes gradually from fine-grained illite to coarse-grained recrystallized mica. Such change could be accompanied by a shift of the pore size towards larger pores and therefore decreasing surface area and sorption capacity. Since the thermal history of Ediacaran samples used in this study is relatively poorly known, the use of empirical formulas to relate vitrinite reflectance to palaeotemperature has been applied as a first approximation. Depending on whether relatively slow or fast heating occurred during burial, different empirical formulations are typically used (Waliczek et al., 2021):

$$T_{peak} = (\ln VR_r + 1.68)/0.0124 \quad (\text{Eq.9})$$

$$T_{peak} = (\ln VR_r + 1.19)/0.00782 \quad (\text{Eq.10})$$

Here, T_{peak} denotes the maximum paleotemperature (K) and VR_r denotes the measured vitrinite reflectance (%). From these empirical formulas, the temperatures were between 510.15 and 592.15 K for Ediacaran samples while 468.15 – 566.15 K were computed for Silurian samples. Therefore, recrystallisation in these Ediacaran samples could be responsible for altered sorption capacities. Another possibility emerges from the observations of Weaver (1967, 1989). He found that illite in Precambrian shales was likely formed by alteration of feldspar in alkaline environments whereas illite in Paleozoic shales predominantly formed by illite/smectite conversion. While illite/smectite conversion could be related to a solid-state transformation, formation of illite from feldspars is related to dissolution and precipitation processes. This

could explain differences in sorption characteristics as well but requires further in-detail studies on the origins of illite in both sample sets.

The average Langmuir pressure (5.63 MPa) of the Silurian shales was 1.6 times higher than that (3.56 MPa) of the Ediacaran shales. Zhang et al. (2012) observed a similar trend (decreasing Langmuir pressure with increasing thermal maturity) for shales, albeit at lower vitrinite reflectances (0.58% - 2.01%). They attributed this phenomenon to a higher degree of aromatization of the kerogen. In this study, the Langmuir pressure difference could also be derived from differences in the pore size distribution as the average micropore volume fraction of the Ediacaran shales is approximately two times higher than that of the Silurian shales.

4.5.2 Effect of thermal maturity on methane sorption capacity

Several studies found that methane sorption capacity in shales normalized to the TOC content increases upon thermal maturation (Gasparik et al., 2014; Hu et al., 2015). Possible reasons for such an increasing sorption capacity are: (1) an increasing fraction of organic matter-hosted porosity (increasing specific surface area) due to kerogen conversion (Ross and Bustin, 2009; Klaver et al., 2015a) and (2) an increasing methane affinity of organic matter due to an increasing proportion of aromatic structures relative to aliphatic structures (Vandenbroucke and Largeau, 2007). Additionally, it was found that TOC-normalized methane sorption capacity decreases in highly over-mature shales from a vitrinite reflectance of approximately 2.0 – 2.4 % onwards (Gasparik et al., 2014; Yang et al., 2015). This was attributed to an increasing carbonization and an associated destruction of organic matter-hosted micro-pores (Yang et al., 2015). It should be noted that these studies exclusively attributed the sorption capacities (Langmuir volumes) to organic matter, thereby neglecting a potential contribution of clay minerals to total sorption capacity. While this is a valid simplification for high TOC shales and coals, the impact of clay minerals should not be neglected for shales with lower organic matter content. To exemplify the potential effect of clay minerals on the previously reported maturity trend, Eq. 8 was utilized to compute Langmuir volumes of organic matter from other published data (Gasparik et al., 2014; Yang et al., 2015; Merkel et al., 2016; Li et al., 2017; Fink et al., 2018; Nolte et al., 2019; Gaus et al., 2020) and data from this study under three different assumptions: (1) zero clay mineral contribution to total sorption capacity, (2) 0.1 mmol/g clay mineral contribution to total sorption capacity and (3) 0.2 mmol/g clay mineral contribution to total sorption capacity (Fig 4.12). The three assumptions are based on computation results from chapter 4.5.1 and published sorption capacities for individual clay

minerals (Ross and Bustin, 2009; Ji et al., 2012; Ziemiański et al., 2020). Vitrinite reflectances for all sample sets used in Fig 4.12 range from 0.50% to 4.24% and TOC contents from 2.2 wt.% to 45.0 wt.%. Under assumption of the minimum clay contribution (0 mmol/g, upper error bars for maximum deviations in Fig 4.12) an inverted U-shaped trend of sorption capacity with increasing vitrinite reflectance is apparent as was observed by Gasparik et al. (2014) and Yang et al. (2015) from vitrinite reflectances of 0.5% to 3.72%. However, adjusting the clay mineral sorption to values of 0.1 mmol/g (intermediate contribution, individual data points in Fig 4.12) and 0.2 mmol/g (maximum contribution, lower error bars for maximum deviations in Fig 4.12) indicates that clay mineral contributions cannot be neglected as the shift of individual data points along the y-axis due to varying clay mineral contributions may be in the same range as the proposed inverted U-shaped trend due to thermal maturation. This is especially valid if TOC content is relatively low and the clay mineral fraction is relatively high. Results from Gaus et al. (2020) (Kimmeridge & Bazhenov shales) and Gasparik et al. (2014) (Barnett & Alum shales) in Fig 4.12 display that changes in the sorption capacity due to differences in the pretreatment (different particle sizes) and due to heterogeneity, respectively, are in the same range as the proposed inverted U-shaped trend due to thermal maturation as well. Additionally, it should be noted that the thermal history can be affected by different parameters such as burial depth, uplift and erosion, basal heat flow and magmatic activity as well as physical properties of the formation (Hantschel and Kauerauf, 2009). Results from Nolte et al. (2019) for shales from the Collingham and Whitehill Formations from South Africa exhibit higher sorption capacities than expected, which is likely related to the fact that thermal maturity was strongly influenced by magmatic activity at rather shallow burial depth.

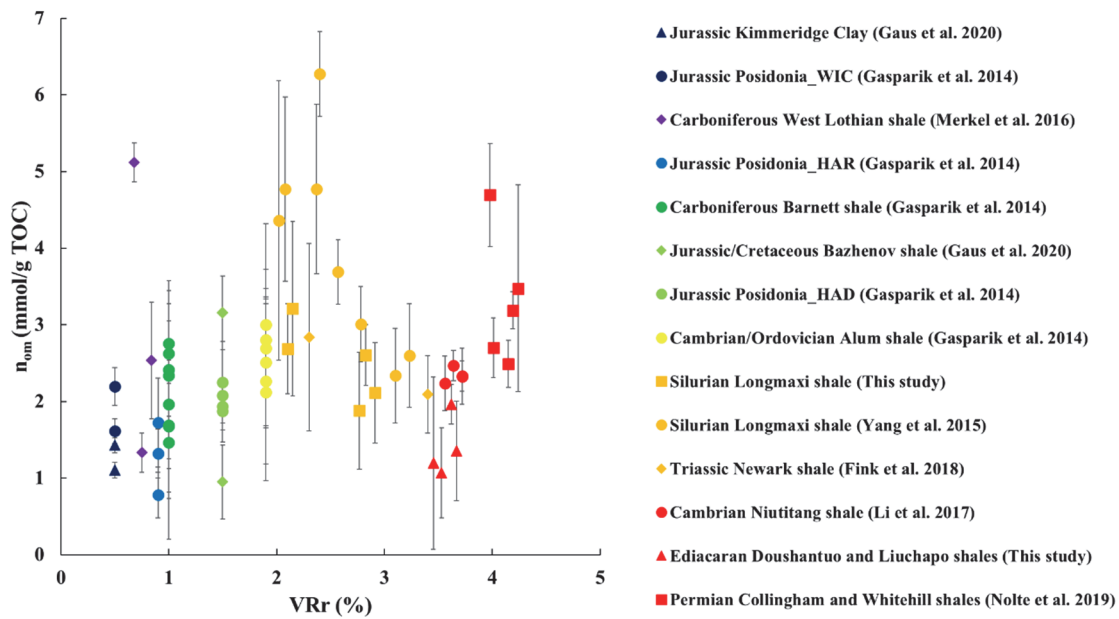


Fig 4.12 Relationship of estimated Langmuir volume of organic matter and equivalent vitrinite reflectance (symbols represent estimated Langmuir volumes of organic matter under the assumption of 0.1 mmol/g contribution of clay minerals to total sorption capacity and the error bars reflect assumptions of 0 and 0.2 mmol/g clay mineral contribution).

4.5.3 Pore structure

The strong correlation between TOC content and CO₂ micropore volume and methane sorption capacity indicates that microporosity associated with organic matter has a major control on methane sorption capacity for both samples. However, no correlation was found between TOC content and BET surface area for both shales (Fig 4.9a). Considering the relatively high specific surface areas of pure illite (38.5-165.7 m²/g) (Ziemiański et al., 2020) one possible reason could be that clay minerals contribute significantly to the surface area of the studied shales. However, it was shown in chapter 4.5.1 that clay minerals of the Ediacaran samples do not contribute to the Langmuir volume. According to Gan et al. (1972), Cazorla-Amorós et al. (1998) and Busch et al. (2016), N₂ shows significantly lower diffusivity in micropores smaller than 0.7 nm when compared to CO₂. This phenomenon was also observed in our study, as the CO₂ micropore volumes of two Ediacaran samples and one Silurian sample were significantly higher than the N₂ micropore volumes (Fig 4.9c). This resulted in an only partly accessible micropore volume for N₂ at the given experimental conditions. Besides, the interpreted pore size from N₂ adsorption isotherms is between 1.6 and 153 nm, while micropores between 1.2 nm and 1.6 nm can be interpreted from CO₂ isotherms. Therefore, the BET specific surface area derived from N₂ adsorption isotherms could only reflect the apparent specific surface area of relatively

coarse micropores, mesopores and fine macropores.

Burial-related compaction in shales leads to a strong reduction of porosity and changes in the pore structure. Vitrinite reflectances of the Ediacaran ($VR_r = 3.5 - 3.7\%$) and Silurian shales ($VR_r = 2.1 - 3.0\%$) obtained in this study imply a higher thermal maturity of the Ediacaran shales related to burial. Basin modelling results indicated that maximum burial of the Ediacaran shales likely exceeded a depth of 6000 m whereas burial of the Silurian shales was up to 4500 m (Tan et al. 2013; Zou et al. 2014). This is also reflected by total porosities (Silurian > Ediacaran) and micropore volume fractions (Ediacaran > Silurian) obtained in this study. Pore structures, in addition to burial-related compaction, might also be influenced by the origin of silica. Although XRD measurements from this study revealed similar silica contents for both shales (Table 4.1), it is likely that the origins of silica in both shales are different (silica biomineralizers are possibly not the main source of silica prior to the Cambrian). Zhao et al. (2017) reported an authigenic microcrystalline quartz content of up to 60% for samples of the Wufeng and Longmaxi Formations. This silica content was shown to originate from biogenic silica dissolution and re-crystallization. For Ediacaran rocks it was shown that silica predominantly originated from dissolved silica in oceans (Maliva et al., 1989; Tarhan et al., 2016). Whereas it was shown that biogenic silica ultimately may lead to an increasing rigidity of the rock and therefore to preservation of pore space during burial for the Silurian (Wufeng and Longmaxi) shale (Zhao et al., 2017), it is currently unknown as to how silica derived from non-biogenic sources influenced the pore structure during burial.

A higher micropore volume fraction and lower mesopore volume of the Ediacaran shales when compared to the Silurian shales was observed, which is also reflected by recorded gas uptake data from high-pressure methane sorption experiments (Fig 4.5) as equilibration times of the Ediacaran shales are more than two times larger at similar particle sizes (between 63 and 354 μm). Since matrix permeabilities determine the long-term gas production in gas shales (Ghanizadeh et al., 2014; Fink et al., 2018), this observation can be regarded as a first indication of a less favorable pore structure of the Ediacaran shales with respect to long-term production when compared to the Silurian shales.

4.5.4 Gas-in-place

To estimate the maximum gas-in-place (GIP) quantity, the specific pore volume (free gas) and the excess sorption capacity at reservoir conditions are needed. Based on interpretations of Zhu

et al. (2016) and Xu et al. (2018b) a geothermal gradient of 25 K/km and a pore pressure gradient of 14.2 MPa/km were used for GIP computations. The average surface temperature was set to 288.15 K. Experimental conditions of the methane sorption isotherms in this study were thus created at reservoir temperatures and covered reservoir pore pressure conditions.

Fig 4.13 shows free, sorptive and maximum GIP amounts computed for a depth of 1200 m (approximately the current depth of retrieved cores of the Ediacaran samples) for the Ediacaran and Silurian shales at dry conditions. Whereas the computed sorptive storage of the Ediacaran shales (0.014-0.120 mmol/g) is similar to that of the Silurian shales (0.039-0.128 mmol/g), free gas storage amounts are considerably larger for the Silurian shales. Therefore, estimated total gas storage capacities are lower for the Ediacaran shales (0.054-0.251 mmol/g) when compared to the Silurian shales (0.237-0.330 mmol/g).

Insight into the water saturation of potential shale gas reservoirs is crucial for the accurate assessment of gas reserves as it has a strong control on volumetric and sorptive gas storage. Reported water saturations for the Silurian (Longmaxi) shale range between 20 to 50 vol.% (Hu et al., 2019). No reported water saturations could be found for the Ediacaran shales. Until a critical moisture content is reached, the sorption capacity decreases with increasing amounts of (pre-adsorbed) water (Gasparik et al., 2014; Merkel et al., 2015a; Yang et al., 2017). Additional water uptake above this critical moisture content has negligible influence on methane sorption capacity. Yang et al. (2017) report a 44% to 63% reduction in sorptive methane storage capacity for the Silurian (Longmaxi) shales above the critical moisture content (water content: 1.76 wt.% - 4.50 wt.%). Results obtained in this study on two Ediacaran samples show that sorptive methane storage capacities reduce by 32% to 48% above the critical moisture content (water content: 2.14 wt.% - 3.08 wt.%). It should therefore be noted that results from Fig 4.13 tend to reflect estimates of maximum gas storage as these calculations do not consider water saturation and the impact of water vapor on methane sorption capacity.

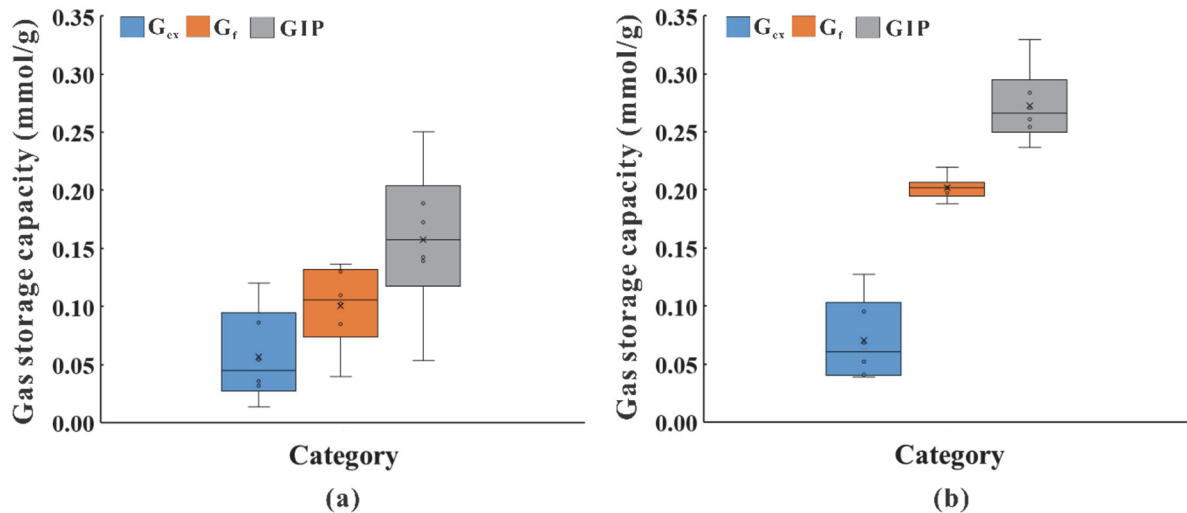


Fig 4.13 Estimates of excess sorption capacity (G_{ex}), free gas capacity (G_f) and total gas storage capacity (GIP) at a depth of 1200 m and corresponding temperature of 318.15 K for dry Ediacaran (a) and Silurian (b) shales (average porosity and bulk density of S1, S3 and S5 are used in the calculation of G_f for samples S2, S4 and S6 as porosities of these samples were likely enhanced by weathering).

Previous studies recommended that economically successful gas shale formations exhibit the following characteristics: TOC content > 2%, effective thickness > 30-50 m, brittle mineral content > 40%, porosity > 2% (Zou et al., 2017; Yasin et al., 2018; Hu et al., 2020a; Yang et al., 2021). Both Ediacaran and Silurian shales are rich in TOC contents (4% on average) and are widely distributed in the Upper Yangtze platform with thicknesses over 100 m. The average brittle mineral contents of both shales exceed 60%, favorable for hydraulic fracturing in shale gas exploitation. The average porosity (3.5%) of Ediacaran shales is approximately half of that (6.8%) in Silurian shales, which leads to lower estimated total gas storage capacities (0.054-0.251 mmol/g) when compared to Silurian shales. However, compared to the gas storage amounts (0.049-0.411 mmol/g) of Fayetteville, Haynesville, Antrim and Marcellus shales from North America, these shales all exceed the lower limit of commercial shale gas development (Zou et al., 2017). High gas production rate achieved from the Ediacaran shale, as mentioned in the introduction, further implies that the oldest potential shale gas formation could be extended from Cambrian to Ediacaran strata. Currently, with respect to Ediacaran shales, only a few studies exist and mainly focus on the pore types, pore size distribution and their relationship with organic matter and minerals (Chen et al. 2016; Yang et al. 2020). Our study also indicates that the pore structure of Ediacaran shales could limit the long-term shale gas production. However, limited by the number and type of Ediacaran samples in this study, experimental permeability measurements on cylindrical specimens could not be performed and

thus, evaluations on the relations between the pore network and the matrix permeability should be conducted in a future study.

4.6 Conclusions

High-pressure CH₄ sorption, low-pressure N₂ / CO₂ adsorption and water immersion porosimetry measurements were performed on Ediacaran (Liuchapo and Doushantuo Formations) and Lower Silurian (Longmaxi Formation) shales from the Upper Yangtze platform to characterize and compare pore structures as well as maximum methane storage capacities. The following conclusions can be drawn:

- (1) Maximum sorption capacities (Langmuir volumes) of Ediacaran and Silurian shales at dry conditions ranged between 0.02 - 0.19 mmol/g and 0.08 - 0.21 mmol/g, respectively. TOC content exhibits significant control on sorption capacity and CO₂ micropore volume shows a strong positive correlation with TOC content for both shales. Clay types but more importantly evolutionary differences (e.g., particle diameters and patterns of aggregation within the rock) during burial and different origins of illite could affect the sorptive storage. Additionally, a strong negative effect of water on methane sorption capacity of up to 64% (comparison of excess sorption at 10 MPa of samples in dry and moisturized state) was observed for the Ediacaran shales.
- (2) Computed total gas storage capacities (sorptive and free gas amounts combined) at present day reservoir conditions are lower for the Ediacaran shales (0.054 - 0.251 mmol/g) when compared to the Silurian shales (0.237 - 0.330 mmol/g).
- (3) Total porosities (Silurian > Ediacaran), mesopore volumes (Silurian > Ediacaran) and micropore fractions (Ediacaran > Silurian) indicate that compaction had a stronger influence on the Ediacaran shale. This could be related to deeper burial (larger vitrinite reflectances for the Ediacaran shales) but also to the origin of silica (biogenic vs. abiogenic) as silica biomineralizers were likely not the main source of silica prior to the Cambrian. A lower diffusion efficiency of the Ediacaran shales when compared to the Silurian shales was observed from gas uptake data of high-pressure methane sorption experiments. This observation can be regarded as a first indication of a less favorable pore structure of the Ediacaran shales with respect to long-term production when compared to the Silurian shales.
- (4) The effect of thermal maturity on maximum methane sorption capacities of organic matter

was investigated by comparison of shales with vitrinite reflectances ranging from 0.5% to 4.24% and TOC contents ranging from 2.2 to 45.0 wt.%. A clear relationship of maximum sorption capacity of organic matter and thermal maturity could not be identified as combined variations of sorption capacity due to sample preparation (particle size), sample heterogeneity, burial history and most importantly false estimations of clay mineral contribution to overall sorption capacity are larger than potential trends due to thermal maturity.

5. General discussion and outlook

In this thesis, a multi-scale characterization of the petrophysical properties of tight sedimentary rocks (limestone and shale) has been performed. A series of petrophysical and imaging techniques were applied on these rocks to characterize the pore structure, fluid transport properties and sorption capacity. Apart from the concise conclusions drawn at the end of chapters 2-4, a general discussion and suggestions for future studies are given below.

5.1 General discussion

5.1.1 Pore accessibility

A detailed characterization of the pore size distribution and pore morphology of the Cobourg limestone down to 10 nanometers was achieved by FIB- and BIB-SEM techniques. However, an unambiguous allocation of fluid flow pathways through the rock could not be achieved although a series of microstructural evidence infer that pores in the clay mineral phase are likely responsible for fluid flow. In order to provide more evidence on the dominant flow pathways in the intact Cobourg limestone, investigations on the connectivity of pores below the resolution of the above-mentioned methods in the calcite and clay mineral phases are of particular importance.

Porosity can be subdivided into an accessible (interconnected) and inaccessible (closed) fraction from a petrophysical viewpoint. The accessible fraction can be further subdivided into transport pores and storage (dead-end) pores. Since pore throats in the Cobourg limestone could not be imaged, we could only assume that pores in the carbonate phase belong to the inaccessible (closed) fraction and that therefore only pores in the silicate phase contribute to flow. However, fluid flow computations with this assumption generated somewhat unrealistic high permeability coefficients for the silicate phase. To investigate whether pores in the calcite are part of the accessible or inaccessible fraction, HP experiments could be first performed on the intact rock (plug) and successively on the same sample in a crushed state. Disruption of the rock fabric by crushing could open inaccessible pores (if existent) and therefore provides a direct measurement on closed pore volume. Since inaccessible pores in HP measurements contribute to the grain volume rather than the pore volume, successive opening of these pores by crushing would lead to a reduction of the grain volume and an increase in grain density. Such studies were performed on fine-grained rocks by Sondergeld et al. (2010), Klaja et al.

(2015), Fu et al. (2019) and Gaus et al. (2020). In all studies, grain densities/porosities increased upon particle size reduction.

Due to the practical pore resolution limitation of FIB-SEM, pore size distribution analyses of the calcite and clay mineral phases start at 25 nm in this study. By utilization of low-pressure nitrogen adsorption it could be examined whether the pore size distribution in the Cobourg limestone is dominated by pores < 25 nm. Ideally, clay mineral and calcite phases should be separated beforehand in order to differentiate between pores in each phase. This would also give an indication on whether pore connectivity exists below the image resolution or whether the pores are isolated (especially in the calcite) as suggested by image analyses. Since these measurements are performed on particles of approximately 200 μm in size, porosities from low-pressure nitrogen adsorption could be compared to HP measurements and BIB-SEM images to further investigate whether pores in the calcite phase are accessible. If large macropores (> 0.5 μm) account for the major fraction of pore volume in evaluation from low-pressure nitrogen adsorption, it demonstrates that large pores in calcite are likely connected.

Additionally, Wood's metal injection (WMI) in combination with BIB-SEM could be an alternative way to visualize the connected pore space at high resolution over a large area (several mm^2). The wood's metal (WM) is an alloy of 50% bismuth (Bi), 25% lead (Pb), 12.5% tin (Sn) and 12.5% cadmium (Cd) and has similar physical properties as mercury when it melts at 70°C. In such an experiment, the liquid WM would be injected into the pore space of Cobourg limestone samples by stepwise increasing the pressure up to 316 MPa at 90 °C. By decreasing the temperature at maximum pressure, the WM would again solidify. Afterwards, the injected rock samples can be cut, polished and imaged with BIB-SEM (Klaver et al., 2015b). Based on the qualitative and quantitative image analysis, the pore accessibility and connectivity in the calcite and clay mineral phases could be characterized and compared by direct evidence of pores filled with WM (down to 10 nm).

5.1.2 Gas-In-Place estimation

Although a detailed comparison of the pore structure and sorption capacity of Ediacaran and Lower Silurian gas shales were documented in chapter 4, some aspects of sorption experiments can be improved and other relevant experiments can be performed in the future to estimate the maximum Gas-In-Place amount more accurately.

In chapter 4, sorption measurements were conducted on dry and moisturized shale samples

with particle sizes ranging between 63 and 354 μm at unconfined conditions. It has been reported that particle size can influence the sorption capacity. Ji et al. (2012) found an increase in excess sorption capacity at approximately 11 MPa from 0.016 mmol/g to 0.059 mmol/g and 0.266 mmol/g to 0.305 mmol/g for chlorite-rich and montmorillonite-rich clay rocks, respectively, upon particle size reduction from 270-830 μm to $<53 \mu\text{m}$. Gaus et al. (2020) reported an increase of Langmuir volume from 0.111 mmol/g to 0.193 mmol/g for the Bazhenov shale when comparing core plugs (38 mm in diameter and 40 mm in length) to samples with $<1 \mu\text{m}$ particle size. In addition to the effects of rock fabric, sorption measurements on crushed samples disregard potential effects of overburden on sorption capacity. Pone et al. (2009) observed that an application of confining pressure of 13.8 MPa reduces CH_4 and CO_2 sorption capacities of bituminous coals by 64% and 91%, respectively. Liu et al. (2016) found a reduction of approximately 6% of methane sorption capacity with effective stress increasing from 1 to 33 MPa. Gaus et al. (2021) reported stress dependence of the methane excess sorption capacity, expressed as percentage reduction at 40 MPa overburden as compared to unconfined conditions, decreases in the order of Eagle Ford shale (~56%), Bossier shale (~30%), Kimmeridge shale (~14%), and Alum shale (~5%). This was attributed to the additional stress-strain work that needs to be performed during sorption-induced swelling against the effective stress at confined conditions. Sorption measurements at different temperatures must be conducted to estimate the evolution of sorption capacity of shale formations with increasing depth. It is known that moisture has a negative effect on methane sorption capacities in coals and shales (Gasparik et al., 2014; Merkel et al., 2015a; Yang et al., 2017). However, thus far these measurements were exclusively performed on crushed rocks and therefore at unconfined conditions. The evolution of sorption capacity of confined core samples as a function of water content could be different. For example, the critical moisture content has never been reported for shale cores under effective stress and could differ for plugs at confined conditions as compared to crushed samples at unconfined conditions.

Considering the effects of particle size, stress, temperature and moisture, it would be meaningful to measure the sorption capacities of moisturized shale core samples under in-situ effective stress and temperature. In combination with pore volume measured at in-situ effective stress, estimations of Gas-In-Place amounts should be more representative and accurate. However, such measurements are also challenging because the equilibrium times of gas uptake will be much longer than those for the crushed rocks. It also requires careful calibration of the apparatus considering the typically low porosities of shales.

5.2 Outlook

5.2.1 Competitive sorption on core shales under effective stress

Experimental results in literature have shown that CO₂ is more favourably sorbed than CH₄ when both gas species coexist in shales (Nuttal et al., 2005; Merkel et al., 2015b; Klewiah et al., 2020). In the context of enhanced shale gas recovery (ESGR), this behavior has great potential because injecting CO₂ into shale formations would trigger desorption of CH₄ molecules at the sorption sites. Methane molecules would return to the bulk free phase in the pore space and increase the rate and volume of CH₄ production (Merkel et al., 2015b). Competitive sorption of CH₄ and CO₂ from a two-component gas mixture is conducted on shales to evaluate the maximum sorption capacity as well as the selectivity. The relative sorption capacity of shales for either CO₂ or CH₄ is controlled by the respective interaction energy (thermodynamic forces), molecular size and accessibility of each gas type to the nanoporous network of the shale matrix (Klewiah et al., 2020). The sorption selectivity parameter is typically used to evaluate the competitive sorption between CO₂ and CH₄. However, competitive sorption of CH₄ and CO₂ on shales are widely conducted on crushed rocks at unconfined conditions (Nuttal et al., 2005; Merkel et al., 2015b). Whether the sorption selectivity parameter is different for competitive sorption on core plugs at in-situ stressed states needs to be examined in the future study.

5.2.2 Fracture sealing and reopening

The identification of open stylolites in the Cobourg limestone and their conduit role for fluid flow indicate that the matrix permeability should not be considered as a critical factor for the sealing efficiency of the host rock. Day et al. (2017) analysed the microstructure of Cobourg limestone by SEM and showed fractures preferentially occurring in the fine-grained clay matrix. In the context of radioactive waste disposal, the excavation of a repository will inevitably cause fracturing around the openings and flow in the excavation damaged zone (EDZ) could be more pronounced than in the intact host rock. After backfilling and sealing the repository, it is likely that the fractures in the EDZ will be slowly sealed again under the combined impact of stress and water-induced swelling of clay minerals (Zhang, 2015). The fluid flow through the EDZ may be reduced. In the safety assessment of a radioactive waste repository, an important issue is the impact of gases (produced from the anoxic corrosion of metallic components) on the host rocks. The main concerns are the accumulated gas pressure and whether pathways can be

created by gases for transporting radionuclides into the biosphere. Therefore, it would be meaningful to investigate the mechanism of gas migration in the damaged Cobourg limestone in the following aspects:

- Fractures in the EDZ are initially occupied by air and will be slowly sealed under stress (backfilling and sealing). The relation between gas permeability and the closure of dry fractures under various loads (isotropic and deviatoric compression) is worth studying.
- With the evaporation of pore water in the surrounding rocks, the fractures of EDZ will be slowly moisturized. The clay minerals on the fracture planes will start to swell and decrease the apertures, which probably will slow down gas movement. Effects of gas humidity on the gas flow through fractures should be investigated.
- The pore water in the saturated rock formations will migrate into the fractures of the EDZ because of hydraulic gradients. Consequently, the sealing intensity of fractures will be further enhanced. For water-saturated fractures, the gas flow behavior at different sealing intensity and the impact of gas pressure on the reopening of closed fractures and generation of new fractures should be examined by gas breakthrough experiments.
- With increasing time of storage of nuclear waste, heat generated from radioactive decay can be clearly pronounced and should therefore influence the temperature distribution within the host rock and also alter its petrophysical properties. Therefore, the impact of temperature on the transport properties of fractured host rocks should be investigated.

5.2.3 Fluid flow testing incorporated with CT scanning

Experimental studies of fluid transport through natural porous media are ideally performed in triaxial flow cells to mimic geological conditions (in-situ temperature and stress). In many studies, sample conditions were not well characterized or only examined by visual, microscopic or SEM observations before or after the measurements, which does not reflect microstructural changes under the impact of temperature, stress or fluid migration during the measurements (Ghanizadeh et al., 2014; Heller et al., 2014). With the potential of visualizing deformation and flow processes during these measurements, combining triaxial flow cells and micro-CT scanning would be of great interest to the geoscientific community. Soldal et al. (2017) combined a micro-CT scanner and X-ray transparent triaxial apparatus to visualize the deformation and failure of cylindrical sandstones (38mm in diameter) with increasing shear stresses. Glatz et al. (2018) reported a high-temperature (>400 °C) and high-pressure (>13.8

MPa confining pressure and >68.9 MPa axial stress) triaxial flow cell combined with a X-ray CT scanner. The new triaxial system allows for time-lapse imaging to capture the impact of effective stress on the fluid distribution and porous structure.

The combination of a triaxial flow cell and a micro-CT scanner for fluid flow testing provides deformation information not available from traditional deformation sensors. It can also be applied to visualize the microstructural evolution of organic-rich immature shales as a function of the temperature (especially during hydrocarbon formation and expulsion) at confined conditions. In this way, the porosity and permeability evolution of shales with thermal maturity can be well interpreted by corresponding changes of microstructure.

6. References

- Adzumi, H., 1937. Studies on the flow of gaseous mixtures through capillaries. III. The flow of gaseous mixtures at medium pressures. *Bulletin of the Chemical Society of Japan*, 12(6), 292–303.
- Allan, C.J., Nuttall, K., 1997. How to cope with the hazards of nuclear fuel waste. *Nuclear engineering and design*, 176 (1-2), 51-66.
- Andrä, H., Combaret, N., Dvorkin, J., Glatt, E., Han, J., Kabel, M., Keehm, Y., Krzikalla, F., Lee, M., Madonna, C., Marsh, M., 2013. Digital rock physics benchmarks—Part II: Computing effective properties. *Computers & Geosciences*, 50, 33-43.
- Anovitz, L.M., Cole, D.R., 2015. Characterization and analysis of porosity and pore structures. *Reviews in Mineralogy and geochemistry*, 80(1), 51-154.
- Apted, M.J., Ahn, J. eds., 2017. *Geological repository systems for safe disposal of spent nuclear fuels and radioactive waste*. Woodhead Publishing.
- Bachu, S., 2000. Sequestration of CO₂ in geological media: criteria and approach for site selection in response to climate change. *Energy Conversion and Management*, 41(9), 953-970.
- Backeberg, N.R., Iacoviello, F., Rittner, M., Mitchell, T.M., Jones, A.P., Day, R., Wheeler, J., Shearing, P.R., Vermeesch, P., Striolo, A., 2017. Quantifying the anisotropy and tortuosity of permeable pathways in clay-rich mudstones using models based on X-ray tomography. *Scientific Reports*, 7(1), 1-12.
- Barrett, E.P., Joyner, L.G., Halenda, P.P., 1951. The determination of pore volume and area distributions in porous substances. I. Computations from nitrogen isotherms. *Journal of the American Chemical society*, 73(1), 373-380.
- Bass, J.D., 1995. Elasticity of minerals, glasses, and melts. *Mineral physics & crystallography: a handbook of physical constants*, 2, 45-63.
- Beauheim, R.L., Roberts, R.M., Avis, J.D., 2014. Hydraulic testing of low-permeability Silurian and Ordovician strata, Michigan Basin, southwestern Ontario. *Journal of hydrology*, 509, 163-178.
- Berner, R.A., Raiswell, R., 1984. C/S method for distinguishing freshwater from marine sedimentary rocks. *Geology*, 12(6), 365-368.
- Birkholzer, J., Houseworth, J., Tsang, C.F., 2012. Geologic disposal of high-level radioactive waste: Status, key issues, and trends. *Annual Review of Environment and Resources*, 37, 79-106.
- Blunt, M.J., Bijeljic, B., Dong, H., Gharbi, O., Iglauer, S., Mostaghimi, P., Paluszny, A., Pentland, C., 2013. Pore-scale imaging and modelling. *Advances in Water Resources*, 51, 197-215.
- Bourbie, T., Walls, J., 1982. Pulse decay permeability: analytical solution and experimental test. *Society of Petroleum Engineers Journal*, 22(05), 719-721.
- Brace, W.F., Walsh, J.B., Frangos, W.T., 1968. Permeability of Granite under High Pressure. *Journal of Geophysical Research*, 73(6), 2225-2236.
- Breen, E.J., Jones, R., 1996. Attribute openings, thinnings, and granulometries. *Computer vision and image understanding*, 64(3), 377-389.
- Brower, K.R., Morrow, N.R., 1985. Fluid flow in cracks as related to low-permeability gas sands. *Society of Petroleum Engineers Journal*, 25(02), 191-201.
- Brunauer, S., Emmett, P.H., Teller, E., 1938. Adsorption of gases in multimolecular layers. *Journal of the American chemical society*, 60(2), 309-319.

- Bultreys, T., Van Hoorebeke, L., Cnudde, V., 2015. Multi-scale, micro-computed tomography-based pore network models to simulate drainage in heterogeneous rocks. *Advances in Water Resources*, 78, 35-49.
- Busch, A., Bertier, P., Gensterblum, Y., Rother, G., Spiers, C.J., Zhang, M. and Wentinck, H.M., 2016. On sorption and swelling of CO₂ in clays. *Geomechanics and Geophysics for Geo-energy and Geo-resources*, 2(2), 111-130.
- Cavé, L., Al, T., Xiang, Y., Vilks, P., 2009. A technique for estimating one-dimensional diffusion coefficients in low-permeability sedimentary rock using X-ray radiography: Comparison with through-diffusion measurements. *Journal of contaminant hydrology*, 103(1-2), 1-12.
- Cazorla-Amorós, D., Alcaniz-Monge, J., De la Casa-Lillo, M.A., Linares-Solano, A., 1998. CO₂ as an adsorptive to characterize carbon molecular sieves and activated carbons. *Langmuir*, 14(16), 4589-4596.
- CEPI, 2019. China Energy Development Report of 2018. China Electric Power Planning & Engineering Institute.
- Chalmers, G.R., Bustin, R.M., 2007. The organic matter distribution and methane capacity of the Lower Cretaceous strata of Northeastern British Columbia, Canada. *International Journal of Coal Geology*, 70(1-3), 223-239.
- Chalmers, G.R., Ross, D.J., Bustin, R.M., 2012. Geological controls on matrix permeability of Devonian Gas Shales in the Horn River and Liard basins, northeastern British Columbia, Canada. *International Journal of Coal Geology*, 103, 120-131.
- Charvet, J., 2013. The Neoproterozoic–early Paleozoic tectonic evolution of the South China Block: an overview. *Journal of Asian Earth Sciences*, 74, 198-209.
- Chen, J., 2018. Shale Gas Exploration and Development Progress in China and the way forward. In IOP Conference Series: Earth and Environmental Science (Vol. 113, No. 1, 012178). IOP Publishing.
- Chen, Q., Zhang, J., Tang, X., Li, W., Li, Z., 2016. Relationship between pore type and pore size of marine shale: An example from the Sinian–Cambrian formation, upper Yangtze region, South China. *International Journal of Coal Geology*, 158, 13-28.
- Clarkson, C.R., Bustin, R.M., 1996. Variation in micropore capacity and size distribution with composition in bituminous coal of the Western Canadian Sedimentary Basin: implications for coalbed methane potential. *Fuel*, 75(13), 1483-1498.
- Clarkson, C.R., Haghshenas, B., Ghanizadeh, A., Qanbari, F., Williams-Kovacs, J.D., Riazi, N., Debuhr, C. and Deglint, H.J., 2016. Nanopores to mega fractures: Current challenges and methods for shale gas reservoir and hydraulic fracture characterization. *Journal of Natural Gas Science and Engineering*, 31, 612-657.
- Cnudde, V., Boone, M.N., 2013. High-resolution X-ray computed tomography in geosciences: A review of the current technology and applications. *Earth-Science Reviews*, 123, 1-17.
- Curtis, M.E., Sondergeld, C.H., Ambrose, R.J., Rai, C.S., 2012. Microstructural investigation of gas shales in two and three dimensions using nanometer-scale resolution imaging. *AAPG bulletin*, 95(4), 555-577.
- Dai, J., Dong, D., Ni, Y., Hong, F., Zhang, S., Zhang, Y., Ding, L., 2020. Some essential geological and geochemical issues about shale gas research in China. *Natural Gas Geoscience*, 31(6), 745–760.
- Dang, W., Zhang, J., Tang, X., Chen, Q., Han, S., Li, Z., Du, X., Wei, X., Zhang, M., Liu, J., Peng, J., 2016. Shale gas potential of Lower Permian marine-continental transitional black shales in the Southern North China Basin, central China: Characterization of organic geochemistry. *Journal of Natural Gas Science and Engineering*, 28, 639-650.

- David, C., Wong, T.F., Zhu, W., Zhang, J., 1994. Laboratory measurement of compaction induced permeability change in porous rocks: implication for the generation and maintenance of pore pressure excess in the crust. *Pure Appl Geophys*, 143:425–456.
- Davy, C. A., Hu, Z.Z., Selvadurai, A.P.S., Klaver, J., Willemetz, M.C., Agostini, F., Skoczylas, F., Dewanckele, J., Amann-Hildenbrand, A., Lenormand, R., 2019. Transport properties of the Cobourg Limestone: A benchmark investigation. SCA2019-037.
- Day, J.J., Diederichs, M.S., Hutchinson, D.J., 2017. The influence of mineralogy and grain scale features in healed intrablock structure on direct shear properties in the Cobourg Limestone. In 51st US Rock Mechanics/Geomechanics Symposium. American Rock Mechanics Association.
- Deng, B., Liu, S.G., Liu, S., Li, Z.W., Zhao, J.C., 2009. Restoration of exhumation thickness and its significance in Sichuan Basin. *Journal of Chengdu University of Technology (Science & Technology Edition)*, 36(6), 675-686.
- Desbois, G., Urai, J.L., Kukla, P.A., 2009. Morphology of the pore space in claystones—evidence from BIB/FIB ion beam sectioning and cryo-SEM observations. *eEarth Discussions*, 4(1), 1-19.
- Dierick, M., Van Loo, D., Masschaele, B., Boone, M., Pauwels, E., Brabant, L., Cnudde, V., Van Hoorebeke, L., 2013. HECTOR, a new multifunctional micro-CT scanner at UGCT. In IEEE 10th International symposium on Biomedical Imaging: From nano to macro.
- Doebelin, N., Kleeberg, R., 2015. Profex: a graphical user interface for the Rietveld refinement program BGMN. *Journal of applied crystallography*, 48(5), 1573-1580.
- Dong, J.J., Hsu, J.J., Wu, W.J., Shimamoto, T., Hung, J.H., Yeh, E.C., 2010. Stress dependence of the permeability and porosity of sandstone and shale from TCDP Hole-A. *Int J Rock Mech Min Sci*, 47(7):1141–1157.
- Dreisbach, F., Staudt, R., Keller, J.U., 1999. High pressure adsorption data of methane, nitrogen, carbon dioxide and their binary and ternary mixtures on activated carbon. *Adsorption*, 5(3), 215-227.
- Dubinina, M.M., Astakhov, V.A., 1971. Development of the concepts of volume filling of micropores in the adsorption of gases and vapors by microporous adsorbents. *Bulletin of the Academy of Sciences of the USSR, Division of chemical science*, 20(1), 8-12.
- EIA, 2015. World Shale Resource Assessments. U.S. Energy Information Administration.
- EIA, 2019. U.S. Shale Gas Production, Annual. U.S. Energy information Administration.
- Fall, M., Nasir, O., Nguyen, T.S., 2014. A coupled hydro-mechanical model for simulation of gas migration in host sedimentary rocks for nuclear waste repositories. *Engineering geology*, 176, 24-44.
- Farquhar, R.A., Smart, B.G.D., Todd, A.C., Tompkins, D.E., Tweedie, A.J., 1993. Stress sensitivity of low-permeability sandstones from the Rotliegendes sandstone. In SPE annual technical conference and exhibition. Society of Petroleum Engineers.
- Fatt, I., Davis, D.H., 1952. Reduction in permeability with overburden pressure. *Journal of Petroleum Technology*, 4(12), 16.
- Faybishenko, B., Swift, P. eds., 2016. International Approaches for Deep Geological Disposal of Nuclear Waste: Geological Challenges in Radioactive Waste Isolation: Fifth Worldwide Review. Lawrence Berkeley National Laboratory.
- Feng, G., Zhu, Y., Chen, S., Wang, Y., Ju, W., Hu, Y., You, Z., Wang, G.G., 2020. Supercritical Methane Adsorption on Shale over Wide Pressure and Temperature Ranges: Implications for Gas-in-Place Estimation. *Energy & Fuels*, 34(3), 3121-3134.
- Fink, R., Amann-Hildenbrand, A., Bertier, P., Littke, R., 2018. Pore structure, gas storage and matrix transport characteristics of lacustrine Newark shale. *Marine and Petroleum Geology*, 97, 525-539.

- Fink, R., Krooss, B.M., Amann, A., 2017. Stress-dependence of porosity and permeability of the Upper Jurassic Bossier shale: an experimental study. *Geological Society London Special Publications*, 454.
- Flügel, E., 2013. *Microfacies of carbonate rocks: analysis, interpretation and application*. Springer Science & Business Media.
- Fu, Y., Jiang, Y., Wang, Z., Hu, Q., Xie, J., Ni, G., Lei, Z., Zhou, K., Liu, X., 2019. Non-connected pores of the Longmaxi shale in southern Sichuan Basin of China. *Marine and Petroleum Geology*, 110, 420-433.
- Fyfe, W.S., 1999. Nuclear waste isolation: an urgent international responsibility. *Engineering geology*, 52(3-4), 159-161.
- Gan, H., Nandi, S.P., Walker Jr, P.L., 1972. Nature of the porosity in American coals. *Fuel*, 51(4), 272-277.
- Gangi, A.F., 1978. Variation of whole and fractured porous rock permeability with confining pressure. In *International Journal of Rock Mechanics and Mining Sciences & Geomechanics Abstracts* (Vol. 15, No. 5, 249-257). Pergamon.
- Gasparik, M., Bertier, P., Gensterblum, Y., Ghanizadeh, A., Krooss, B.M., Littke, R., 2014. Geological controls on the methane storage capacity in organic-rich shales. *International Journal of Coal Geology*, 123, 34-51.
- Gaus, G., Fink, R., Amann-Hildenbrand, A., Krooss, B.M. and Littke, R., 2021. Experimental determination of porosity and methane sorption capacity of organic-rich shales as a function of effective stress: Implications for gas storage capacity. *AAPG Bulletin*, 105(2), 309-328.
- Gaus, G., Kalmykov, A., Krooss, B.M., Fink, R., 2020. Experimental Investigation of the Dependence of Accessible Porosity and Methane Sorption Capacity of Carbonaceous Shales on Particle Size. *Geofluids*.
- Gensterblum, Y., Ghanizadeh, A., Cuss, R.J., Amann-Hildenbrand, A., Krooss, B.M., Clarkson, C.R., Harrington, J.F., Zoback, M.D., 2015. Gas transport and storage capacity in shale gas reservoirs—A review. Part A: Transport processes. *Journal of Unconventional Oil and Gas Resources*, 12, 87-122.
- Gensterblum, Y., Van Hemert, P., Billefont, P., Busch, A., Charriere, D., Li, D., Krooss, B.M., De Weireld, G., Prinz, D., Wolf, K.H., 2009. European inter-laboratory comparison of high-pressure CO₂ sorption isotherms. I: Activated carbon. *Carbon*, 47(13), 2958-2969.
- Ghabezloo, S., Sulem, J., Guédon, S., Martineau, F., 2009. Effective stress law for the permeability of a limestone. *International Journal of Rock Mechanics and Mining Sciences*, 46(2), 297-306.
- Ghanbarian, B., Hunt, A.G., Ewing, R.P. and Sahimi, M., 2013. Tortuosity in porous media: a critical review. *Soil science society of America journal*, 77(5), 1461-1477.
- Ghanizadeh, A., Bhowmik, S., Haeri-Ardakani, O., Sanei, H., Clarkson, C.R., 2015. A comparison of shale permeability coefficients derived using multiple non-steady-state measurement techniques: Examples from the Duvernay Formation, Alberta (Canada), *Fuel*, 140, 371-387.
- Ghanizadeh, A., Gasparik, M., Amann-Hildenbrand, A., Gensterblum, Y., Krooss, B.M., 2014. Experimental study of fluid transport processes in the matrix system of the European organic-rich shales: I. Scandinavian Alum Shale. *Marine and Petroleum Geology*, 51, 79-99.
- Glatz, G., Lapene, A., Castanier, L.M., Kovscek, A.R., 2018. An experimental platform for triaxial high-pressure/high-temperature testing of rocks using computed tomography. *Review of Scientific Instruments*, 89(4), 045101.
- Głowacki, A., Selvadurai, A.P.S., 2016. Stress-induced permeability changes in Indiana limestone. *Engineering geology*, 215, 122-130.

- Grathoff, G.H., Peltz, M., Enzmann, F., Kaufhold, S., 2016. Porosity and permeability determination of organic-rich Posidonia shales based on 3-D analyses by FIB-SEM microscopy. *Solid Earth*, 7(4), 1145-1156.
- Grobe, A., Schmatz, J., Littke, R., Klaver, J., Urai, J.L., 2017. Enhanced surface flatness of vitrinite particles by broad ion beam polishing and implications for reflectance measurements. *International Journal of Coal Geology*, 180, 113-121.
- Guo, Q., Shields, G.A., Liu, C., Strauss, H., Zhu, M., Pi, D., Goldberg, T., Yang, X., 2007. Trace element chemo-stratigraphy of two Ediacaran–Cambrian successions in South China: implications for organo-sedimentary metal enrichment and silicification in the early Cambrian. *Paleogeography, Paleoclimatology, Paleoecology*, 254(1-2), 194-216.
- Guo, X., Guo, X., 2016. Nuclear power development in China after the restart of new nuclear construction and approval: A system dynamics analysis. *Renewable and Sustainable Energy Reviews*, 57, 999-1007.
- Gurvich, L.G., 1915. Acerca de la fuerza de atracción fisicoquímica [On the physico-chemical force of attraction]. *Journal of the Physical and Chemical Society of Russia*, 47, 805–827 [in Russian].
- Haeri-Ardakani, O., Al-Aasm, I., Coniglio, M., 2013. Petrologic and geochemical attributes of fracture-related dolomitization in Ordovician carbonates and their spatial distribution in southwestern Ontario, Canada. *Marine and Petroleum Geology*, 43, 409-422.
- Han, S., Zhang, J., Li, Y., Horsfield, B., Tang, X., Jiang, W., Chen, Q., 2013. Evaluation of Lower Cambrian shale in northern Guizhou province, South China: Implications for shale gas potential. *Energy & Fuels*, 27(6), 2933-2941.
- Hantschel, T. and Kauerauf, A.I., 2009. *Fundamentals of basin and petroleum systems modeling*. Springer Science & Business Media.
- Hao, F., Zou, H., Lu, Y., 2013. Mechanisms of shale gas storage: Implications for shale gas exploration in China. *AAPG bulletin*, 97(8), 1325-1346.
- Hekimi, B., 2012. *The physical and mechanical properties of an argillaceous limestone* (Doctoral dissertation, McGill University).
- Heller, R., Vermilyen, J., Zoback, M., 2014. Experimental investigation of matrix permeability of gas shales. *Experimental Investigation of Matrix Permeability of Gas Shales*. *AAPG bulletin*, 98(5), 975-995.
- Hildenbrand, A., Krooss, B.M., Busch, A., Gaschnitz, R., 2006. Evolution of methane sorption capacity of coal seams as a function of burial history—a case study from the Campine Basin, NE Belgium. *International Journal of Coal Geology*, 66(3), 179-203.
- Hildenbrand, A., Urai, J.L., 2003. Investigation of the morphology of pore space in mudstones—first results. *Marine and Petroleum Geology*, 20(10), 1185-1200.
- Hu, H., Zhang, T., Wiggins-Camacho, J.D., Ellis, G.S., Lewan, M.D. and Zhang, X., 2015. Experimental investigation of changes in methane adsorption of bitumen-free Woodford Shale with thermal maturation induced by hydrous pyrolysis. *Marine and Petroleum Geology*, 59, 114-128.
- Hu, Y., Li, X., Zhang, Z., He, J. and Li, G., 2020a. Numerical investigation on the hydraulic stimulation of naturally fractured Longmaxi shale reservoirs using an extended discontinuous deformation analysis (DDA) method. *Geomechanics and Geophysics for Geo-Energy and Geo-Resources*, 6(4), 1-21.
- Hu, Z., Duan, X., He, Y., Wu, J., Chang, J., Liu, L., Wu, K., Ma, Z., 2019. Influence of reservoir primary water on shale gas occurrence and flow capacity. *Natural Gas Industry B*, 6(1), 71-78.

- Hu, Z., Klaver, J., Schmatz, J., Dewanckele, J., Littke, R., Krooss, B.M., Amann-Hildenbrand, A., 2020b. Stress sensitivity of porosity and permeability of Cobourg limestone. *Engineering Geology*, 105632.
- IAEA, 2001. The use of scientific and technical results from underground research laboratory investigation for the geological disposal of radioactive waste. In: TECDOC-1243. IAEA, Vienna.
- Jafari, M., Cao, S.C., Jung, J., 2016. Geological CO₂ sequestration in saline aquifers: Implication on potential solutions of China's power sector. *Resources, Conservation and Recycling*, 121,137-155.
- Ji, L., Zhang, T., Milliken, K.L., Qu, J., Zhang, X., 2012. Experimental investigation of main controls to methane adsorption in clay-rich rocks. *Applied Geochemistry*, 27(12), 2533-2545.
- Jlassi, K., Krupa, I., Chehimi, M.M., 2017. Overview: clay preparation, properties, modification. In *Clay-polymer nanocomposites* (pp. 1-28). Elsevier.
- Jones, Jr., O. F., 1975. A laboratory study of the effects of confining pressure on fracture flow and storage capacity in carbonate rocks. *Journal of Petroleum Technology*, 27(01), 21-27.
- Joos, G., Freeman, I.M., 2013. *Theoretical physics*. Courier Corporation.
- Katsube, T. J., Mudford, B.S., Best, M. E., 1991. Petrophysical characteristics of shales from the Scotian Shelf. *Geophysics*, 56, 1681-1689.
- Keller, L.M., Holzer, L., Wepf, R., Gasser, P., 2011. 3D geometry and topology of pore pathways in Opalinus clay: Implications for mass transport. *Applied Clay Science*, 52(1-2), 85-95.
- Keller, L.M., Schuetz, P., Erni, R., Rossell, M.D., Lucas, F., Gasser, P., Holzer, L., 2013. Characterization of multi-scale microstructural features in Opalinus Clay. *Microporous and Mesoporous Materials*, 170, 83-94.
- Kelly, S., El-Sobky, H., Torres-Verdín, C., Balhoff, M.T., 2016. Assessing the utility of FIB-SEM images for shale digital rock physics. *Advances in water resources*, 95, 302-316.
- Kilmer, N.H., Morrow, N.R., Pitman, J.K., 1987. Pressure sensitivity of low permeability sandstones. *Journal of Petroleum Science and Engineering*, 1(1), 65-81.
- Klaja, J., Łykowska, G., Przelaskowska, A., 2015. Helium porosity measurements for rocks from unconventional reservoirs performed on crushed samples. *Nafta-Gaz*, 71(11), 856-863.
- Klaver, J., Desbois, G., Littke, R., Urai, J.L., 2015a. BIB-SEM characterization of pore space morphology and distribution in postmature to overmature samples from the Haynesville and Bossier Shales. *Marine and petroleum Geology*, 59, 451-466.
- Klaver, J., Desbois, G., Urai, J.L., Littke, R., 2012. BIB-SEM study of the pore space morphology in early mature Posidonia Shale from the Hils area, Germany. *International Journal of Coal Geology*, 103, 12-25.
- Klaver, J., Hemes, S., Houben, M., Desbois, G., Radi, Z., Urai, J.L., 2015b. The connectivity of pore space in mudstones: insights from high-pressure Wood's metal injection, BIB-SEM imaging, and mercury intrusion porosimetry. *Geofluids*, 15(4), 577-591.
- Klewiah, I., Berawala, D.S., Walker, H.C.A., Andersen, P.Ø., Nadeau, P.H., 2020. Review of experimental sorption studies of CO₂ and CH₄ in shales. *Journal of Natural Gas Science and Engineering*, 73, 103045.
- Klinkenberg, L.J., 1941. The permeability of porous media to liquids and gases. *Drilling and Production Practice*, 200-213.

- Krooss, B.M., Van Bergen, F., Gensterblum, Y., Siemons, N., Pagnier, H.J.M., David, P., 2002. High-pressure methane and carbon dioxide adsorption on dry and moisture-equilibrated Pennsylvanian coals. *International Journal of Coal Geology*, 51(2), 69-92.
- Kuila, U., McCarty, D.K., Derkowski, A., Fischer, T.B. and Prasad, M., 2014. Total porosity measurement in gas shales by the water immersion porosimetry (WIP) method. *Fuel*, 117, 1115-1129.
- Kundt, A. and Warburg, E., 1875. Ueber reibung und wärmeleitung verdünnter gase. *Annalen der Physik*, 232(10), 177-211.
- Kunz, O., Wagner, W., 2012. The GERG-2008 wide-range equation of state for natural gases and other mixtures: an expansion of GERG-2004. *Journal of chemical & engineering data*, 57(11), 3032-3091.
- Kwon, O., Kronenberg, A.K., Gangi, A.F. and Johnson, B., 2001. Permeability of Wilcox shale and its effective pressure law. *Journal of Geophysical Research: Solid Earth*, 106(B9), 19339-19353.
- Kwon, O., Kronenberg, A.K., Gangi, A.F., Johnson, B. and Herbert, B.E., 2004. Permeability of illite-bearing shale: 1. Anisotropy and effects of clay content and loading. *Journal of Geophysical Research: Solid Earth*, 109.
- Legland, D., Arganda-Carreras, I. and Andrey, P., 2016. MorphoLibJ: integrated library and plugins for mathematical morphology with ImageJ. *Bioinformatics*, 32(22), 3532-3534.
- Letendre, A., 2011. Permeability Changes in Lindsay Limestone Due to Isotropic Compression. Doctoral dissertation. McGill University Library.
- Letham, E.A., Bustin, R.M., 2016. Klinkenberg gas slippage measurements as a means for shale pore structure characterization. *Geofluids*, 16, 264-278.
- Li, H.H, Chen, K., Bao, S.J., Zhang, Y.L., Song, T., Wang, P., 2019. Evaluation of shale gas resources of the Sinian Doushantuo Formation in the southern Huangling anticline, western Hubei Province. *Petroleum Geology & Experiment*, 41(1), 31-37.
- Li, L., Taihigh, A., 2020. An in-depth analysis of the evolution of the policy mix for the sustainable energy transition in China from 1981 to 2020. *Applied Energy*, 263, 114611.
- Li, P., Zhang, J.C., Tang, X., Huo, Z.P., Li, Z., Luo, K.Y., Li, Z.M., 2020. Assessment of shale gas potential of the lower Permian transitional Shanxi-Taiyuan shales in the southern North China Basin. *Australian Journal of Earth Sciences*, 1-23.
- Li, S., Tang, D., Pan, Z., Xu, H., Huang, W., 2013. Characterization of the stress sensitivity of pores for different rank coals by nuclear magnetic resonance. *Fuel*, 111, 746-754.
- Li, T., Tian, H., Xiao, X., Cheng, P., Zhou, Q. and Wei, Q., 2017. Geochemical characterization and methane adsorption capacity of overmature organic-rich Lower Cambrian shales in northeast Guizhou region, southwest China. *Marine and Petroleum Geology*, 86, 858-873.
- Liang, L., Xiong, J., Liu, X., Luo, D., 2016. An investigation into the thermodynamic characteristics of methane adsorption on different clay minerals. *Journal of Natural Gas Science and Engineering*, 33, 1046-1055.
- Lippitt, L., 1959. Statistical analysis of regional facies change in Ordovician Cobourg limestone in northwestern New York and southern Ontario. *AAPG Bulletin*, 43(4), 807-815.
- Littke, R., Klusmann, U., Krooss, B., Leythaeuser, D., 1991. Quantification of loss of calcite, pyrite, and organic matter due to weathering of Toarcian black shales and effects on kerogen and bitumen characteristics. *Geochimica et Cosmochimica Acta*, 55(11), 3369-3378.
- Littke, R., Urai, J.L., Uffmann, A.K., Risvanis, F., 2012. Reflectance of dispersed vitrinite in Palaeozoic rocks with and without cleavage: Implications for burial and thermal history modeling in the Devonian of Rursee area, northern Rhenish Massif, Germany. *International Journal of Coal Geology*, 89, 41-50.

- Liu, J., Spiers, C.J., Peach, C.J., Vidal-Gilbert, S., 2016. Effect of lithostatic stress on methane sorption by coal: Theory vs. experiment and implications for predicting in-situ coalbed methane content. *International Journal of Coal Geology*, 167, 48-64.
- Loubergé, H., Villeneuve, S., Chesney, M., 2002. Long-term risk management of nuclear waste: a real options approach. *Journal of Economic Dynamics and Control*, 27, 157-180.
- Loucks, R.G., Reed, R.M., Ruppel, S.C. and Hammes, U., 2012. Spectrum of pore types and networks in mudrocks and a descriptive classification for matrix-related mudrock pores. *AAPG bulletin*, 96(6), 1071-1098.
- Loucks, R.G., Reed, R.M., Ruppel, S.C., Jarvie, D.M., 2009. Morphology, genesis, and distribution of nanometer-scale pores in siliceous mudstones of the Mississippian Barnett Shale. *Journal of sedimentary research*, 79(12), 848-861.
- Lu, X.C., Li, F.C., Watson, A.T., 1995. Adsorption measurements in Devonian shales. *Fuel*, 74(4), 599-603.
- Mahanta, B., Tripathy, A., Vishal, V., Singh, T.N., Ranjith, P.G., 2017. Effects of strain rate on fracture toughness and energy release rate of gas shales. *Engineering geology*, 218, 39-49.
- Mählmann, R.F., Frey, M., 2012. Standardisation, calibration and correlation of the Kübler-index and the vitrinite/bituminite reflectance: an inter-laboratory and field related study. *Swiss Journal of Geosciences*, 105(2), 153-170.
- Maliva, R.G., Knoll, A.H., Siever, R., 1989. Secular change in chert distribution: a reflection of evolving biological participation in the silica cycle. *Palaios*, 519-532.
- Masschaele, B., Cnudde, V., Dierick, M., Jacobs, P., Van Hoorebeke, L., Vlassenbroeck, J., 2007. UGCT: New x-ray radiography and tomography facility. *Nuclear Instruments and Methods in Physics Research Section A* 580, 266-269.
- McDowell, S.D., Elders, W.A., 1980. Authigenic layer silicate minerals in borehole Elmore 1, Salton Sea geothermal field, California, USA. *Contributions to mineralogy and petrology*, 74(3), 293-310.
- McKernan, R.E., Rutter, E.H., Mecklenburgh, J., Taylor, K.G., Covey-Crump, S.J., 2014. Influence of effective pressure on mudstone matrix permeability: implications for shale gas production. In *SPE/EAGE European Unconventional Resources Conference and Exhibition*. Society of Petroleum Engineers.
- McKinley, I., 1992. The management of long lived nuclear waste. *Energy Policy*, 20(7), 1992, 683-692.
- Merkel, A., Fink, R., Littke, R., 2015a. The role of pre-adsorbed water on methane sorption capacity of Bossier and Haynesville shales. *International Journal of Coal Geology*, 147, 1-8.
- Merkel, A., Fink, R., Littke, R., 2016. High pressure methane sorption characteristics of lacustrine shales from the Midland Valley Basin, Scotland. *Fuel*, 182, 361-372.
- Merkel, A., Gensterblum, Y., Krooss, B.M., Amann, A., 2015b. Competitive sorption of CH₄, CO₂ and H₂O on natural coals of different rank. *International Journal of Coal Geology*, 150, 181-192.
- Mikutta, R., Kleber, M., Kaiser, K., Jahn, R., 2005. Organic matter removal from soils using hydrogen peroxide, sodium hypochlorite, and disodium peroxodisulfate. *Soil science society of America journal*, 69(1), 120-135.
- Milliken, K.L., Rudnicki, M., Awwiller, D.N., Zhang, T., 2013. Organic matter-hosted pore system, Marcellus formation (Devonian), Pennsylvania. *AAPG bulletin*, 97(2), 177-200.
- Morrow, C.A., Shi, L., Byerlee, J.D., 1984. Permeability of fault gouge under confining pressure and shear stress. *J Geophys Res*, 89, 3193-3200.

- Mostaghimi, P., Blunt, M.J., Bijeljic, B., 2013. Computations of absolute permeability on micro-CT images. *Mathematical Geosciences*, 45(1), 103-125.
- Nasserri, M.H.B., Goodfellow, S.D., Wanne, T., Young, R.P., 2013. Thermo-hydro-mechanical properties of Cobourg limestone. *International Journal of Rock Mechanics and Mining Sciences*, 61, 212-222.
- NBS, 2019. China Energy Consumption Yearbook (2009-2018). National Bureau of Statistics of China.
- Nguyen, T.S., Li, Z., Su, G., Nasserri, M.H.B., Young, R.P., 2018. Hydro-mechanical behavior of an argillaceous limestone considered as a potential host formation for radioactive waste disposal. *Journal of Rock Mechanics and Geotechnical Engineering*, 10(6), 1063-1081.
- Nie, H.K., Tang, X., Bian, R., 2009. Controlling factors for shale gas accumulation and prediction of potential development area in shale gas reservoir of South China. *Acta Petrolei Sinica*, 30(4), 484-491.
- Nolte, S., Geel, C., Amann-Hildenbrand, A., Krooss, B.M., Littke, R., 2019. Petrophysical and geochemical characterization of potential unconventional gas shale reservoirs in the southern Karoo Basin, South Africa. *International Journal of Coal Geology*, 212, 103249.
- Nuttal, B.C., Eble, C., Bustin, R.M., Drahovzal, J.A., 2005. Analysis of Devonian black shales in Kentucky for potential carbon dioxide sequestration and enhanced natural gas production. *Greenhouse Gas Control Technologies*, 7, 2225-2228.
- NWMO, 2011. Geosynthesis. Nuclear Waste Management Organization Report (NWMO).TR-2011-11 R000. Toronto, Canada.
- Ojovan, M.I., Lee, W.E., 2014. *An Introduction to Nuclear Waste Immobilisation (Second Edition)*. Oxford, 321-335.
- Ollion, J., Cochenec, J., Loll, F., Escudé, C., Boudier, T., 2013. TANGO: a generic tool for high-throughput 3D image analysis for studying nuclear organization. *Bioinformatics*, 29(14), 1840-1841.
- Peters, E.J., 2005. *Petrophysics*. Department of Petroleum and Geosystems Engineering, University of Texas at Austin.
- Petts, D.C., Saso, J.K., Diamond, L.W., Aschwanden, L., Al, T.A., Jensen, M., 2017. The source and evolution of paleofluids responsible for secondary minerals in low-permeability Ordovician limestones of the Michigan Basin. *Applied Geochemistry*, 86, 121-137.
- Philipp, T., Amann-Hildenbrand, A., Laurich, B., Desbois, G., Littke, R., Urai, J.L., 2017. The effect of microstructural heterogeneity on pore size distribution and permeability in Opalinus Clay (Mont Terri, Switzerland): insights from an integrated study of laboratory fluid flow and pore morphology from BIB-SEM images. *Geological Society, London, Special Publications*, 454(1), 85-106.
- Pone, J.D.N., Halleck, P.M., Mathews, J.P., 2009. Sorption capacity and sorption kinetic measurements of CO₂ and CH₄ in confined and unconfined bituminous coal. *Energy & Fuels*, 23(9), 4688-4695.
- Randolph, P.L., Soeder, D.J., Chowdiah, P., 1984. Porosity and permeability of tight sands. SPE Paper 12836 Presented at the SPE Unconventional Gas Recovery Symposium, 13–15 May, Pittsburgh, Pennsylvania, USA.
- Raven, K.G., Gale, J.E., 1985. Water flow in a natural rock fracture as a function of stress and sample size. *International Journal of Rock Mechanics and Mining Sciences & Geomechanics*, 22(4), 251-261.
- Ren, J., Niu, B., Wang, J., Jin, X., Zhao, L., Liu, R., 2013. Advances in research of Asian geology—A summary of 1: 5M International Geological Map of Asia project. *Journal of Asian Earth Sciences*, 72, 3-11.
- Rexer, T.F., Benham, M.J., Aplin, A.C., Thomas, K.M., 2013. Methane adsorption on shale under simulated geological temperature and pressure conditions. *Energy & Fuels*, 27(6), 3099-3109.

- Rexer, T.F., Mathia, E.J., Aplin, A.C., Thomas, K.M., 2014. High-pressure methane adsorption and characterization of pores in Posidonia shales and isolated kerogens. *Energy & Fuels*, 28(5), 2886-2901.
- Ross, D.J. and Bustin, R.M., 2009. The importance of shale composition and pore structure upon gas storage potential of shale gas reservoirs. *Marine and petroleum Geology*, 26(6), 916-927.
- Rouquerol, J., Rouquerol, F., Llewellyn, P., Maurin, G., Sing, K.S., 2013. Adsorption by powders and porous solids: principles, methodology and applications. Academic press.
- Rutter, E., Mecklenburgh, J., Taylor, K., 2017. Geomechanical and petrophysical properties of mudrocks: introduction. Geological Society, London, Special Publications, 454 (1), 1-13.
- Sandalow, D., Wu, J., Yang, Q., Hove, A., Lin, J., 2014. Meeting China's Shale Gas Goals. Center on global energy policy, Columbia.
- Sander, R., Pan, Z., Connell, L.D., 2017. Laboratory measurement of low permeability unconventional gas reservoir rocks: A review of experimental methods. *Journal of Natural Gas Science and Engineering*, 37, 248-279.
- Saxena, N., Hofmann, R., Alpak, F.O., Berg, S., Dietderich, J., Agarwal, U., Tandon, K., Hunter, S., Freeman, J., Wilson, O.B., 2017. References and benchmarks for pore-scale flow simulated using micro-CT images of porous media and digital rocks. *Advances in Water Resources*, 109, 211-235.
- Seemann, T., Bertier, P., Krooss, B.M., Stanjek, H., 2017. Water vapour sorption on mudrocks. Geological Society, London, Special Publications, 454(1), 201-233.
- Selvadurai, A. P. S., Głowacki, A., 2016. Stress-Induced Permeability Alterations in an Argillaceous Limestone. *Rock Mechanics and Rock Engineering*, 50(5), 1079–1096.
- Selvadurai, A.P.S., 2017. Geomechanical characterization of the Cobourg Limestone. Nuclear Waste Management Organization Technical Report TR-2017.
- Selvadurai, A.P.S., 2019. A Multi-phasic perspective of the intact permeability of the Heterogeneous Argillaceous cobourg Limestone. *Scientific reports*, 9(1), 1-14.
- Selvadurai, A.P.S., Głowacki, A., 2018. Estimates for the local permeability of the Cobourg limestone. *Journal of Rock Mechanics and Geotechnical Engineering*, 10(6), 1009-1019.
- Shi, Y., Wang, C.Y., 1986. Pore pressure generation in sedimentary basins: overloading versus aquathermal. *Journal of Geophysical Research: Solid Earth*, 91(B2), 2153-2162.
- Sing, K.S., 1991. Characterization of porous solids: An introductory survey. In *Studies in Surface Science and Catalysis*, 62, 1-9.
- Slatt, R.M., O'Brien, N.R., 2011. Pore types in the Barnett and Woodford gas shales: Contribution to understanding gas storage and migration pathways in fine-grained rocks. *AAPG bulletin*, 95(12), 2017-2030.
- Snow, D.T., 1965. A parallel plate model of fractured permeable media. Ph. D. Thesis, Univ. of California.
- Soeder, D.J., 1988. Porosity and permeability of eastern Devonian gas shale. *SPE Formation Evaluation*, 3(01), 116-124.
- Soldal, M., Wilkinson, H.D., Viken, I., Sauvin, G., 2017. Rock visualization using micro-CT scanner and X-ray transparent triaxial apparatus. In *International Symposium of the Society of Core Analysts* (p. 9).
- Sondergeld, C.H., Newsham, K.E., Comisky, J.T., Rice, M.C., Rai, C.S., 2010. Petrophysical considerations in evaluating and producing shale gas resources. In *SPE unconventional gas conference*. Society of Petroleum Engineers.

- Tan, J., Horsfield, B., Mahlstedt, N., Zhang, J., di Primio, R., Vu, T.A.T., Boreham, C.J., van Graas, G., Tocher, B.A., 2013. Physical properties of petroleum formed during maturation of Lower Cambrian shale in the upper Yangtze Platform, South China, as inferred from PhaseKinetics modelling. *Marine and Petroleum Geology*, 48, 47-56.
- Tarhan, L.G., Hood, A.V., Droser, M.L., Gehling, J.G., Briggs, D.E., 2016. Exceptional preservation of soft-bodied Ediacara Biota promoted by silica-rich oceans. *Geology*, 44(11), 951-954.
- Taylor, G.H., Teichmüller, M., Davis, A.C.F.K., Diessel, C.F.K., Littke, R. and Robert, P., 1998. *Organic petrology*.
- Teklu, T.W., Zhou, Z., Li, X., Abass, H., 2016. Experimental investigation on permeability and porosity hysteresis in low-permeability formations. In *SPE Low Perm Symposium*. Society of Petroleum Engineers.
- Terzaghi, K., 1936. The shearing resistance of saturated soils and the angle between the planes of shear. In *First international conference on soil Mechanics*, 1936, 54-59.
- Thommes, M., Kaneko, K., Neimark, A.V., Olivier, J.P., Rodriguez-Reinoso, F., Rouquerol, J. and Sing, K.S., 2015. Physisorption of gases, with special reference to the evaluation of surface area and pore size distribution (IUPAC Technical Report). *Pure and applied chemistry*, 87(9-10), 1051-1069.
- Tiab, D., Donaldson, E.C., 2015. *Petrophysics: theory and practice of measuring reservoir rock and fluid transport properties*. Gulf professional publishing.
- Tinni, A., Fathi, E., Agarwal, R., Sondergeld, C.H., Akkutlu, I.Y., Rai, C.S., 2012. Shale permeability measurements on plugs and crushed samples. In *SPE Canadian Unconventional Resources Conference*. Society of Petroleum Engineers.
- Tissot, B.P., Welte, D.H., 2013. *Petroleum formation and occurrence*. Springer Science & Business Media.
- Ufer, K., Kleeberg, R., 2015. Parametric Rietveld refinement of coexisting disordered clay minerals. *Clay Minerals*, 50(3), 287-296.
- Ufer, K., Stanjek, H., Roth, G., Dohrmann, R., Kleeberg, R., Kaufhold, S., 2008. Quantitative phase analysis of bentonites by the Rietveld method. *Clays and Clay Minerals*, 56(2), 272-282.
- Uffmann, A.K., Littke, R., Rippen, D., 2012. Mineralogy and geochemistry of Mississippian and Lower Pennsylvanian black shales at the northern margin of the Variscan Mountain Belt (Germany and Belgium). *International Journal of Coal Geology*, 103, 92-108.
- Vandenbroucke, M., Largeau, C., 2007. Kerogen origin, evolution and structure. *Organic Geochemistry*, 38(5), 719-833.
- Vanorio, T., Prasad, M., Nur, A., 2003. Elastic properties of dry clay mineral aggregates, suspensions and sandstones. *Geophysical Journal International*, 155(1), 319-326.
- Vilks, P., Miller, N.H., 2007. Evaluation of experimental protocols for characterizing diffusion in sedimentary rocks (NWMO). TR-2007-11. Toronto, Canada.
- Vogler, D., Walsh, S.D., Bayer, P., Amann, F., 2017. Comparison of surface properties in natural and artificially generated fractures in a crystalline rock. *Rock Mechanics and Rock Engineering*, 50(11), 2891-2909.
- Waliczek, M., Machowski, G., Poprawa, P., Świerczewska, A. and Więclaw, D., 2021. A novel VRo, Tmax, and S indices conversion formulae on data from the fold-and-thrust belt of the Western Outer Carpathians (Poland). *International Journal of Coal Geology*, 234, 103672.

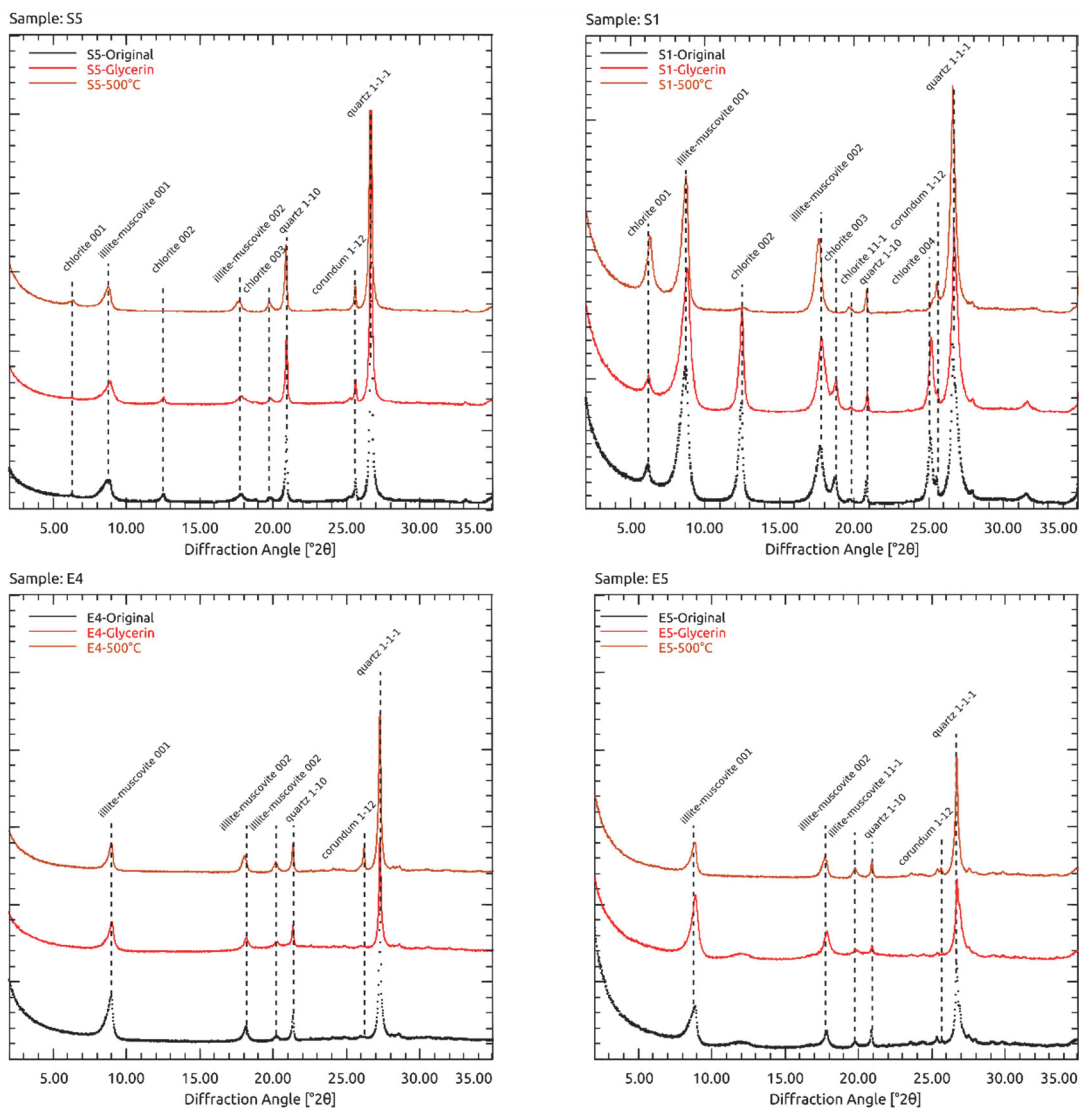
- Walsh, J.B., 1981. Effect of pore pressure and confining pressure on fracture permeability. In *International Journal of Rock Mechanics and Mining Sciences & Geomechanics Abstracts*, 18(5), 429-435.
- Wang, P., Jiang, Z., Chen, L., Yin, L., Li, Z., Zhang, C., Tang, X., Wang, G., 2016. Pore structure characterization for the Longmaxi and Niutitang shales in the Upper Yangtze Platform, South China: Evidence from focused ion beam–He ion microscopy, nano-computerized tomography and gas adsorption analysis. *Marine and Petroleum Geology*, 77, 1323-1337.
- Wang, Y., Meng, F., Wang, X., Baud, P., Wong, T.F., 2018. Effective stress law for the permeability and deformation of four porous limestones. *Journal of Geophysical Research: Solid Earth*, 123(6), 4707-4729.
- Wang, Y.F., Zhai, G.Y., Lu, Y.C., Ma, Y.Q., Li, J., Liu, G.H., Zhang, Y.X., 2019. Sedimentary lithofacies characteristics and sweet-spot interval characterization of the Sinian Doushantuo Formation in Upper Yangtze Platform, South China. *China Geology*, 2(3), 261-275.
- Wang, Z.G., Tan, X.C., 1994. Palaeozoic structural evolution of Yunnan. *Journal of Southeast Asian Earth Sciences*, 9(4), 345-348.
- Weaver, C.E., 1967. Potassium, illite and the ocean. *Geochimica et cosmochimica acta*, 31(11), 2181-2196.
- Weaver, C.E., 1989. *Clays, muds, and shales*. Elsevier, New York.
- Witherspoon, P.A., Bodvarsson, G.S., 2006. Geological challenges in radioactive waste isolation: fourth worldwide review.
- WNA, 2020. *Nuclear Power in China*. World Nuclear Association.
- Wu, S.J., Wei, G.Q., Yang, W., Xie, W.R., Zeng, F.Y., 2016. Tongwan Movement and its geologic significances in Sichuan Basin. *Natural Gas Geoscience*, 27(1), 60-70.
- Xiang, Y., Al, T., Scott, L., Loomer, D., 2013. Diffusive anisotropy in low-permeability Ordovician sedimentary rocks from the Michigan Basin in southwest Ontario. *Journal of Contaminant Hydrology*, 155, 31-45.
- Xu, C., Lin, C., Kang, Y., You, L., 2018a. An experimental study on porosity and permeability stress-sensitive behavior of sandstone under hydrostatic compression: characteristics, mechanisms and controlling factors. *Rock Mechanics and Rock Engineering*, 51(8), 2321-2338.
- Xu, H., Zhou, W., Cao, Q., Xiao, C., Zhou, Q., Zhang, H., Zhang, Y., 2018b. Differential fluid migration behaviour and tectonic movement in Lower Silurian and Lower Cambrian shale gas systems in China using isotope geochemistry. *Marine and Petroleum Geology*, 89, 47-57.
- Yang, B., Xue, L., Duan, Y. and Wang, M., 2021. Correlation study between fracability and brittleness of shale-gas reservoir. *Geomechanics and Geophysics for Geo-Energy and Geo-Resources*, 7(2), 1-13.
- Yang, F., Hu, B., Xu, S., Meng, Q., Krooss, B.M., 2018. Thermodynamic characteristic of methane sorption on shales from oil, gas, and condensate windows. *Energy & Fuels*, 32(10), 10443-10456.
- Yang, F., Ning, Z., Zhang, R., Zhao, H., Krooss, B.M., 2015. Investigations on the methane sorption capacity of marine shales from Sichuan Basin, China. *International Journal of Coal Geology*, 146, 104-117.
- Yang, F., Xie, C., Ning, Z., Krooss, B.M., 2017. High-pressure methane sorption on dry and moisture-equilibrated shales. *Energy & Fuels*, 31(1), 482-492.
- Yang, R., He, S., Hu, Q., Hu, D., Zhang, S., Yi, J., 2016. Pore characterization and methane sorption capacity of over-mature organic-rich Wufeng and Longmaxi shales in the southeast Sichuan Basin, China. *Marine and Petroleum Geology*, 77, 247-261.

- Yang, W., He, S., Zhai, G., Tao, Z., Dong, T., Han, Y., Chen, K., Wei, S., 2020. Pore characteristics of the lower Sinian Doushantuo Shale in the Mid-Yangtze Yichang area of China: Insights into a distinct shale gas reservoir in the Neoproterozoic formation. *Journal of Natural Gas Science and Engineering*, 73, 103085.
- Yang, Y., Aplin, A.C., 2007. Permeability and petrophysical properties of 30 natural mudstones. *Journal of Geophysical Research: Solid Earth*, 112 (B3).
- Yang, Y., Aplin, A.C., 2010. A permeability–porosity relationship for mudstones. *Marine and Petroleum Geology*, 27(8), 1692-1697.
- Yasin, Q., Du, Q., Sohail, G.M. and Ismail, A., 2018. Fracturing index-based brittleness prediction from geophysical logging data: application to Longmaxi shale. *Geomechanics and Geophysics for Geo-Energy and Geo-Resources*, 4(4), 301-325.
- Yuan, Y.S., Sun, D.S., Li, S.J., Lin, J.H., 2013. Caledonian erosion thickness reconstruction in the Sichuan Basin. *Chinese Journal of Geology*, 48(3), 581-591.
- Zhai, G.M., 1987. *Petroleum geology of China*. Petroleum Industry Press, 10, 30-33.
- Zhai, G.Y., Wang, Y.F., Zhou, Z., Liu, G.H., Yang, Y.R., Li, J., 2018. “Source-Diagenesis-Accumulation” enrichment and accumulation regularity of marine shale gas in southern China. *China Geology*, 1(3), 319-330.
- Zhang, C.L., 2015. Investigation of gas migration in damaged and resealed claystone. *Geological Society, London, Special Publications*, 415(1), 75-93.
- Zhang, Q., Littke, R., Zieger, L., Shabani, M., Tang, X. and Zhang, J., 2019. Ediacaran, Cambrian, Ordovician, Silurian and Permian shales of the Upper Yangtze Platform, South China: Deposition, thermal maturity and shale gas potential. *International Journal of Coal Geology*, 216, 1-20.
- Zhang, R., Ning, Z., Yang, F., Zhao, H., Wang, Q., 2016. A laboratory study of the porosity-permeability relationships of shale and sandstone under effective stress. *International Journal of Rock Mechanics and Mining Sciences*, (81), 19-27.
- Zhang, T., Ellis, G.S., Ruppel, S.C., Milliken, K., Yang, R., 2012. Effect of organic-matter type and thermal maturity on methane adsorption in shale-gas systems. *Organic geochemistry*, 47, 120-131.
- Zhao, J., Jin, Z., Jin, Z., Wen, X., Geng, Y., 2017. Origin of authigenic quartz in organic-rich shales of the Wufeng and Longmaxi Formations in the Sichuan Basin, South China: Implications for pore evolution. *Journal of Natural Gas Science and Engineering*, 38, 21-38.
- Zheng, J., Zheng, L., Liu, H.H., Ju, Y., 2015. Relationships between permeability, porosity and effective stress for low-permeability sedimentary rock. *International Journal of Rock Mechanics and Mining Sciences*, 78, 304-318.
- Zhou, Y., 2010. Why is China going nuclear?. *Energy Policy*, 38(7), 3755-3762.
- Zhu, C., Hu, S., Qiu, N., Rao, S., Yuan, Y., 2016. The thermal history of the Sichuan Basin, SW China: Evidence from the deep boreholes. *Science China Earth Sciences*, 59(1), 70-82.
- Ziemiański, P.P., Derkowski, A., Szczurowski, J. and Kozieł, M., 2020. The structural versus textural control on the methane sorption capacity of clay minerals. *International Journal of Coal Geology*, 103483.
- Zimmermann, G., Burkhardt, H., Engelhard, L., 2005. Scale dependence of hydraulic and structural parameters in fractured rock, from borehole data (KTB and HSDP). *Geological Society, London, Special Publications*, 240(1), 37-45.
- Zou, C., 2017. *Unconventional petroleum geology*. Elsevier.

Zou, C.N., Dong, D.Z., Wang, Y.M., Li, X.J., Huang, J.L., Wang, S.F., Guan, Q.Z., Zhang, C.C., Wang, H.Y., Liu, H.L., Bai, W.H., Liang, F., Lin, W., Zhao, Q., Liu, D.X., Yang, Z., Liang, P.P., Sun, S.S., Qiu, Z., 2016. Shale gas in China: Characteristics, challenges and prospects (II). *Pet. Explor. Dev.* 43 (2), 1–13.

Zou, C.N., Du, J.H., Xu, C.C., Wang, Z.C., Zhang, B.M., Wei, G.Q., Wang, T.S., Yao, G.S., Deng, S.H., Liu, J.J., Zhou, H., Xu, A.N., Yang, Z., Jiang, H., Gu, Z.D., 2014. Formation, distribution, resource potential, and discovery of Sinian–Cambrian giant gas field, Sichuan Basin, SW China. *Pet. Explor. Dev.* 41 (3), 306–325.

7. Appendix



Appendix 1 X-ray diffraction pattern of separated clay fraction measured as texture preparations of four representative shale samples (S5, S1, E4, E5); representing the untreated, original sample (black), the glycerin treated sample (red) and heated sample (orange). Reflections are labeled according to the individual mineral and its corresponding hkl's.

Curriculum vitae

Personal Information

Name: Zhazha Hu

Gender: Male

Tel: +49 241 80 95755

Email: zhazha.hu@emr.rwth-aachen.de

Address: RWTH Aachen University, Lochnerstr. 4-20, 52056 Aachen, Germany

Research Interests

Fluid flow in low-permeable rocks, high-pressure gas sorption, permeability simulation, mineralogy.

Education

- Since 2016: Applied Geosciences (Ph.D. student), RWTH Aachen University
- 2013-2016: Engineering Geology (M.Sc.), China University of Geosciences (Beijing)
- 2009-2013: Resources Exploration Engineering (B.Sc.), Yangtze University.

Publications

- [Hu, Z.](#), Klaver, J., Schmatz, J., Dewanckele, J., Littke, R., Krooss, B.M., Amann-Hildenbrand, A., 2020. Stress sensitivity of porosity and permeability of Cobourg Limestone. *Engineering Geology*, 105632.
- [Hu, Z.](#), Gaus, G., Seemann, T., Zhang, Q., Littke, R., Reinhard, F., 2021. Pore structure and sorption capacity investigations of Ediacaran and Lower Silurian gas shales from the Upper Yangtze platform, China. *Geomechanics and Geophysics for Geo-Energy and Geo-Resources*, 7(3), 1-26.
- Davy, C. A., [Hu, Z.](#), Selvadurai, A.P.S., Klaver, J., Willemetz, M.C., Agostini, F., Skoczylas, F., Dewanckele, J., Amann-Hildenbrand, A., Lenormand, R., 2019. Transport properties of the Cobourg Limestone: A benchmark investigation. *The 2019 International Symposium of the Society of Core Analysts*, SCA2019-037.
- Zhang, Q., Huang, W., [Hu, Z.](#), Zhou, H., Lu, X., Lin, K. and Xia, X., 2017. Study of the effects of hydraulic fracturing at different dip angles for the development of coalbed methane: a case study in the southeast part of Qinshui Basin, China. *International Journal of Oil, Gas and Coal Technology*, 14(1-2), 186-200.